Nature Inspired Surface/Interface Engineering Towards Advanced Device Applications

SREEPATHY SRIDHAR

PhD

2020

Nature Inspired Surface/Interface Engineering Towards Advanced Device Applications

SREEPATHY SRIDHAR

A thesis submitted in partial fulfilment of the requirements of the University of Northumbria at Newcastle for the degree of Doctor of Philosophy

Department of Mechanical and Construction Engineering

December 2020

Abstract

Nature inspired surface/interface with multi-faceted functions possess promises in the frontier engineering applications in flexible electronics, energy harvesting, autonomous systems, bio-mimicking tissues, micro-fluidics, etc. Understanding the relationship between nature's architecture and underlying science could bring enabling solutions to overcome the engineering challenges. A nature inspired surface with smart resilient features provides intrinsic complexity and their multiplicity under different stimuli, i.e. chemical, physical, electronic, mechanical and (in some cases) biological properties. By mimicking/harvesting a variety of surface and interfacial features from nature, the final composition will display an integrative design to provide further explorations in deciphering the hidden physics towards advanced device applications in real world.

Specifically, we bring a few engineering examples with chemical/physical approaches to construct artificial nano/micro-structured surface, yield various functional surface for different application scenarios.

- A porous layer has been realised to provide controllable generation of microarchitecture to exhibit an anti-corrosion behaviour under UV exposure with multifaceted characteristics such as profound solar absorptivity, thermal emissivity. By further treating the surface with silane, a hybrid layer has been established with superhydrophobic and anti-icing features which shares innate interests in thermal transport/aero-space engineering.

- The structural conformation/ elastic instabilities of the surface are exploited to devise an extreme switchable configuration to develop a morphing strategy

for switchable lipophilic/oleophobic properties. The geometrical shift of soft structure is instructed to create a steady transition of surface topology rendering a unique switchable transition that are widely inspired in sub-sea/offshore engineering for oil and water separation.

- We also develop a highly-replenishable thermal energy harvesting technology via a dynamical elasto-bouncing process of polymeric hydrogel to translate the thermal energy into useful elasto-kinetic energy, then further converted into electrical energy via a simple piezo-material based system, which paves way for a future portable and conformable energy harvesting tool in the regions of extreme geo-thermal residencies and industries.

- Using a one drop filling technique along with interfacial pinning points between hydrophilic and hydrophobic, a unique microfluidic approach is presented to create heterogenous structures. By exploiting the communication between swelling mismatch of different functional groups, driven via in-plane and through thickness heterogeity, a highly complex 3D soft reconfiguration is achieved which is activated by stimulation inputs.

- The theoretical understandings are exploited in the above applied engineering scenarios, such as elastic mechanics, morphing structure, surface/interface interactions and kinetics of of the polymer systems experienced on a hot surface, which offers further insights into the elastic recoiling evolution and tunability of the system for effective energy translation efficiency.

We hope above approaches shed more lights on the nature inspired structure in device engineering, thus, advance the knowledge in the frontier science.

Acknowledgement

I would like to thank my PhD advisors, Professor Ben Bin Xu and Dr. Yifan Li, who has been profoundly supportive in my researches. I will forever be thankful to my external supervisor and friend Dr. Steven Wang from City University of Hong Kong. I still think fondly of him, considering me as his own PhD student and assisting me to complete my thesis.

I also thank the formal members of my research group Dr. Cong Wang (Now a PDRA in Kings College London) and Dr. Ding Wang (Now a PDRA in University of Southampton) for their helpful and knowledgeable guidance upon my arrival to the group. I would like to express my thanks to the technical staffs, Gavin Warburton, Simon Nivelle, Paul Curran for their valuable advice and experience and making my research life more enthusiastic and homely. I thank all the members of staff and academics who I have worked with in Northumbria University. I appreciate to Northumbria University for providing me the RDF PhD studentship and the access to research facilities.

I would also like to thank everyone who has been working in the same lab and office with me, for their valuable advices and discussions on my research and study. Furthermore, I would like to express my thanks to the staffs in the lab, workshop for their help. I appreciate the lab facilities and computing resources that are provided by Northumbria University.

I appreciate the contributions from the collaborated institutes and project partners, which are:

Most important, I would like to express my deepest gratitude to my family for their endless dedication throughout my existing time on earth. I wouldn't have achieved anything without their love and care.

Dedication

This thesis is dedicated to my father the late Sridhar Subramanian and my mother Bhuvaneswari Sridhar for their strenuous encouragement to motivate me to pursue my dreams and supporting a long way to achieve them one by one.

Declaration

I declare that the work contained in this thesis has not been submitted for any other award and that it is all my own work. I also confirm that this work fully acknowledges opinions, ideas and contributions from the work of others.

Any ethical clearance for the research presented in this thesis has been approved.

I declare that the word count of this thesis is currently 38303 words

Name: Sreepathy Sridhar

Signature:

Date: 17/12/2020

Contents

List of Figures

List of Tables

Achievements

Journal paper:

1. **S. Sridhar***, C. Wang*, J. G. Terry, X. Chen, A. Sun, Z. Li, H. Lv, B. B. Xu, Y. Li, Controlled Co-operative Wetting Enabled Heterogeneous Structured 3D Morphing Transducers, Adv. Mater. Interfaces 2020, 2001211. (**Q1**)

2. D. Wang*, Y. Liu*, **S. Sridhar***, Y. Li, G. McHale, H. Lv, Z. Yu, S. Wang, B. B. Xu, Bi-axially Morphing Droplet Shape by an Active Surface, Adv. Mater. Interfaces 2020, 2001199. (**Q1,** Wiley Hot Topics paper in Surfaces and Interfaces)

3. Z. Zhao, C. Ling, D. Wang, J.-X. Wang, J. Saczek, S. Pramana, **S. Sridhar**, J. Shang, B. B. Xu, D. C.W. Tsang, J.-F. Chen, S. Wang, Liquid Marbles in Liquid, Small 2020, 16, 2002802. (IF=11.459, 23rd of 314 in MATERIALS SCIENCE, **Top 10%,** press in MaterialsViewsChina)

4. Y. Jiao, C. Ling, J.-X. Wang, H. Amanico, J. Saczek, H. Wang, **S. Sridhar**, B. B. Xu, S. Wang, D. Wan, Controllable Synthesis of Up-conversion Nanophosphors towards Scale-up Productions, Part. Part. Syst. Charact. 2020, 37, 2000129.

5. Z. Li, Y. Liu, M. Lei, A. Sun, **S. Sridhar**, Y. Li, X. Liu, H. Lu, Y. Q. Fu, B. B. Xu, Stimuli-responsive gel impregnated surface with switchable lipophilic/oleophobic properties, Soft Matter 2020, 16, 1636. (**Q1**)

6. Z. Zhang*, **S. Sridhar***, G. Weib, Y. Yub, Z. Zhangb, L. Jiang, Y. Yang, M. W. Shahzad, X. Chen, B. B. Xu, A highly controlled fabrication of porous anodic aluminium oxide surface with versatile features by spatial thermo-anodization, Surf. Coat. Technol. 2020, 126809. **(Q1)**

7. Y. Liu, A. Sun, **S. Sridhar**, Z. Li, Z. Qi, J. Liu, X. Chen, H. Lv, B.Z. Tang, B. B. Xu, An Autonomous Soft Gripper enabled by Harnessing Multimode Elastic Instabilities, **under review.**

8. **S. Sridhar**, A.Sun, T. Wang, Y. Li, Z. Wang, S. Wang, B. B. Xu, Guided Soft Thermo-Electric Harvester Fuelled by Elastic Leidenfrost, **to be submitted.**

9. A. Sun, **S. Sridhar**, Y. Li, B. B. Xu, Highly tunable 3D printed smart gel based intraocular lens with increased refractive index and biocompatibility, **to be submitted.**

Award & Exchange Experiences:

1. Visiting Research Student in Department of Chemical Engineering, SEP 2018 – MAR 2019, Newcastle University
2. *Fourth Meeting: On-site Industry Away Day at Merck*, 11 DEC 2018, Merck, Southampton

Certified Workshops & Conference:

1. *CSCST SCI Annual Conference: Sustainable Energy and Manufacturing the Future,* 11 – 12 SEP 2020 (**Poster Presentation**)
2. *CSCST SCI Annual Conference: Sustainable Energy and Manufacturing the Future,* 11 – 12 SEP 2020 (**Oral Presentation**)
3. *Reforming Multi-disciplinary Engineering Innovation for the New Normal Symposium*, 28 AUG 2020, Northumbria University, UK (**Flash Talk)**
4. *Droplets 2019*, 16 – 18 SEP 2019, Durham University, UK (**Poster Presentation**)
5. *IEEE Transducers* 2019, 23 -27 JUN 2019, Berlim, Germany (**Poster Presentation**)
6. *Invited talk: Process Intensification Group,* 17th May 2019, Newcastle University, UK (**Invited Talk**)

7. *HYMA 2019: 6th International Conference on Multifunctional, Hybrid, and Nanomaterials*, 11 – 15 MAR 2019, Sitges, Spain (**Poster Presentation**)

8. *UK Fluid Networks (UKFN) – Multiscale Modelling of Wetting Phenomena*, 12 -13 SEP 2018, Durham, UK (**Workshop**)

9. *The 25th Joint Annual Conference of CSCST-SCI*, 6 - 7 SEP 2018, University of Manchester, UK (**Oral Presentation**)

10. **Third Prize** in Oral Presentation, The 25th Joint Annual Conference of CSCST-SCI, 6-7 SEP 2018, University of Manchester

11. *UK Fluids Conference 2018*, 4 – 6 SEP 2018, University of Manchester, UK (**Poster Presentation**)

12. *UKFN SIG mini-symposium: Structural surfaces and liquid/surface interactions*, 20 April 2018, Heriot-Watt University, Edinburgh (**Video Presentation)**

13. UKFN – *Smart materials and surfaces powered future engineering solutions*, 29th Nov 2017, Nottingham Trent University(**Workshop**)

Chapter 1

Introduction

Fascinating phenomenon in nature, such as the water-repellent microarchitectures of lotus leaves[1], reduced drag force in shark skin[2], anti-icing and oil repellent structures in filefish[3, 4], invisible gas vapor present on heated systems[5] have inspired researchers to reveal the underlying science and utilise them to enable novel technologies. Such attempts are of cardinal consequential due to its potential elucidation towards commitments for a variety of real-world challenges. Despite decades of immense research and development in exploiting complex surface and interfacial systems with focuses on superwettability, surface energy harvesting and conversion, gas/droplet transportation, etc, the mission of exploring cheaper and smarter systems with desired performance is still ongoing. This thesis will address this deficiency by offering some perspective approaches on understanding the currently available wilderness inspired systems and concepts devised from the above physics. It will also be discussed in detail about how different systems (solid, liquid) can provide a versatility in their behaviour on various surface and interfacial textures. Then, emerging applications of such surface and interfaces according to recent progress in this budding field of research will be highlighted.

1.1 Background

Next generation device technology inspired from naturally existing surfaces require smart physics to exhibit multifaceted characteristics. This has potential benefits such as structural compatibility with deformable surfaces and structures, high resilient device performance and improved system configurability under varying environmental conditions. Smart surface and interface inspired applications have grown into one of the more interesting technologies for next generation applications[6-8]. Inspired by the naturally active surfaces and its performance at extreme environment conditions which can undergo multiple states of structural configurations are the basis of our device.

Subjecting to external stimuli, smart surface/interfaces can undergo in-plane/out-of-plane deformations and transfer surface energy into multimode deformations with reversible configurations at extreme conditions[9-12]. The aim of work presented in this thesis is to investigate structure-property relationship on the naturally inspired surface physics phenomenon and realized in the device/structure design and development. The main objective is to develop functional smart surfaces which can behave fundamental surface physical/chemical transition to create hierarchical surface energy transitions, and hence to fabricate devices for multi-faceted applications at extreme environmental conditions.

1.2 Aims and Objectives

The overall aim of the project is to exploit a series of nature inspired surface structures that can present surface physical/chemical transition/switches at a solid-solid, solid-liquid interfaces. Such exploration will be accompanied by corresponding structure-property studies to develop functional structure/device crossing multilengthscale from nanometer (10^{-9} m) level to macroscopic level (i.e. 10^{-2} m), hence, the project revolves around a range of advanced chemical, physical and mechanical techniques to facilitate the structure-properties knowledge.

Technically, the approach was performed by using micro-engineered surface to systematically exert a re-entrant structure with various kinds of materials – including immiscible polymers, inorganic materials, invisible gas-vapor layer that can enhance the stability of a solid/liquid composite interface. Specific considerations were given to the control of spatial interactions between solid, liquid and gas interfaces and their behaviour on a naturally viable surface. The objectives of this report are listed as follows:

a. Design and develop the smart surface and interfaces towards smart environmentally responding structures/devices.

b. Improving the instrumental systems to explore the desired structures/devices with defined applications.

c. Explorations of new theoretical model in understanding the dynamic behaviour at the surface interface on multiscale structural surfaces.

d. Integrating the surface physics and theoretical outcome for various extreme devices with defined boundary conditions.

1.3 Outline of thesis

Chapter 1: Introduction. A description of how the present project was inspired and its contributions to the extreme device structuring.

Chapter 2: Literature review. The multifaceted role of nature inspired surface and interfacial systems with their unique phenomenon are introduced. Classifications of naturally abundant and inspired surfaces/ interfaces are explained in detail. The smart material concept is provided, with a brief introduction on the theories behind device fabrication are also listed.

Chapter 3: Experimental methods. The in-lab techniques that put effect in surface fabrication with on-demand characterization methods including Optical Microscopy (OM), Droplet Shape Analyzer (DSA), Scanning Electron Microscopy (SEM), etc are explored in detail.

Chapter 4: We designed a novel non-compromised resistance towards corrosion with superior solar absorptivity and thermal emissive porous aluminium surface via unexplored thermo-anodization route. We characterized the role of temperature in regulating the porous structure of the anodic surface and elucidate the effect of surface chemistry on the superwettable behaviour for aerospace engineering.

Chapter 5: We designed a stimuli responsive switchable surfaces to provide both lipophilic, oleophobic characteristics. Through the conjunction of novel surface

instability induced wrinkle on a 3D printed groove structure and injected stimuli responsive hydrogel pattern, the overall superwettability of the surface could be reversible as well as reconfigurable. We characterize the superwettability of the surface by investigating the transition of surface topology and surface wetting property using a structure-property relationship.

Chapter 6: Upon nature's inspiration of how water droplets dynamically bounce on a heated surface, we designed a novel thermoelectric converter based on new phenomenon, elastic Leidenfrost effect. Counterintuitively, by simply elastically tuning the water droplets and confining their dynamic bouncing behaviour with a tube, a non-chaotic bouncing pattern is achieved. To translate the elasto-kinetic energy, a piezoelectric disc is fixed on the top for the spheres to impact and deform to generate electricity. Our design philosophy will provide a novel cost-effective, portable and completely reconfigurable energy harvesting system, and will find extensive applications in geo-thermal resources.

Chapter 7: By selectively fabricating a surface with alternating hydrophilic/ hydrophobic structure, a pinning interface is introduced. This facile technology with an in-built ionic hierarchy can be further exploited to realize a hydrogel bilayer structures with 3D reconfigurability undergoing elastic deformation driven by in-plane and through thickness elastic mismatch.

Chapter 8 : We will further reveal the underpinning parameters of the Leidenfrost activated polymer construct by developing a viscoelastic model and thermo-mechanical model to the pin the basic mechanisms towards improved system's stability.

Chapter 9: Conclusion and future possibilities. Overall summary on current research work based on nature inspired surface/interfaces and its corresponding applications under different extreme conditions are provided.

Chapter 2

Literature Review

2.1. Elasticity of materials

There are many intrinsic elastic materials such as elastomers, liquid metals, stimuli responsive polymers, etc which can achieve the flexibility and programmed structural reconfigurations (the capacity for being stretched) corresponding to the external stimuli. Of selective importance, hydrogels are soft, highly tunable and conformable hydrated materials[13, 14]. For a deformable soft system, hydrogels rely on their reverse configurability behaviour[15-19] which is defined by its shear modulus(ratio of shear force per unit area (stress) to the ratio of shear deformation over initial length (strain) and elastic modulus(ratio of the stress to the strain along that axis). The interrelated characteristics of the hydrogels has led to defining a fundamental relationship between swelling ratio, shear modulus and crosslinking density as shown below:

$$G = RT\rho_x Q^{\frac{-1}{3}} \quad (1)$$

wherein, ρ_x is crosslinking density, Q is swelling ratio, R is gas constant, T is absolute temperature and G is shear modulus. However, the relationship between crosslinking density and elastic modulus is given as:

$$E = (3\rho_x RT)/M_C \quad (2)$$

wherein M_c is molecular weight between elastically-active crosslinking points, and E is elastic modulus. These properties are completely interrelated and can assist in designing hydrogels for various applications. Crosslinking density is defined as the number of chain segments present between crosslinks, whereas swelling ratio is the ratio between swollen weight to dry weight.

As crosslinking density increases, the elastic modulus increases and the molecular weight between elastically active crosslinking points decreases. Hence, upon experiencing a certain force on the material, the structure becomes distorted and the adjacent crosslinker align to each other allowing for maximum deformation. On a reversible note, when the hydrogel structure is not under the influence of an external force, it reconfigures itself by pulling the crosslinkers back to their original shapes.

2.1.1 Mechanical behaviour of elastic materials

As mentioned earlier, the overall intrinsic mechanical behaviour of the soft material is characterized by its stiffness, elasticity, toughness, tensile properties, ductility, and fracture strength at extreme environment. Ideally, the deformation of the elastic materials is an energy dependent process called as elastic energy. Energy storage is not heavily lost when under stress, rather reconfigures itself both structurally and mechanically undergoing an elastic deformation. When an elastic material is deformed for many cycles, the elastic deformation is translated into a plastic deformation region under which the reverse switchability of the polymeric chains is diminished. The elastic deformation of the materials is defined by Hooke's law which relates the stress (σ) to strain (γ) as follows:

$$\sigma = E.\gamma \quad (3)$$

To achieve an increased elastic modulus for the soft materials, their crosslinker concentration is often altered and helps in many useful applications.

2.1.2. Elastic materials

Intrinsically and extrinsically different with rigid materials such as marbles, rock, etc which do not deform easily under an external stimuli, elastic materials such as hydrogels are widely studied due to its covalently connected elastic nature, which makes the theory of entropic elasticity applicable[20,21]. Some of the hydrogel materials such as Polyacrylamide (PAAm), etc have multi-faceted characteristics with applications in the area of water treatment[22], oil recovery[23], agriculture[24], medicine[25], as well as in most recently developed hydrogel devices. PAAm based extreme devices are profited by its high water content, high stretchability, elasticity, and transparency. The mechanical behaviour of the PAAm hydrogel depends on the modulus, reverse structural and functional configurability stretchability and fracture toughness based on its molecular variables. By playing with the crosslinkers such as N,N'-Methylenebis(acrylamide) (MBAA), the hydrogels can be modulated to be soft and brittle or stretched more than its initial length. While increasing the concentration of crosslinkers, the overall elastic modulus is pronounced with shortening of the average polymer chain length in the PAAm network and vice versa(**Fig 2.1**). The advantages of PAAm inspired hydrogels are its tunability to exhibit swelling, large deformation, instability, fracture, viscoelasticity, poroelasticity under defined environment conditions. PAAm based elastic materials have been widely exploited by controlling its elastic reconfigurability in extreme device applications such as

epidermal electronics[26], flexible artificial skins[27], energy harvesting devices[28], bio-medical electronics[29], presser sensors[30] and soft robotics[31].

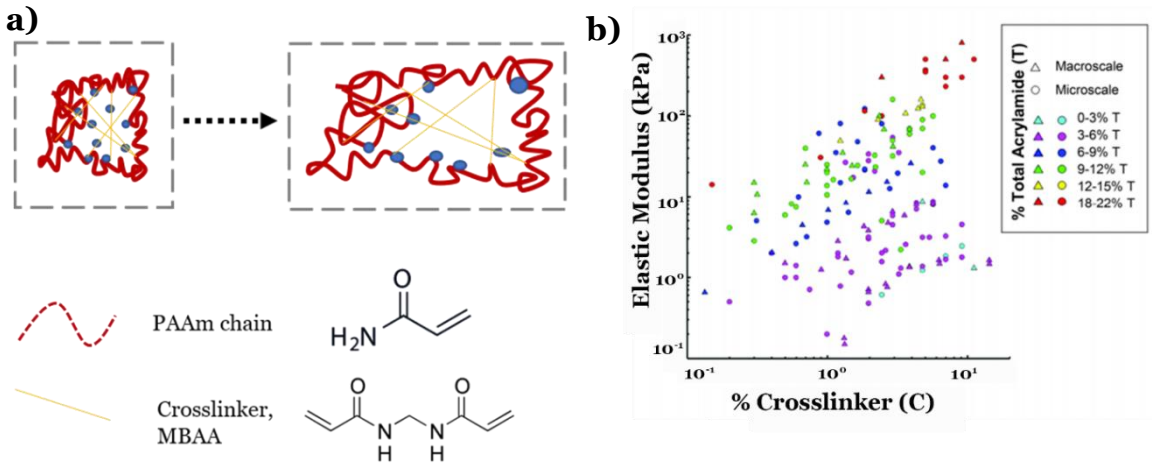

Figure 2.1 a) Structural configuration of polyacrylamide hydrogel; **b)** Wide range of stiffness behaviour exhibited by polyacrylamide system with various crosslinking concentration[20].

2.2 Governing principles exploited for liquid based system manipulation

2.2.1 Wettability theory

The definition for the wettability of surface is based on two common factors called as hydrophilicity and hydrophobicity. Wetting theory provides different surface physics which could be tuned by physically or chemically modifying the surfaces. The fundamental surface conditions[32-34] are described as

- surfaces manifesting a fixed contact angle higher than 150° are termed as superhydrophobic/superoleophobic;

• surfaces with intermediate contact angle values of 90° and 150° are hydrophobic /oleophobic;

• surfaces whose overall contact angle lies below 90° are said to be hydrophilic/oleophilic.

The contact angle measurement is the standard experiment to determine the surface wetting state[35, 36]. The surface wettability is governed by Young's law, which determines the work adhesion nature of the liquid medium on the surface under thermodynamic equilibrium. The Young's equation is stated as below

$$\gamma_{SL} = \gamma_{SV} - \gamma_{LV} \cos\theta \quad (4)$$

where γ_{SL} is the interfacial energy between solid and liquid phase, γ_{SV} is the interfacial energy between solid and vapor phase, γ_{LV} is the interfacial energy between liquid and vapor phase, and θ is the static/dynamic equilibrium contact angle of a liquid droplet interacting on the surface. However, the Young's equation is only applicable for a flat and homogenous surface.

2.2.2 Wenzel and Cassie-Baxter theory

It is challenging to obtain the true contact angle at the interface of liquid droplet on a rough or heterogenous surfaces such as porous[37], wrinkled[38], textured[39], etc, as the localised tiny feature brings complicated and devised arbitrary interactions. To capitalize on this disparity, the Young's law has been further developed by taking the surface roughness into account. Firstly, Wenzel proposed a relationship between surface roughness and the degree of surface

hydrophobicity, which is measured by water contact angle. In short, Wenzel equation[40] is defined as :

$$\cos\theta_{rough} = r\ cos\theta_{smooth} \quad (5)$$

wherein the contact angles of rough and smooth surfaces are represented as θ_{rough} and θ_{smooth} along with a roughness factor, r. Wenzel theory is highly applicable in defining the static contact angle of the droplet, which remains pinned to the surface. Whereas, Cassie-Baxter state is considered when a liquid droplet is in dynamic state between solid-liquid and liquid-vapour interfaces.[41] In Cassie state[42], liquids are assumed to only contact top of the rough surface, and air pockets trapped underneath the liquid are considered completely non-wetting. Therefore, compared to Wenzel state, Cassie state is deemed to be a composite state (**Fig. 2.2**). The apparent CA in Cassie state (θ_c) is described as:

$$\cos\theta_c = f_s cos\theta_s + f_v cos\theta_s \quad (6)$$

where f_s and f_v are area fractions of the solid and vapor, respectively. Since $f_s + f_v = 1$, $\theta_s = \theta_Y$ (Young's contact angle), and $\theta_v = 180°$, eqn (6) can be written as eqn (7):

$$\cos\theta_c = -1 + f_s(cos\theta_Y + 1) \quad (7)$$

In some situations, such as under the conditions of droplet press, impact or vibration, liquids partially fill the open voids on a rough surface, therefore, an intermediate state between Wenzel and Cassie state would be obtained[43].

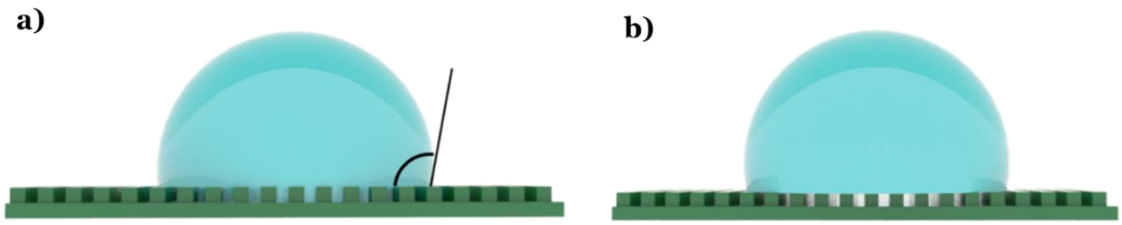

Figure 2.2 Illustrations of droplet wetting in **a)** Wenzel state and **b)** cassie state

2.2.3 Isotropic and anisotropic wetting

In real life, isotropic wetting with identical contact angle (CA) measured in all directions is very rear, due to the diversity of nature. Conversely, anisotropic wetting commonly occurs when contact line encounters physical (topographical or structural) asymmetry and/or chemical heterogeneity on solid surfaces, which results in non-spherical droplet shapes. The size of a droplet and the variability of the surface property should be controlled within a suitable range to avoid a pseudo isotropic wetting case when the variability of the surface property is on a very small scale compared to a droplet, and rule out the condition that the droplet is too small compared with the characteristic units of the anisotropic wetting surfaces to realize anisotropic wetting behaviour (**Fig. 2.3**).

Anisotropic wetting phenomena include both static properties (different static CAs in different directions) and dynamic properties (different sliding angles and directional movement). The anisotropic movement of droplets or liquids in specified directions has shown great potential for self-cleaning, microfluidic, and fog collection. Generally, a stationary droplet on a solid surface is subjected to counterbalanced external forces. Once the external forces are unbalanced, which means the driving force is large enough to conquer the resistance, anisotropic wetting occurs. Motion of liquids is subjected to resistance force F_{Res}. The F_{Res} is

caused by CA hysteresis (difference between the advancing CA, θ_{Adv}, and the receding CA, θ_{Adv}, of a droplet), and can be described as:

$$F_{Res} \sim \pi R_{0\gamma} (Cos\theta_{Res} - Cos\theta_{Adv}) \quad (8)$$

where R_0 is radius of the droplet, and γ is surface tension of the liquid. In general terms, the reason for these various anisotropic wetting behaviours could be classified into two types: non-uniform surface wettability and asymmetrical geometric shapes of the surface.

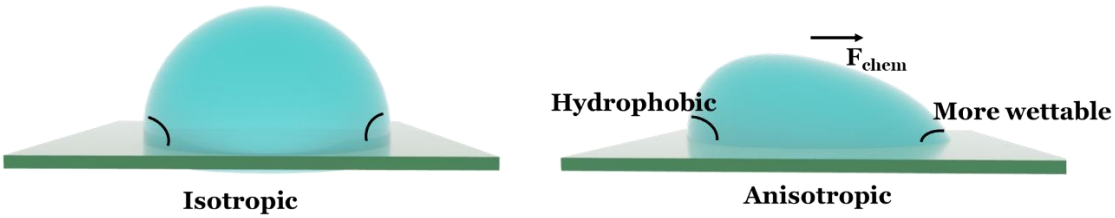

Figure 2.3 a) Isotropic and **b)** Anisotropic wettability control

2.2.4 Liquid infused wetting theory

Another derived wetting condition is achieved by lubricating the surfaces with slippery materials that can handle low surface tension liquids without causing mechanical damage[44-46]. The slippery surfaces can be created based on three conditions wherein, (i) the active lubricant and the static/contractual liquid droplet is immiscible; (ii) the lubricating materials should wet the surface with higher affinity over the impacting liquid droplet. **Figure 2.4** represents the various droplet behaviour characteristics involved when a liquid droplet contacts the lubricated layer. For example, when the lubricated layer is made of fluorinated oil and comes in contact with another liquid droplet, the liquid droplet undergoes either of the following conditions[47]. The impacting liquid droplet is completely conversed by the underlying lubricated oil layer when spreading parameter $S_{ow(a)} > 0$ making it highly hydrophilic or withholds its

original shape if $S_{ow(a)} < 0$ proving the surface to be highly hydrophobic. The spreading factor $S_{ow(a)}$ is defined by

$$S_{ow(a)} \equiv \gamma_{wa} - \gamma_{ow} - \gamma_{oa} \tag{9}$$

wherein, γ_{wa} is the water–air surface tension, γ_{ow} is the surface tension of oil–water, and γ_{oa} is the oil–air's surface tension. Hence, depending on the above phases (such as water, air, oil) the lubricant oil can exhibit increased wetting of the surface, partially wet or avoid wetting. As discussed earlier, the wetting behaviour of the oil is also determined by the substrate roughness at the the contact line, where $cos\theta = (\phi - r)/(r - 1)$ inwhich r is the surface roughness factor which was used in Wenzel's equation and ϕ is the liquid's occupying unit area at the surface similar to the fraction factor in Cassie's equation. Hence, if the lubricated layer completely wets the surface, the liquid droplet will exhibit a dynamic behaviour, whereas, when the lubricant is not present, the droplet can pin to the surface and exhibit a Wenzel state, or the droplet can slide over the lubricated surface partially if the lubricated covers half the surface.

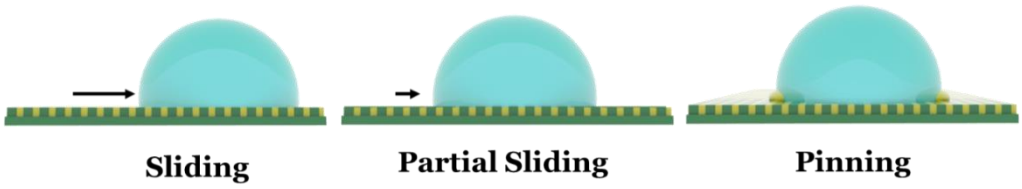

Figure 2.4 Different regime of droplet behaviour on a slippery infused surface

2.2.5 Contact Angle Hysteresis

Derived from the above wetting theories, it is of pristine importance to understand the interaction of low-surface energy and surface roughness for superhydrophobicity[48]. Surface wetting behaviour is widely influenced by the surface topography wherein the surface roughness plays a critical role. Theories such as Wenzel state, Cassie-Baxter state defines the contact angle of the surface when the surface is no longer flat, or no surface roughness is being involved. However, the above theories have considerable limitations to illustrate the dynamic liquid behaviour on rough surfaces. With this perspective, the contact angle hysteresis is defined as, when a liquid droplet is dispensed onto a rough surface and more volume of liquid is being added, the droplet starts to expand[49]. As, the volume steadily increases, the contact angle shifts reaching a critical value called as advancing angle (θ_A) and when the liquid is drawn, the overall volume decreases making the contact line recede. This is called as receding contact angle (θ_R). The contact angle hysteresis (CAH) is calculated based on the difference between advancing and receding contact angle, and it is always noted that CAH will be higher in Wenzel state as the liquid volume is higher and a lower CAH is achieved in Cassie state as shown in **Fig. 2.5**.

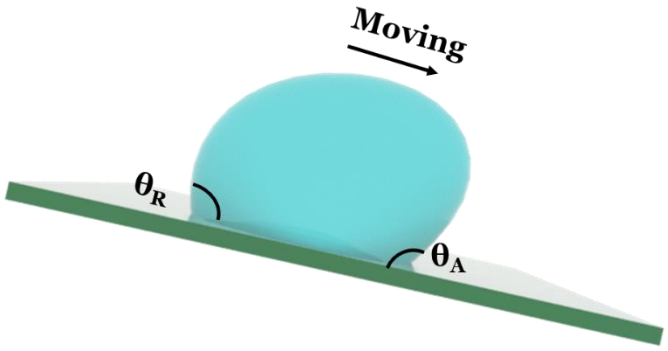

Figure 2.5 Schematic of contact angle hysteresis calculated using advancing and receeding angles

2.3 Wetting enabled system embodied motion behaviour

Most naturally abundant systems orchestrate a superior functionality and adaptability to extreme environments via conforming towards range of liquid states at their surface and interfaces. In general, superhydrophobic surfaces with static contact angle larger than 150° can be explained by the complex hierarchical surface architecture of the lotus leaves resulting in various droplet dynamics. One such example is the directional liquid droplet motion behaviour on butterfly winds which is attributed by its intrinsic surface architectures. Another classic example is the liquid infused smooth interfaces found in nepenthes pitcher plant that has the potential to eliminate contact line pinning of various surface tension liquids.[50] Hence before delving onto the theories that govern the droplet motion, it is of pristine importance to unravel the droplet motion behaviours influenced by various surface architectures and interface conditions as shown in **Fig. 2.6**.

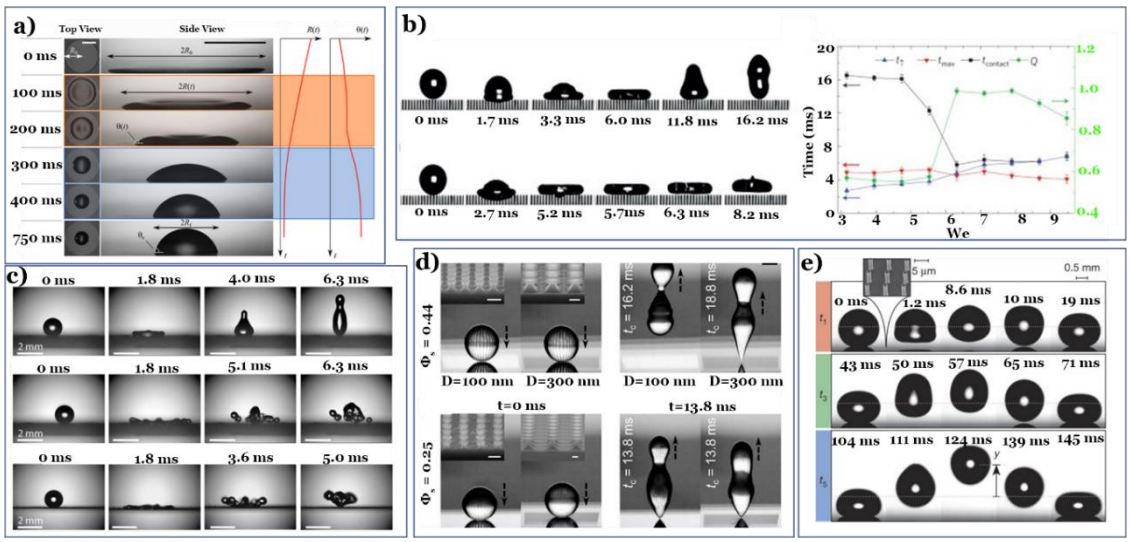

Figure 2.6 Strategies towards droplet manipulation on various surface and interfaces **a)** Dewetting behaviour of a liquid droplet from a smooth surface[51]. **b)** Impact and spreading behaviour of an axisymmetric droplet with defined incoming velocity[52]. **c)** Droplet impinging on a nanoflower decorated interface with shape retention,[53] **d)** Reduction of contact time of jumping droplets,[54] **e)** Spontaneous bouncing of liquid droplets with restitution coefficient close to unity based on the underlying air-pressure interface[55].

2.3.1 Dynamic liquid system under contact

Dynamic droplet behaviour at the surface contact interface can result from various factors such as the wettability[51], impact velocity[52], surface textures[53], contact time[54], interfacial nature[55]. We should clearly understand that the interaction between the liquid droplet and the surface interface is extremely transient and dynamic in principle which is highly dependent on the weber number of the droplet $We = \rho v^2 D_o/\gamma$ and the Reynolds number $Re = \rho v D_o/\mu$ which measures the fluids inertia with respect to surface tension and viscosity. Here, ρ, D_o, and v represent the density, diameter and impact velocity of the liquid drop, respectively, and γ and μ are the surface tension and dynamic viscosity of the liquid drop. Under dynamic behaviour, the droplet with higher We and Re leads to formation of secondary droplets and ultimately splashes; whereas, at lower We region, the drop is characterized by small deformation with high restitution coefficient(α) due low/negligible energy dissipation. In principle, droplet bouncing with restitution coefficient (α) < 1 occurs at the capillary-inertial regime wherein the overall kinetic energy is translated into surface energy, and whereas $\alpha > 1$ is characterized by viscous-inertial regime which is due to the viscous force.

One such example is the droplet motion along a surface treated silicon wafer with alkyltrichlorosilane in a diffusion-controlled process which provided a hydrophobic interface. The droplet motion was directed by an imbalance in the forces acting on the solid–liquid contact interface at opposite sides of the droplet[56]. The droplet motion can also be directed by treating the surface via coalescence or condensing droplets with the aid of mechanical attenuation. By constructing surface pillars, a dynamic surface wettability gradient was

established that are prone to external stimuli with controllability towards space and time. Beyond this, surfaces with wedge like features can drive droplets along the surface by laplace pressure and tuning the overall asymmetric shape of the surface textures[57]. In other words, the overall contact angle hysteresis should be driven by surface tension that results in dynamic contractual motion behaviour of the droplet. As an alternative to physically functionalize the surface, stimuli responsive chemical moieties can be exploited to impart reverse configurability with different wetting features. A classic example is the addition of azobenzene groups which exhibits dual configurations when enabled under different light wavelengths and can therefore be locally controlled to achieve droplet motion/transport along the surface[58]. Also, widely exploited silanes can be adhered to the surface to achieve controlled surface charge density gradients that promotes droplet motion for wider applications.

2.3.2 Jumping liquid droplets

On an important dynamic behaviour exerted by the liquid droplets, wider audience have been attracted owing to it multifaceted practical windows in heat transfer, anti-icing, and energy harvesting. The droplets bouncing is often considered due to the vapor condensation process that results in droplet impingement as seen in several natural systems such as self-cleaning cicada wings[134] and water strider legs[59]. One key point in the design attribute of the surface/ interface is to achieve droplet repulsion from surface as swift as possible by reducing the contact time between the droplet and the surface. Conventionally, the droplet gets suspended over the surface without physically contacting via an invisible air cushion to induce asymmetric and fast recoiling. Wang et al. designed a novel liquid repellent surface to induce “pancake bouncing” phenomenon by

reducing the contact time to 80% by revising the droplet capillary energy stored into a vertical kinetic motion to lift the drop[146]. The bouncing velocity is scaled as $\sqrt{\frac{\gamma}{\rho D_o}}$ where the total surface energy is translated into kinetic energy. However, the measured drop jumping velocities were significantly smaller than that predicted based on the capillary-inertial scaling law[60]. Carefully tuning the surface could reveal the jumping of condensate drops that either results in departure or adherent to the surface. Recently, droplet impact on liquid films have been experimented to understand that the spreading dynamics and the restitution coefficient was completely independent of the underlying liquid substrate and the bouncing of the droplet was attributed to the robust air layer present at the interface[61]. And by decreasing the environmental pressure, the droplet was found to be jumping on the surface which was dictated by the fast evaporation underneath the droplet surface and interface. Another strategy to exert bouncing phenomenon is by undertaking a phase-change process at the interface wherein, heating the surface above the droplet's boiling point leads to formation of an integral film at the impact area. By carefully designing the surface, droplets rebound can be directed towards high heat transfer regime by breaking the wetting symmetry[62]. And, recently, similar droplet rebound was observed on surface exhibiting cold temperature that demonstrated the possibility of complete bouncing[63]. Hence, there are several factors/principles that plays a wider role in defining the droplets motion behaviours and dictating them towards extreme device fabrication.

2.3.3 Invisible Gas-Vapor layer dictated system manipulation

A widely known kitchen phenomenon wherein, a drop of liquid upon placed on a surface heated above its boiling point tends to hold its structural integrity. Researchers believed that, a portion of liquid at the solid-liquid interface gets vaporized and trapped beneath it. And this vapor functionalizes as a thermal insulation layer to the liquid droplet protection by regulating vapor layer and extending the overall lifetime of the droplet[64-68]. The fundamental surface physics behind this interface is complicated, however, on a general state, the invisible vapor layer significantly reduces the friction between the droplet and the surface and suspends it away from the surface as shown **Fig. 2.7**[69]. This has been defined as static Leidenfrost effect by Johann Gottlob Leidenfrost[70]. Liquid

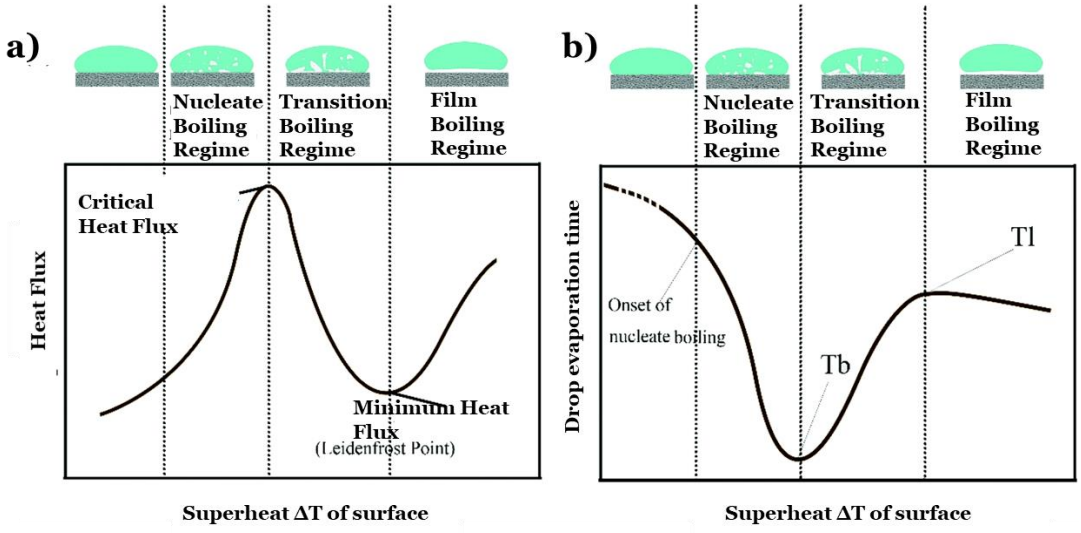

Figure 2.7 Different regime exhibiting by liquid droplets on a surface with temperature above its boiling point towards **a)** heat flux and **b)** evaporation time[71].

droplets whose elasticity is almost zero were found to be self-propelled on a heated textured surface interface[72-76]. The propulsion was originated due to the asymmetry of surface and the viscous force which regulates the flow of vapor underneath it for a directional motion[77,78]. By altering the surface interface by

texturing or surface coating or changing temperature, even dry ice which belongs to sublimating solids can exhibit a similar friction-free motion such as dry ice[79,80], can exhibit the same frictionless and thermally insulating properties as a droplet at high enough temperature above their sublimation point. Such a dynamic Leidenfrost phenomenon which coexists in extreme nature can inspire us to device different gadgets which are both robust and environment friendly. In this section work, we will consider the basic regime analysis obtained when a liquid droplet meets the gas-vapor interface on a solid surface. Fundamentally, when the liquid droplets nucleate when the surface reaches lowest temperature boiling regime, whereas, it boils when the temperature is in the transition boiling regime[81,82]. However, the droplets get suspended on the surface when the temperature is above the film boiling regime as the invisible vapor layer is formed. Droplets which are supported by the above vapor layer evaporates with time as the vapor temperature increases highlighting a critical heat flux requirement to achieve a localized minimum droplet lifetime. The Leidenfrost behaviour is found to vary significantly when the surface texture is altered owing to multi-physics behaviour[28,83]. Modulating the surface interface with porous structures was studied extensively by Avedisian et al[84] and concluded that the Leidenfrost temperature increases as the surface pores are raised. A lower evaporation rate is achieved by reducing the vapor layer at the solid-liquid interface for sustainable droplet moment. Several parameters and models have been tested to understand the extension of life of the droplets on a hot substrate [85-87]. One of which is Kim et al[88] who discussed the role of surface roughness parameters, wettability and nanoporosity on the Leidenfrost behaviour of the droplets. Increasing the surface roughness could raise the Leidenfrost temperature of water to 359°C (up from 274°C) on a silicon oxide surface [89]. Sublimating solids, such as dry ice, can also exert similar frictionless and thermally insulating characteristics as a liquid

droplet[77]. The qualitative dissimilarities between the solids and liquid droplets are their shapes, lack of reconfigurability upon deformation, and internal flow. Hence, altering the surface interface physics could result in an increased heat transfer with reduced evaporation time[90-92]. Such physics is of wider interest in the field of cooling, drag reduction and liquid transport. These effects could potentially assist in devising energy harvesting devices which used waste heat as a source of energy input[93-95].

2.3.3.1 Leidenfrost assisted Dynamic Activities

The behaviour of a droplet upon collision with a hot surface is indeed very complicated and influenced by physicochemical characteristics of the drop as well as the surface/interface conditions[78, 96-104]. The possible dynamic activities for a liquid droplet include sticking to the surface, bouncing off, or splashing and splitting into smaller droplets, as shown in **Fig 2.8** The irreversibility of the droplet splash can be altered to produce a highly stable bounce-off condition by increasing the lamella. The initial kinetic energy of droplet should meet the essential criterion to achieve stable droplet dynamic nature on the surface. The droplet splashes when the impact kinetic energy exceeds the threshold value of the surface/interface leading to smaller satellite like droplets jetting out of its outermost perimeter[105-107]. To withhold the droplet's structure, it is often characterized by Ohneorge number, which is stated as:

$$Oh = \sqrt{\frac{We}{Re^2}} = \frac{\eta}{\sqrt{\rho\ \sigma\ d}} \tag{10}$$

wherein $Re=\rho ud/\eta$ is the Reynolds number. Therefore, the retraction of droplet can be influenced/modulated by reconfiguring surface/interface physics which in turn affects the capillary forces for various motion behaviours.

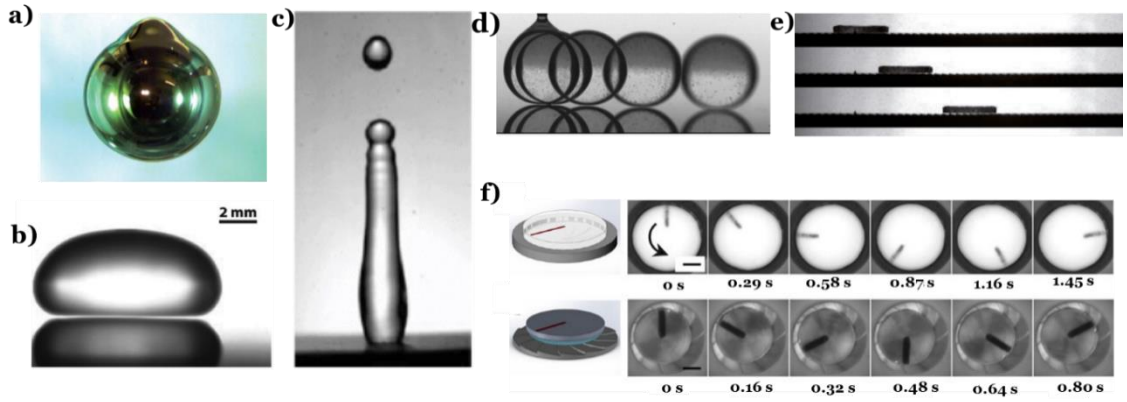

Figure 2.8 Leidenfrost assisted motions observed on various surface/interface parameters. **a)** Hidden vapor layer present on the surface of a heated steel ball propelling through a liquid bath[65]. **b)** Liquid droplet suspended on a heated surface by its own invisble gas-vapor layer[70]. **c)** Repulsion behaviour of impacting liquid system which eventually breaks down into tiny droplets due to zero surface integrity[105]. **d)** Self-propulsion of liquid droplet upon careful placement over a superhydrophobic coated heated surface[68]. **e)** Directional motion behaviour of a rachet(solid system) on a textured surface driven by hidden gas-vapor flow direction as an effective cargo transport[168]. **f)** Rotation of a sublimable solid system[45].

2.3.3.2 Factors assisting self-propulsion of non-elastic matter on different surface/interfaces

The Leidenfrost effect has substantial impact on the shape and motion behaviours of the non-elastic matter such as liquid droplets, solids, etc, as shown in **Fig. 2.8f**[73-76, 108, 109]. Unlike solids, liquid droplets can typically be axisymmetric and undergoes shape oscillations due to the shear viscous forces arising from the escaping vapor in a static state[46, 110-114]. However, on a dynamic scale, when the droplets approach the hot surface with a defined incoming

velocity, the upward force exerted by the invisible gas-vapor layer on a surface interface stabilizes the surface tension and deforms the film. As the temperature of the surface increases above its boiling regime, an air bubble is created at the surface-droplet interface which regulates the thermal flow [115]. Impinging droplet behaviour is normally calculated based on the velocity experienced by the droplets during impact and the energy gained due to repulsion from the gas-vapor interface. A clear phase diagram depicting the regime-wise droplet bouncing behaviour is considered by Biance et al[81], which show that a long dynamic cycle can be generated by altering the surface/interface with defects to regulate the impact velocities of the droplet.

Another approach to understand the dynamic nature is to consider the self-propelling behaviour of the droplets and solids along the surface. The motion is quite like how a liquid droplet behaves on a super-hydrophobic layer wherein, the wetting angle is lower resulting in decreased spreading of the droplet[113-119]. Self-propulsion can be realised by constructing the surfaces with designed architectures aiding in higher transition boiling regime. The vapor flow direction on a surface is the driving force for both the droplets and solids[71, 120-132]. Linke *et al* develop a fundamental understanding on the self-propelling behaviour of the droplets driven by viscous force interaction on a textured surface[133]. Grounds *et al* also showcased that the wetting contacts of the droplets can also alter the directionality of the droplet flow[134]. Li *et al* demonstrate conditions in which droplet propulsion can be directed on a topographically structured surface at extremely high temperature conditions. For those geometries which exhibits inhibition of droplet motion, a higher surface temperature can break the wetting symmetry of the droplet and provides higher heat transfer coefficient[135]. The study also proved that, by carefully modifying the surface interfaces, the droplets

can transport on their own which finds its applications in extreme places such as drug delivery, cargo transport, electronic cooling systems, etc.

2.3.3.3 Elasto - Leidenfrost behaviour

For liquid droplets whose surface tension can potentially lead to production of secondary droplets upon impacting with hot surface, or sublimable solids such as dry ice with higher Young's modulus limiting its deformable behaviour. In comparison to non-elastic systems such as liquid droplets, sublimable solids, etc, studies of Leidenfrost behaviour on non-Newtonian systems has received very low attention. And it is pristine importance to understand the materialistic properties of the elastic systems before approaching its usability in extreme engineering systems.

Impacts of elastically tuned hydrogel-based systems poses assorted insights onto the hydrodynamics and heat-transfer within the viscoplastics or elastic fluids. The addition of an additive to the liquid systems is seen to greatly inhibiting the splashing phenomenon or the formation of sticky regime during the contact boiling phase[136,137]. The inclusion of elastic component to the system significantly reduces the spreading diameter of the systems and improves the dynamic rebound of the droplets(**Fig. 2.9**)[138]. In doing so, they also reduce the liquid surface tension at the surface by adsorbing to the air-water interface.

Under a specific Leidenfrost parameter, the elastic droplets have the tendency to bounce off the hot surface by harvesting surface thermal energy into kinetic energy. However, in terms of energy consumption, the total energy reserved within the polymeric droplets spent to deform the surface which affects

the overall contact time, sphere deformation and overall energy consumption. In contrast to the above viscoplastics, the bouncing of an elastically structured sphere can restructure itself by converting the kinetic energy gained into elastic energy and under a cyclic conversion from elastic energy into kinetic energy[139]. The overall work spent for rebound of the elastic sphere is given as[140]:

$$U_{polymer} = \pi b^2 w \tag{11}$$

wherein, b^2 is the contact radius of the sphere, and w is the work of adhesion per unit area. And the elastic energy gained by the elastic sphere is given as:

$$U_{Elastic} = \frac{32}{45} E R^{\frac{1}{2}} \delta^{\frac{5}{2}} \tag{12}$$

wherein, δ is the normal compression, R is the radius and E is the elastic modulus of the elastic sphere. This behaviour has been identified in very few studies with limited knowledge about the role of temperature and elastic component of the system. It is therefore surprising to underutilize the potential of such a cyclic energy conversion cycle for extreme devices such as energy harvesters, soft robotics, medical applications, etc.

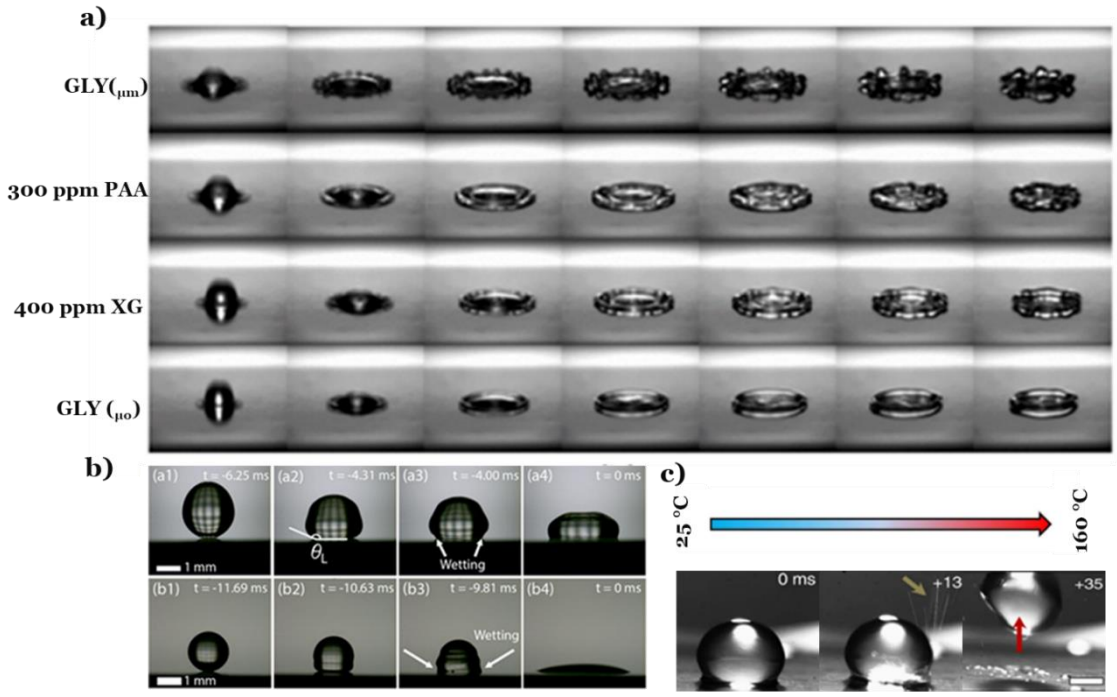

Figure 2.9 Various contractual and rebound dynamics of **a)** viscous[137], **b)** elastically tuned liquids[138] and **c)** soft solids on a heated surface interface[139].

2.3.4 Other liquid based system manipulation theories

In addition to the above listed theories followed in nature, some creatures exhibit highly functional wetting property which is exploited for manipulating liquid droplet behaviour. As discussed earlier, the sliding or rolling characteristics of the droplets can be distinguished based on the droplet sliding angle especially after the vast studies on pitcher plant. The *Nepenthes* plant is widely inspired towards novel concept of liquid drainage which are ideally used in fog harvesting applications. The liquid drainage concept can be further altered to repel the impacting droplets for applications in smart windows. It is proved that the droplet collection or motion is achieved through the liquid infused layer on the pitcher plant which can be further enhanced by the application of external stimuli. One such stimuli is based on the wetting or shape gradient that allows the liquid systems to slide[141], bounce[142] or hop[143] based on the applications as shown in **Fig. 2.10**. Another way is to allow liquid based systems for

manipulation is via electrowetting. It involves reduction of the solid-electrolyte contact angle via an external applied potential difference. Briefly, the

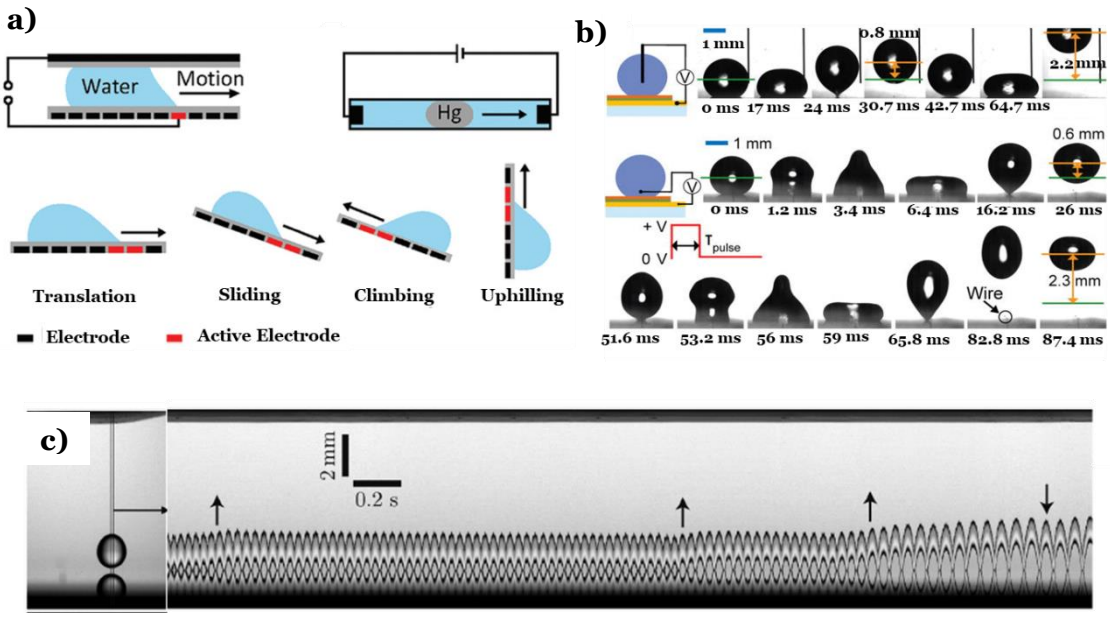

Figure 2.10 a) Mechanism of droplet motion controllability using electrowetting[145], b) Dynamic droplets under electrowetting[146] and c) combination of leidenfrost and electrowetting towards sustained droplet bouncing behaviour[146]

administration of the voltage potential gives rise to electric double layer at the solid–liquid interface which can be manipulated to either spread the liquid droplet or repel from the surface. Whitesides group have been the forerunner of developing such electrically attenuated droplet motion system resulting in timed liquid motion upon request[144]. Electrowetting for droplet repulsion in a vertical manner was also studied when the droplet is placed under an AC electric field that provides enough thrust energy for the droplet to bounce and ceased when the field was removed[145]. For sustained liquid droplet bouncing on the surface, electrowetting was administered on a Leidenfrost activated droplets which led to continued bouncing until the droplet evaporates. It is believed that administration of two stimuli/phenomenon can provide the necessary kinetic and potential energies typical to elastic bouncing as shown in **Fig. 2.10 c**[146].

2.3.5 Summary

The above chapters present the generalized approach towards demonstrating the basic wetting conditions exploited towards liquid based system manipulation such as isotrophic and anisotrophic with theories such as Wenzel, Cassie-Baxter governed during low temperature wetting events and high temperature droplet manipulation using Leidenfrost phenomenon. The above theories provide a multi-dimensional thermodynamic approach to the effects happening at solid/liquid interfaces. Wetting dynamics have been kept pure in a microscopic approach with new insights developing from the wetting physics such as Wenzel, Cassie and other extreme condition. For example, as the liquid droplet moves over wetting gradient, the droplet motion is further promoted due to reduced capillary force without any external energy consumption. These static and dynamic theories are of high importance with both fundamental and applicative points of view that governs the droplet characteristics on various natural and artificial surfaces. Ideally, contact line forces supports explicit mechanical probe onto various biological matter, wherein, a dynamic variation of solid angle of the impacting surface serves as a model for theoretical development. Although the exquisite theories have been outlined in this section, research on their partnership under different surface conditions needs further exploration. As the researches about the wettability conditions to control the droplet dynamics on the surface are established partially, manipulation of such droplet based systems present significant practical implications. The wetting theories provides insights onto controllability over mass, momentum and energy between the liquid based systems which will open numerous technological applications in soft robotics, droplet transportation and manipulation, energy harvester, etc.

2.4 Progresses on Nature Inspired Functional Structural Interfaces

This chapter offers an overview of the smart functional surfaces and interfaces which are present abundantly in nature and inspired from them. The functional surfaces will render a large potential of functions with multifaceted, bottom-up, self-reconfigurable and replenishable characteristics by following fundamental wetting theories towards environment adaptations[147-152]. Such innate functional characters aid in increased level of adaptivity to achieve dynamic interactions with the surrounding environment. Functional surfaces reach immense level of orchestration enabled by well-crafted manipulation[153-157]. Progresses will begin with the fundamental exploration and implementation of nature/nature-mimicking unique properties of naturally existing surfaces and its counterparts, followed by their applicability in extreme device fabrications and applications. Consequently, the incorporation of such functional surfaces and interfaces in extreme real-world applications with experimental observations and unravelling the governing theories will also be discussed.

2.4.1 Nature abundant surfaces

A variety of naturally prevailing surfaces possess extreme hidden surface physics; for example lotus leaves provides a superior dewetting property[158], hot cooking pan provides thermal transport behaviour[159], gecko feet[160] which provides different surface textures for striking nano-templates surfaces found in nature possess superhydrophobic properties; for example row beetles[161], insect wings[162]. One characteristic of these nature surface is their hidden surface physics that can provide multifaceted surface hierarchy for varied applications.

Naturally existing surfaces provides various forms of inspirations and captivating properties such as self-cleaning[163-165], soft actuations[166-168], power generations[169-172], etc. Accordingly, inspiration from nature provides new exciting standard in development of smart, cheaper, adaptable and highly efficient engineered surface for extreme environmental conditions.

Nature provides inspiration to produce smart surfaces when compared to a complicated biological mimicry. Less complex special architectures and surface conditions have received immense attention. Many examples can be pivotally seen in nature to represent extreme surface physics such as hydrophobic lotus leaf, highly ordered microstructure of beetle shells, hot planar surfaces, etc(**Fig. 2.11**). One highly regarded feature of smart surface is their responses to uncommon environmental catalyst and their drive towards surface interface instabilities.

Widely speaking, the surface interfaces present in nature are classified into three-phase interface or the two-phase interface. One such example is the prevalence of textured surfaces on lotus leaves that offers both high contact angle and low contact hysteresis with enhanced superhydrophobic property. Two-phase surface/interface interactions include but not limited to solid/solid[173,174], liquid/liquid[175,176], solid/liquid[177,178], solid/gas[179,180], etc. For example, heating up a solid surface to an extreme temperature provides an invisible gas-vapor layer on the solid surface interface which provides directional movement of liquids, solids, etc. It is attractive to capitalize on such instabilities for designing stimuli responsive devices with high fidelity and multi-tunability. Such naturally prevailing surface interfaces can be harvested for various tasks such as channelling of power, motion, structural behaviours, etc for multiple applications

in the field of tuneable optics, stretchable electronics, energy harvesters, microfluidics, aerospace engineering, etc.

2.4.2 Nature mimicking surfaces

Inspiration from nature to unravel the hidden mechanisms of surface physics is the most efficient way to design and fabricate nature mimicking surfaces. Selected examples of nature-inspired surface/interfaces with hidden surface theories for extreme applications are shown in **Fig. 2.11**.

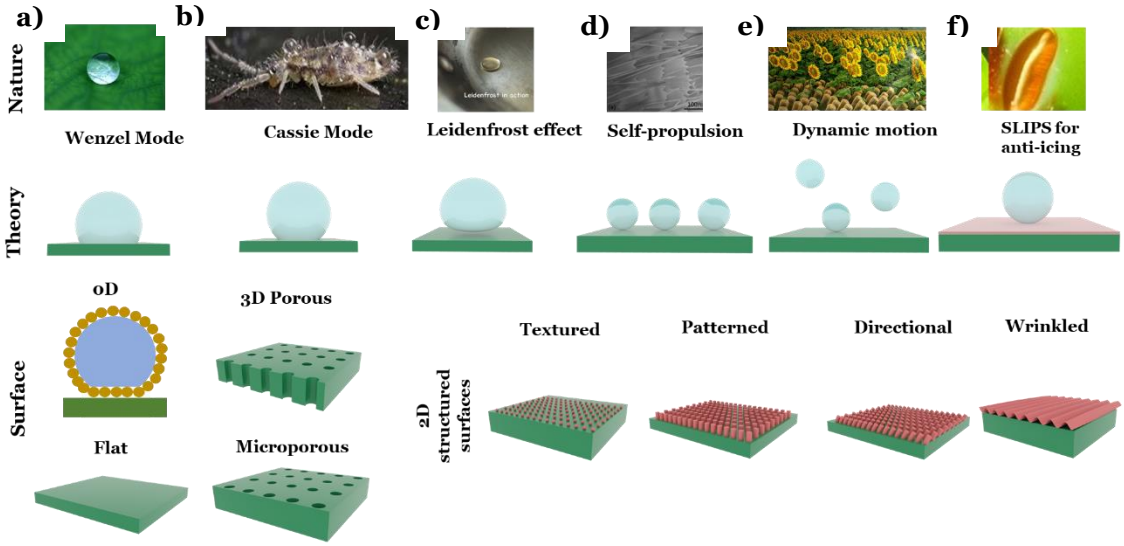

Figure 2.11 Overview of the different nature/nature mimicking surfaces that are possible in exhibiting wide range of surface physics principles for extreme device applications. **a)** Superhydrophobic lotus leaf exhibiting Wenzel state[158]; **b)** Rove beetles with extreme liquid repulsion[161]. **c)** Leidenfrost effect observed on a cooking hot pan[159]. **d)** Liquid mobility observed on a textured butterfly scale[162]; **e)** Guided propulsion of liquid based systems inspired from sunflower army[176]; **f)** Liquid/oil separation and anti-icing property surface inspired from nepenthes plant[171].

The design philosophy of nature mimicking surfaces to introduce wide wetting theories can be extended from various structural surfaces developed using 0D particles, 1D fibres, 2D structures, 3D porous materials with wider

dimensionalities. As similar to randomly textured lotus leaf surfaces, densely wrinkled mosquito eyes, or even naturally present hot exhaust automobile pipes releasing waste heat can inspire several micro-nanostructured biological surfaces, these structural features can motivate various people to style and construct multiple structural anomalies for for carrying out multi-faceted applications.

2.4.2.1 0D particles

Due to the intrinsic resistance towards wettability, 0D particles such as nanoparticles, colloidal particles can adhere to the different surfaces and provide a sole stabilizing interface towards coalescence, and miscibility[181]. The stability of these surfaces is influenced by the interfacial wetting characteristics of these particles which are greatly regulated by their contact angle. When the contacting liquid is water, water-in-air materials can result in fabrication of liquid marbles using hydrophobic particles which have low surface free energies resulting in reduced wetting by surrounding liquids. With the involvement of surface roughness, these 0D particles can attach onto the surface of high viscous liquids to form a highly stable Cassie wetting state[182], which are widely applied in oil bubbles and dry oils. For explorations in oil-repellent surfaces, pitcher plants of the genus Nepenthes serve as a best example. The surface topography and superhydrophilic mimicking gel-like surface generates enough frictional force along with superior wettability even under the absence of water lubricated layer as seen in marine species. In the above case, hydrogels which are cross-linked polymers via chemical or physical treatment serve as an ideal medium for impregnated surfaces due to its tunable and reconfigurable liquid-sorption properties. Moreover, by selectively attaching multiple 0D nanoparticles over each other, a 3D porous structured substrate can be obtained. These surfaces can

be further impregnated to form liquid-infused surfaces which can be exploited towards water/oil separation.

2.4.2.2 1D surfaces

1D structures play a wider role in construction of nanostructured surfaces, gels, sponges, etc with inspiration from duck feathers[162], etc. Owing to their surface curvature, these structures have effectively higher surface roughness factor allowing them to be switchable between superhydrophobicity and superhydrophilicity properties. In the case of droplets, wetting a 1D surface leads to more dynamicity when surface gradient is introduced. And, the differences between Laplace pressure on either side of the droplets, a successful cargo transport can be achieved to be either directional or in a controlled manner. Such For example, a team led by Zheng's group designed and developed an artificial spider silk and found cargo transport behaviour due to the surface's higher surface energy[183]. Due to the factors such as alignment direction, position and topographical features, the rationale behind fabricating such structures are easy. Not only in cargo transport, but also these 1D structures made of asymmetric shape design and surface modifiication can be a representative of various physiological principles such as "Ion Channels" which can respond to changes in the wettability to ensure selective transport of cargo[184]. Moreover, 1D structural features on top of the surface can also be externally actuated to allow shape configuration between column to cone towards precise liquid transportation.

2.4.2.3 2D surfaces

Pivotally, most of the structural facets being created on micro/nano-structured surfaces are made of particles which exist as sphere, rods, cones. One such example is the chaotically ordered nanostructures on lotus leaves, mosquito eyes or even in fern leaves. Such 0D structures forms the base for fabricating 2D structural features on any surfaces. The fabrication methodology towards creating an ordered structural feature results in anisotropic characteristics, wherein, a randomly ordered structures result in isotropic characteristics[185]. By selectively designing the structure distribution, several device modalities can be achieved which will be discussed further in the sections. One such example of ordered 2D structure is their ability to trapping of water/oil/gas towards separation applications. A recent study has shown that by selectively fabricating a 2D structure via 3D printing and impregnating the surface with a switchable soft composite resulted in efficient interaction between water and oil[186]. This gel impregnated structure provides superior repellent properties which can be achieved for both water and oil. Moreover, by selectively dissolving a surface, a porous structure can be created with complex multifunctionalities, such as anti-icing, anti-biofouling, etc.

2.4.2.4 3D surfaces

By selectively layering/printing/etching the surface, multidimensional 3D/4D surfaces can be created. It requires a careful combination of the correct scaffold chemistry to adhere itself with one another via ion-binding sites that promote heterogenous nucleation. A hydrogel is a 3 dimensional porous structure that is created by interaction between polymeric chains with water[25]. Owing to

the stronger interaction between liquid molecules and crosslinked polymers, the liquid molecules are firmly trapped within the surface. Upon immersing in water, these crosslinked polymer structures swells in a differential manner to transform from 2D film into a multimodular 3d structure[187]. For example, 3D kirigami structures developed by compressive buckling at various length scales using a wide material choices such as polymer, metals, etc can give rise to enhanced level of structural complexity such as tent[188], etc. It is always believed that when the thickness of the surface is considerably large, the materials can deform into multi-dimensional configurations via a complex, hierarchical route.

2.4.3 Nature inspired interfacial systems

In addition to the widened attempts to fabricate surfaces of various morphologies, recent research has been warranted itself into chemistry, especially for the material systems used at the interface[189]. Due to its intrinsic low-adhesion properties and/or the solid/liquid/gas three-phase contact model[190], chemical behaviour remains solemnly varied on superwettable surfaces when compared to traditional solid/liquid two-phase interfaces. We will focus mainly on the recent developments of interfacial systems for building liquids of varied degrees of surface tension and the behavioural change attributed to the chemical reactants and products.

2.4.3.1 Interfacial materials towards superhydrophobicity/ superoleophobicity

The concept of super repellent materials was studied with spherical liquid droplets which can suspend itself on a soot surface where a rough galena surfaces covered by stearic acids exhibited a superior water contact angle of (CA) of 160°[191]. However, the mechanism/governing principle behind such materials remained unexplored. In addition to low-adhesive super repellent interfaces found in nature, some organisms also provide high-adhesion superhydrophobic properties, such as gecko feet[160]. It is well known that the surface of the gecko feet is constructed with well-aligned micro-hairs called setae, which are divided into several hundred of smaller ends called spatulae. Liu et al. reported that the adhesive interaction between gecko feet and water droplets was found to be in the range of 10 μN to 60 μN, and varied according to surface interface conditions of the setae proteins upon exposure to water[192]. Hence, to provide a superior dynamic droplet behaviour, it is of imperative importance to design the materials interfaces by tuning the chemical compositions to exhibit hydrophobic/hydrophilic properties. For example, plant cuticles are deeply covered with epicuticular wax which consists of straight-chain aliphatic hydrocarbons with different substituted functional groups at the interface[193]. Such a chemically tuned interface could effectively lower surface wetting and protects water permeation. Moreover, surface structure also plays a key factor along with the chemical composition for surface wetting behaviour on the interfaces. Therefore, a thumb rule to fabricate super repellent materials is the introduction of enough surface roughness and tailoring the chemical compositions to be hydrophobic.

Upon studying the superoleophobic materials and inspiration from nature, an underwater pillar arrayed silicon substrate was fabricated with increased roughness to result in contact angle of 174.8 ± 2.3° for oil droplet when immersed in water.[194] However, achieving a robust superoleophobic substrate is highly complex considering the sophistication of the hydrodynamic factors in underwater environments. One such study was carried out by Jiang et al who fabricated a hierarchical macromolecule-nano clay embedded hydrogels which can withstand increased stress to strain ratio of 2.5 MPa at 75 % strain and still exhibit superoleophobicity[195]. As discussed before, the third phase, i.e., the oil droplets, competes with the water to approach the surfaces and controlling the chemical compositions of the surfaces determines the intermolecular forces between the solid and water and those between the solid and oils.

2.4.3.2 Interfacial materials towards superhydrophilicity/ superoleophilicity

Several naturally inspired surfaces have enlightened researchers towards fabricating superhydrophilic structures. One of the favourites is the nepenthes pitcher leaves with micro-textured peristomes or rims revealing a thin layer of sticky liquid infused onto the surface making it super-slippery. Some aquatic animals, such as sharks[196], too exhibit similar characteristics to reduce drag force while moving under water. In technical terms, both these creatures exhibit two distinctive surface patterns such as thin hydrogel-like layers and hierarchical surfaces. A special case for superhydrophilicity is intrinsic superhydrophilicity. Several reports have been established on fabricating intrinsic superwetting phenomenon in silicon without any microstructures and simple liquid infused wrinkled substrate exhibiting the other extreme characteristics[197]. The design of

such surface roughness imparted structure can trap or repel considerable volume of air pockets inside gaps in the microstructure, and creating either superhydrophilic or superoelophilic materials. As known, most widely used oils are immiscible in water which is attributed to the air gaps present in rough surfaces pockets containing oil rather than air. Study by Ujjain et al generated a solvent evaporation-determined rough surfaces embodied with mixture of nanoparticles and polymers wherein surface exhibited water repellency of 176.5 ± 3.3^{0} when immersed in silicone oil exhibiting under-oil water repellent behaviour[198]. The authors have also found that the smooth sample exhibited superhydrophobicity and aerophobicity, whereas the other three types of samples exhibited unexpected superhydrophobicity and superaerophobicity as the intermolecular forces between the solid atoms/molecules and the oil molecules were considerably stronger than those between the solid and water or air. In general, the liquids can be presented as a single-element family like ionic liquids, metallic liquids, liquid crystals or as a multi—module liquid system such as colloids, oil in water, etc. By carefully, structuring the surface chemical compositions with novel design parameters, the overall performance of the liquid-repelling/attracting materials can be facilitated.

2.4.3.3 Interfacial materials towards superaerophobic/ superaerophilic

Inspired by the marine organisms which exists without the presence of gills, are creatures that employs alternative breathing model via physical external lung consisting of air bubbles. However, a different mechanism is withheld by lotus leaves via tailoring of nanopillars on its surface to provide gaps for liquid droplets to gas molecules to travel between interfaces[199]. Based on that, a study

reported an underwater nano wired-haired mesh that can selectively control gas bubbles under water and efficiently transported[200]. The golden rule is that when a solid surface is submerged in an aqueous habitat, water molecules compete against gas bubbles to approach the surface first at the interface. Depending on the chemical compositions of the surfaces, the intermolecular forces between the solid and water and those between the solid and gas determine the wetting state on the substrate. In a common language, the chemical composition on the rough surfaces dictates the wetting state under diverse ambient conditions. For example, superhydrophilic materials in air would be superaerophobic under water, whereas superhydrophobic materials in air would be superaerophilic under water.

2.4.4 Summary

In nature, a solid surface is a stage that provides continuous supply of energy and electrons with tendency towards mass transport under different conditions. Especially, naturally existing surfaces provide a huge impact on designing structures artificially to control and promote various real-life applications which are seemingly endless. This trend of strategically innovating structural matrices requires contradictory conditions such as high specificity and sensitivity for droplet capture and dynamics with special requirement towards repulsion. These surfaces could be fabricated via multifaceted methods and requires new fabrication methods to provide highly reliant material properties with cost towards manufacturing. Applications such as droplet transport on super repulsive nano/micro-structured surfaces, liquid infused surface to provide friction-free movement in endoscopic examinations, invisible gas-vapor layer present under extreme surface conditions need additional optimization in terms of practicality. The nature inspired surfaces can either pronounce or inhibit the

natural three phase contact regime (air, water and solid) for broader applications in energy harvesting, droplet transport, thermal transport, soft robotics, etc. By introducing different nano/micro-architectures on the surface, an optimized mass-energy kinetics can be realized. The manipulation of such surfaces with their intrinsic naturally existing surface phenomenon can lead to core opportunity and solve unmet needs to improve quality of life. Extending the concept of fabricating such naturally available surfaces is also crucial in the future which motivates the development of advanced applications through innovation.

2.5 Strategy towards fabricating superwettable based devices

As discussed in previous sections, a third phase of matter exists at the interface of gas or liquid and the surfaces of superwettable materials. However, the fabrication of such surfaces may project an unexpected characteristic towards traditional two-phase surfaces and promotes as a simple strategy for the alignment/assembly of nanoscale building blocks for superwettable materials. Two major nature-mimetic interfaces are widely considered for extreme device fabrication: solid/liquid interface which have an important role in controlling the wetting state and hierarchical structure formation at the interface, solid/gas interface for enhancing the thermal heat transfer between the interacting objects. The overall design functionality of the surface interface is based on the wetting state of the liquid present at the interface. Prevailing evidence on the liquid transport is provided by altering the surface topography or surface physics to yield higher or lower surface tension for potential applications. We will also shed light on certain the mutual benefits of superwettable materials and the field of chemistry. Due to the low adhesion nature, the interconnected surface gaps are

filled with air and thereby, the surface gaps can continuously transport gaseous reactants into the liquid channels. On the contrary, the superhydrophilic surfaces can also be generated as a super-slippery interfaces due to fully wetted oil layers in the gaps. An ultra-thin layer originates from the product of two reactant liquid films which can behave as a superhydrophilic surface[201]. By, exploiting the above strategy, various surfaces and interfaces are achieved for numerous device fabrications as discussed in the later sections.

2.5.1 Superwettable interfaces based on chemical reactions

Ideally, on a superwettable surface, the liquid droplets which are released during a chemical reaction gets repelled from the surface due to the intrinsic interfacial chemistry thereby improving the overall output of the products. The anti-wetting behaviour of the surface is dictated by the interfacial chemistry and surface microstructures. Zhao et al. reported an alternative way to use hydrophobic powders to build liquid marble based microreactors[202]. Importantly, varying the amount of reaction liquid inside the marble reactors was made more easier due to the low adhesion between the hydrophobic powders and the water forming a superhydrophobic interface. Recently, a novel "super-slippery" surface has attracted much interest. Li et al. reported a super slippery surface made of hydrogel infused 3D architecture that can switch its behaviour between oil and water[203]. The hydrogel pockets played a key role in repelling water permeation, and the rough porosity optimized the anti-liquid property which can be exploited in various promising applications such as blood transport,[204] etc. In general, the static contact angle of water droplets is decreased on the above materials owing to the larger surface tension and a

stimuli-responsive super-slippery structures can be fabricated which can conform itself to the environmental conditions.

2.5.2 Switchable wetting behaviour under interfacial conditions

Stimuli responsive materials can attribute to the co-existence of superhydrophilicity and superhydrophobicity in air by varying the overall molecular configuration by external stimuli, and the resultant surface wettability would change correspondingly. The change of environmental pH value dictates the overall stereo-configurations of functional molecules by rendering them to be hydrophilic or hydrophobic. Studies have proved that the wettability-switched surfaces exhibited different behavioural characteristics swapping between superhydrophilicity and superhydrophobicity[206]. By chemically modifying the DNA molecules with fluoride-containing hydrophobic group and subsequent coating onto a gold surface with the assistance of gold–thoil bonds, yielding a pH-mediated switching interfaces. A carbon fiber immersed in polymethylmethacrylate-b-poly-n-isopropylacrylamide (PMMA-b-PNIPAAm) solution yielding various beads-shaped PNIPAAm fibers below 25 °C, with tiny water droplets being condensed on the surfaces of the fiber. Whereas, for the fiber at 40 °C the coalesced droplets underwent a directional movement due to the wettability interface gradient on the spindle-knots which can be exploited for reversible switching mechanism between under-oil superhydrophobicity/ superhydrophilicity[207-209].

2.5.3 Superwettable interfaces based on fabrication

Interfaces featuring superwettability, such as superlyophilic, superlyophobic, superhydrophobic, superoloephobic, etc exhibit discernible

differences in the transport dynamics of liquid and gas compared to conventional interfaces. Ideally, many fabrication processes such as anodization, wetting mediated patterning, and lithography are usually carried out to fabricate surfaces with air/liquid, solid/liquid, solid/gas interfaces. The above fabrication techniques provide a multifaceted approach for manipulating both spatial and weting/dewetting characteristics.

2.5.3.1 Anodization

Aluminium, along with copper, have been considerably exploited for its innate protective oxide layer. The oxide layer of aluminium called as alumina (Al_2O_3) is adhered to the metal surface[210]. And the overall oxide layer thickness, compactness and chemical composition is dependent on the metal's purity. The formation of aluminium oxide is commonly achieved via anodization under an aggressive environment of different pH conditions(**Fig. 2.12)**. The porous AAOs are prepared by conventional anodizing setup wherein, the outer anodic oxide is slightly miscible to the electrolytes such as sulfuric acid, phosphoric acid, etc[212]. In general, the overall anodizing of aluminium happens as follows:

$$2Al + 3H_2O + 2Al^{3+} \rightarrow 2Al_2O_3 + 3H_2 \quad (13)$$

$$2Al + 3O^{2-} \rightarrow Al_2O_3 + 6e^- \quad \text{(metal oxide interface)} \quad (14)$$

$$2Al^{3+} + 3H_2O \rightarrow Al_2O_3 + 6H^+ \quad \text{(oxide-electrolyte interface)} \quad (15)$$

With wide range of anodization methodologies been optimized and tailored to achieve functional characteristics, some of them including i) Chromic acid anodising, which is known as Type 1 anodization process and commonly

extracted towards aerospace engineering for creating anodic layer from 0.5 μm to 18 μm thickness in 2xxx and 7xxx alloys[213]. The advantages of the resultant products are normally opaque, soft, and ductile nature, however, they are not highly durable and resistant towards dyes, ii) Sulphuric acid anodising, a widely exploited technique to impart superior wear and corrosion protection in Type 2 and Type 3 anodization materials which produces film thickness between 1.8 μm to 25 μm for Type 2, whereas higher thickness in the range of 13 to 150 μm is achieved for Type 3.[214] iii) Organic acid anodising, known for their integral colour anodising process and are highly sensitive to alkaline materials. The anodic layer thicknesses range from 20 μm up to 50 μm[215], iv) Barrier type anodising, commonly performed in borate or tartrate environmental baths in which aluminium oxide remains insoluble. A major structural feature is that the anodic layers are free of pores compared to the sulphuric and chromic acid processes yielding an anodic layer thicknesses in the range of 0.5 μm[216]. Finally, Plasma Electrolytic Oxidation also known as micro-arc oxidation, uses a combination of electrochemical anodization with plasma process in metals like Al[217], Mg[218], Ti[219], etc. They assist in achieving decent resistance towards wear and chemical, however, several reports have suggested that the anodic surface remains extremely rough when compared to its neighbour processes.

In general, the surfaces/interface morphology and structural characteristics of the anodic layer is affected by a number of parameters such as anodising potential, anodising time, current density, type of electrolyte, and temperature of the electrolyte[220]. Increase in the anodising temperature increases the growth rate, pore diameter, cell wall thickness, and pore density of the anodic oxide film. To carry out anodization process, electrolytes are in addition to temperature and voltage to achieve homogeneous arrangement of the

pores[221]. Chu et al[222], delivered a study wherein sulfuric acid can be a potent electrolyte for anodic oxidation process when a mild temperature of 0 to 15°C is applied. Experimental studies have showed that the usage of voltage above its self-ordering voltage could result in no film growth. In a simple relationship, voltages and the corresponding geometrical features of the anode layer is correlated by

$$D_{ipore} = K.V \tag{16}$$

wherein, D_{ipore} is the distance between adjacent pores, K as the proportionality constant, and V the anodizing potential. Study by Murphy[223] has reported the influence of electric field on the porous surface formation. It was noted that the anodization time of the barrier thickness formation is highly dependent on the electric potential being applied which is also proved by Thompson et al[224]. Typical approaches consist of controlled oxidation on alloys and Plasma Electrolytic Oxidation (PEO). Yao et al. prepared a black high-solar-absorptivity and high-emittance coating on Titanium alloy by doping Fe, Co and Ni atoms to obtain as of 0.93 and ε of 0.88[225]. Shang et al. used micro-arc oxidation to prepare a multi-layered GO coated Magnesium alloy which showed an improved corrosion resistance[226]. While the coating technology on the surface of Titanium and Magnesium alloys advances, their corrosion resistance declines upon exposing to solar light irradiation. When a prescribed electric potential is not applied, the cations Al^{3+} gets concentrated at the metal-barrier film resulting in a truncated growth on the surface[224]. The equilibrium temperature of any subsystem of the spacecraft is controlled by the solar absorptance (α_s) and infrared emittance (ε) of its surface[227,228]. Studies have also showed that varying the temperature of the anodization could highly favour solar

absorptance and thermal emittance. Moreover, by varying the temperature the oxidation process could accelerate the dissolution of anodizing coating (i.e. coating layer),

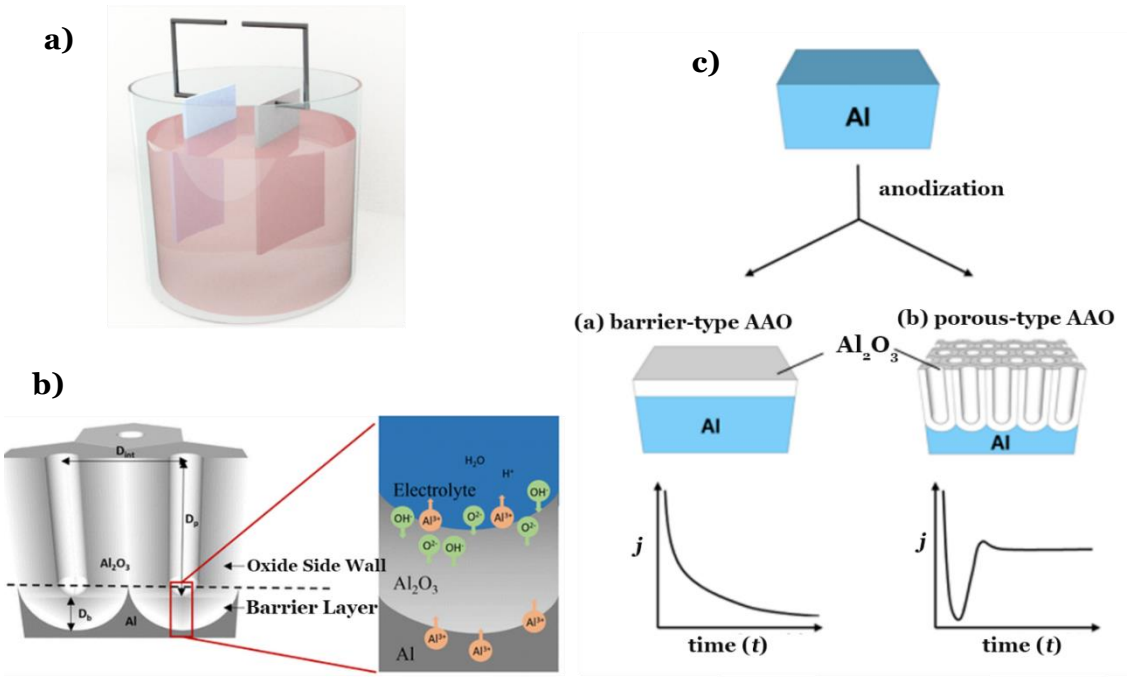

Figure 2.12 a) Anodization reaction chamber with **b)** underlying electrochemistry[160] **c)** Effect of varying voltage and current density on the porous structure formation of aluminium[143].

2.5.3.2 3D printing

Additive manufacturing, also knows as 3D printing is one of the potent advanced manufacturing tool to provide rapid production of 3D structures involving complex patterns. Specifically their complex geometries involving precision, design flexibility and superior customization makes it one of the advanced manufacturing systems. Naturally inspired surfaces with complex topographical features such as in lotus leaf, gecko feet, can be mimicked to ultimate precision. Fundamental studies involving fabrication of artificial lotus

leaves to impart water repellent capability is achieved by 3D printing micropillar surfaces with a contact angle of 139°[229]. Dong and co-workers used 3D laser

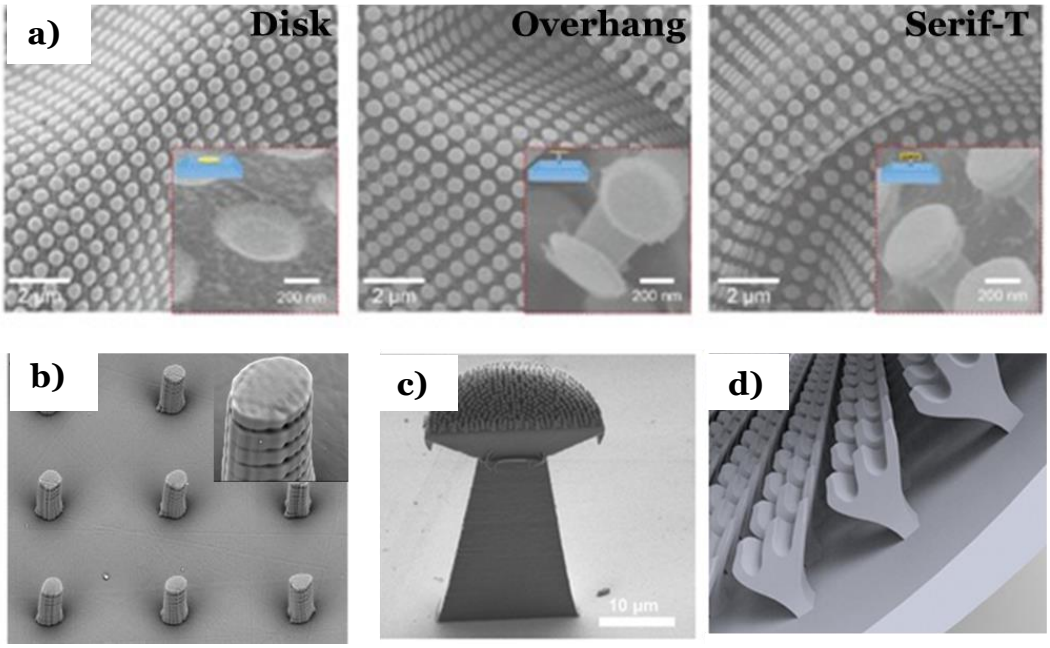

Figure 2.13 a) Spring tail inspired mushroom with multiple nanostructures[233], **b)** Printed superhydrophobic pillars[232], **c)** SEM view of the cross-sectional doubly re-entrant micropillar with a nanorough top [230], **d)** Multiscale 3D printed denditicle structures[231].

printing to fabricate a superoleophobic surface textures that allows for slippery textures to provide advanced liquid repellent properties[230]. In another study, a combined doubly re-entrant micro-topography was created on top of each other to create a double re-entrant micropillars for facilitating an infilled slippery lubricant[231]. Also, inspired by shark skin, several micro-riblet features printed successfully to achieve nearly 10% drag reduction for aerodynamic applications[232]. Re-entrant structures inspired from springtails with mushroom-like overhang structures was fabricated in combination with thermal oxidation[233].

2.5.3.3 Lithography

Briefly, soft lithography tool uses the amalgamation of capillary and hydrodynamic forces within the active components to create multiple patterns of choices. The technique uses supplementary factors such as temperature and time to achieve diverse sized and shaped patterns. Mondin et al. designed an unconventional approach using NIL technologybased on the patterning of PMMA, using the nanoimprint lithography (NIL) to pattern different surface architectures by varying the moulding duration between 10 and 100 seconds[234]. Based on this, researchers got inspired by the microarchitecture present on the lotus leaf surface which has shown to exhibit an invisible lubricant to hold liquid droplets with surface friction. Another team led by Li et al, exploited the photopatterning technique to create micropillared surface with a thin layer of polytetrafluoroethylene (PTFE) nanoparticles on top of it to impart the required superhydrophobicity. This technique uses parallel growth of micropillared architectures with precise control over pillar diameter and inter-spacing[235]. An artificial anisotropic oil repellent oriented hood-like microstructure of the file fish was created on a PDMS surface which provided a contact angle of 143 ± 2.1° inside water[236]. A superamphiphobic surface structure based on ZnO was prepared by combining Ultraviolet radiation and nanoImprint lithography (UV NIL) to create surfaces with further increased contact angle of 155° and extremely low contact angle hysteresis (CAH) [237]. It is believed that the combination of more than one technique can be used to generate architectures on a larger scale surfaces of polymers, rigid metals like Si wafers, elastomers, etc.

2.6 Functional surface/interface enabled engineering applications

Nature inspired functional surfaces can be harnessed in multifaceted roles, including self-cleaning, anti-icing, anti-fogging, anticorrosion, energy harvesting, power generation, sensors and water–oil separation[238-244]. We limit our discussion to extreme applications such as liquid-liquid separation, energy converting devices, anti-icing, soft robotics by manipulating the surface/interfacial energy, mass, and heat transfer via nature's inspiration using above theories.

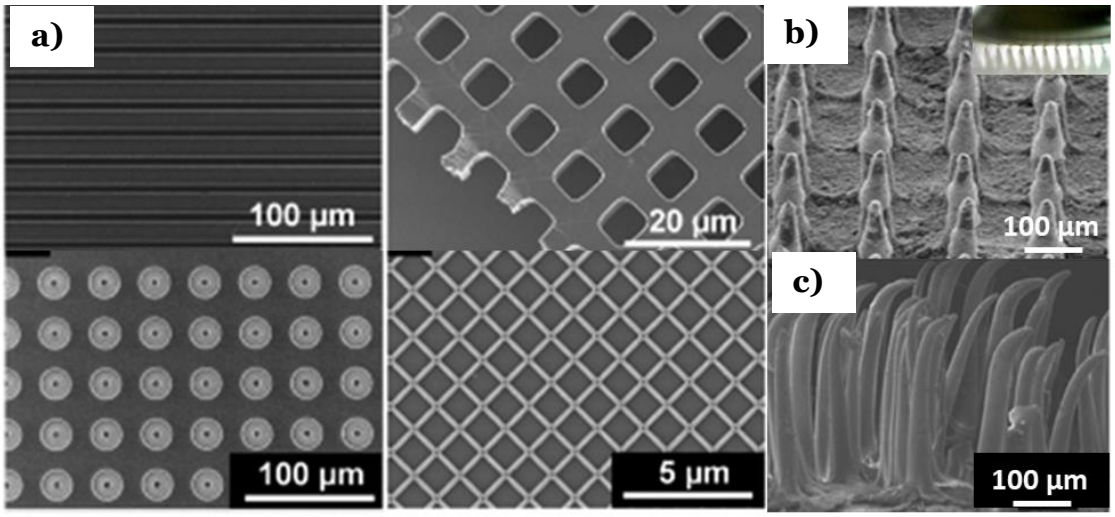

Figure 2.14 a) Nanoimprint assisted lithography fabricated architectures on PMMA surface[235], **b)** Micropillared surface with a thin layer of polytetrafluoroethylene(PTFE) nanoparticles towards superhydrophobicity[235], and **c)** Oil repellent artificial microstructure of file fish[236].

2.6.1 Liquid-Oil Separation devices

We focus on the advantages of extreme wetting states achieved on different surface/interfaces for oil-water separation which are in high-demand in industrial water and oil spills, off-shore engineering[245]. Recently, surface

interfacial materials with integrated switchable superhydro/superoleophobicity have proven to be highly efficient for this purpose. Surfaces which have novel morphing structures combined with superhydrophobicity and superoleophilicity can effectively aid in separation of oil from oil–water mixtures(**Fig 2.15**). Inspired from nature, Jiang's group observed the self-cleaning phenomenon achieved via a multi-scale hierarchical structure on fish skin to enable an on-demand water oleophobic property and surface-wetting controllability. Such features boost the fish's locomotion faster in an oil environment[247]. A liquid infused porous surfaces were created to trap water molecules alone in a mixed liquid environment whose surface behaviour is commonly seen in pitcher plants.

The textile fabrics also forms an inexpensive, soft candidates for separating oily wastewater[231]. By pristinely modifying the surfaces with superhydrophobic components, studies have shown improved superoleophobicity. Depending on how the surface/ interfacial textures are fabricated, the water/oil droplet can dramatically change its adhesion behaviour. Hence artificial surfaces with defined surface chemical modifications can be made into oil separating materials owing to its improved surface roughness property. A major drawback with such structures is their susceptibility towards oil fouling. Organic liquid/oil separation has been a challenge to most of the researchers due to the surface prerequisites and reduced reconfigurability towards different liquid medium. In principle, the surface property must be programmed in such a way that the surface tensions can boost the efficient liquid separations with high flux. Studies have been focussed on improving the surface structural morphology and switch ability towards varied surface tension. One such example is the use of surface wrinkles for efficient phase-separation

formation mechanism. Wrinkled surfaces have been a wider interest to researchers due to its shape transformability and functionability[250]. However, a major drawback in such patterned surfaces is their susceptibility to unwanted liquid flooding at the nucleation sites. One striking feature inspired from nature is the presence of supporting aircushion to minimize liquid-solid interactions. Hence, infusing the surfaces with a gel-like substance which promotes complete reconfigurability, switchability to external stimuli and oil fouling has been

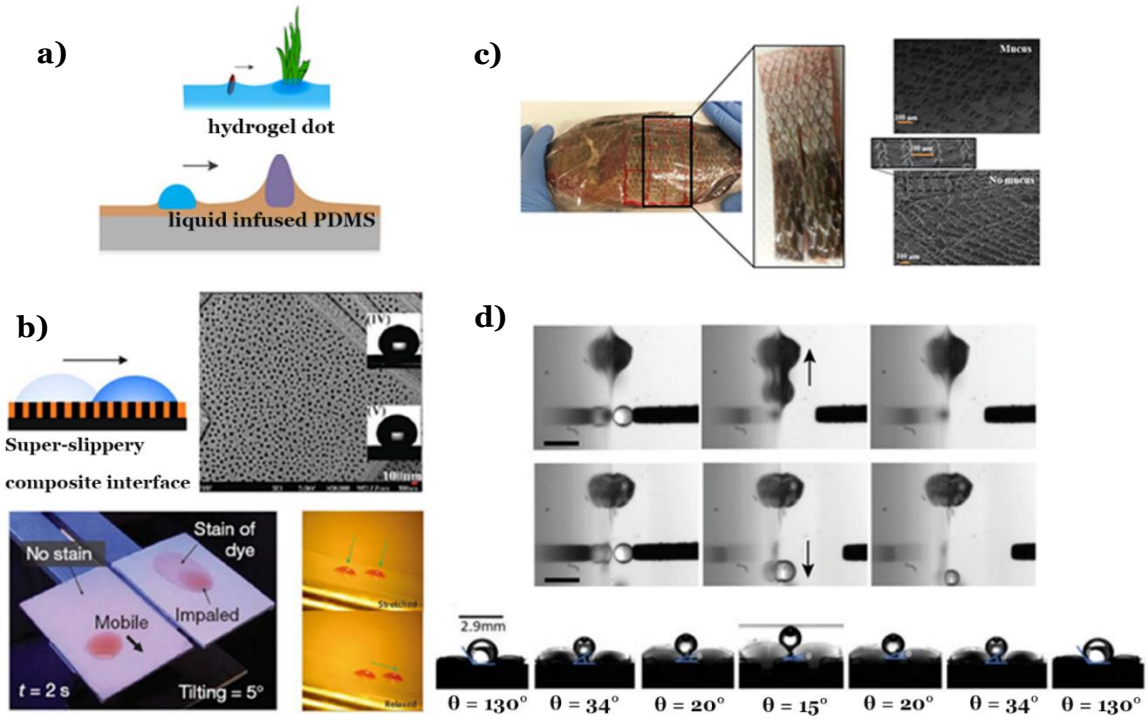

Figure 2.15 a) Directional pumping of droplets by capillary force on slippery surface with immobilized meniscus inspired by vegetation capturing floating seeds[246]. **b)** Adaptive surfaces made of a liquid film supported by a nanoporous elastic substrate to manipulate low-surface tension droplets[247]. **c)** Superoleophobicity of surfaces inspired by fish skin[248], **d)** Gel impregnated stimuli responsive wrinkled surface[251].

welcoming[19]. With the assistance of hydrogel infused textured layers, programmable surfaces have been shown to successfully separate wider immiscible organic liquids.

2.6.2 Energy generation devices

Energy generation is the operation of garnering abundantly available primary energy into useful forms with the aid of novel surface/interfaces[252-254]. In general, scavenging the abundantly unused global energy can lead to propitious inhibition to energy crisis and provide thrust for labor-saving potency for extremely smart devices. Various nature inspired surfaces have been exploited and tested for their role in converting environmentally abundant waste energy into useful power output by taking advantage of the hidden surface physics(**Fig. 2.16**). A solid/liquid interface based triboelectric nanogenerators have received considerable delight in the blue-wave technology which converts mechanical wave energy into powering devices via contact triboelectrification and electrostatic induction on the surface/interfaces. Despite of diverse modifications and advancements, what the device fails to deliver its reconfigurability and tunability originating from the intrinsic materials properties and environmental conditions. A fundamental theory of how the surfaces on a nature scale works provides immense knowledge and inspiration towards solving the unsolvable. Another extreme example of energy generating device is a study led by Mayer et al whose group worked on bionic inspired stretchable nanogenerators for soft power energy generation. The study was inspired from a marine creature, *Electrophorus electricus*, whose surface is made of ionic gradient compartments with biological constraints to feature power characteristics. The group devised an artificial functionally patterned surface made of soft hydrogel blocks bounded by repeated sequence of cationic and anionic pockets which generates immense open circuit voltage of 600V when the electrocytes convert the stored energy within opposing ion gradients of two different cations[253]. And by effectively exploiting the natural phenomenon such as dynamic falling of rain water, a study

has fabricated a simple design interface which exploits the impact energy of the droplets on a liquid-liquid triboelectric membrane to convert waste kinetic energy into useful electrical output[254,255]. Another abundant source of energy available on earth is the thermal energy which is found in many geo-thermal sources and found predominantly as waste-heat. With the assistance of surface physics and phenomenon occurring on a heated surface (Leidenfrost effect), the harvesting of thermal energy using phase change mechanism has led to novel class of friction-free nature inspired design methodology. The study exploits the temperature difference present on the heated surface to be translated into electrical energy by levitating dry-ice loads coupled with magnetic coil system. By manipulating the surface morphology of nature inspired yarn artificial polyurethane microfibers, abundantly available waste heat can be harvested and converted successfully into electrical energy via torsional mechanical energy[256]. To further improve the overall thermal scavenging efficiency on a low grade heat environment, a novel autonomous multigait soft energy system was designed to exhibit thermo-mechano-electrical transduction behaviour which could inspire for more scaled-down soft energy harvester to power electronics on a low scale[257].

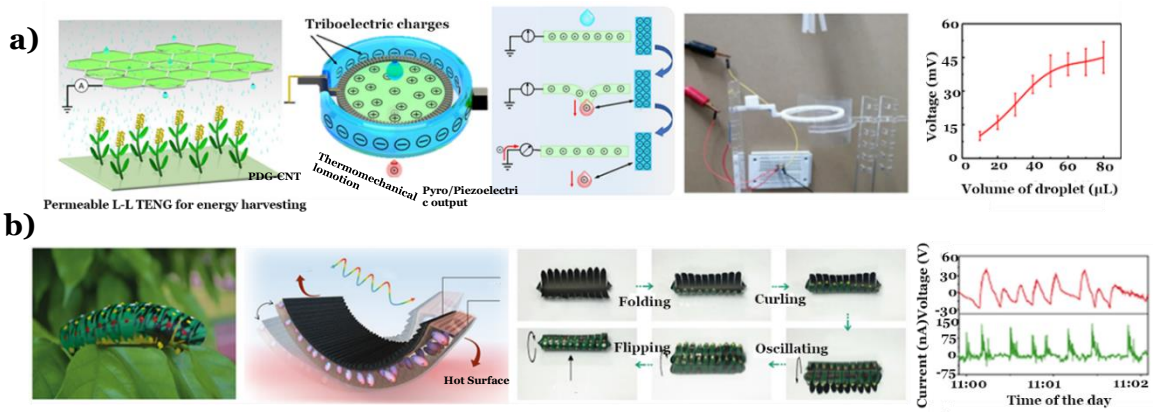

Figure 2.16 a) Triboelectric nanogenerator inspired surface interface for power generation by capturing rain drops [256]. **b)** Thermomechanical locomotion of elastic system powered by waste heat [257].

2.6.3 Anti-icing

A well-known theory states that the ice amassing can alter the aerodynamic character and cause loss of control (**Fig 2.17**). Most importantly aquatic animals such as pout fish skin surface possess special proteins that has shown extreme anti-icing/anti-wetting characteristics. Earlier studies by Aizenberg et al. developed a novel slippery liquid-infused porous surface (SLIPS) with inspiration from Nepenthes plant to impact anti-icing property(**Fig. 2.17 c**) [49, 258]. An inexpensive and low-surface energy possessing surface interface was created using a water-immiscible lubricating layer with Teflon and epoxy resin. Even at 60% humidity, the fabricated surface could eliminate the formations of ice and prevents penetration of frost/ice into the surface textures.

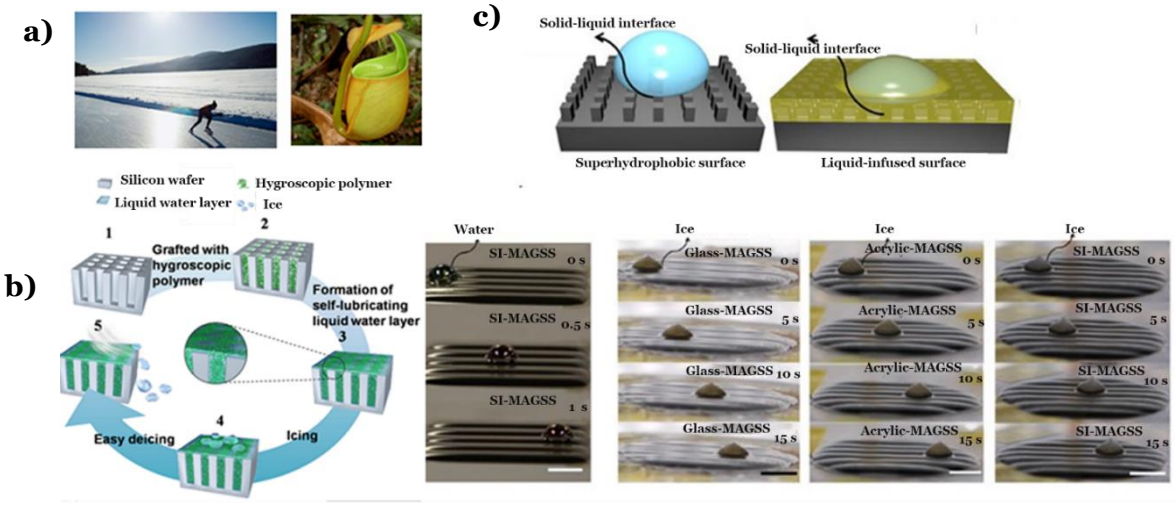

Figure 2.17 Nature inspired anti-icing surface physics and relevant applications in real world. **a)** Skiing in nature supported on liquid infused surface[240], **b)** Porous surface on an anodized aluminium layer exhibiting anti-icing properties by treating with self-lubricating polymer[2259], **c)** Nepenthes surface inspired liquid infused surface interface [260].

Another study showed an improved anti-icing feature when porous structures were treated with SLIPS at the surface rendering which are predominantly used

in manufacturing anodized aluminium oxide for extreme applications in aerospace industries[2591]. This feature has been of prime interest to outer-space voyage vehicles whose surfaces interact with extreme temperature variations. Upon treating the surface/interfaces with poly(acrylic acid) (PAA), a gel infused porous structure could be generated where the absorption efficiency of the system could be altered by tuning the smart gel with cross-linking density[260]. Hence, to suppress icing, it is required to inhibit the ice nucleation at the liquid-solid interface and texturing or tuning the surface/interface physics could be of widened applicability in areas such as cryopreservation of biological tissues, extreme spacecrafts, etc.

2.6.4 Soft Robotics

The amalgamation of recreating nature inspired surfaces which exhibits various surface dynamics are predominantly executed with soft robotics. Recently various soft micro/milli-robots have been lodged based on their behaviour towards various surface/ interfacial mechanism [261-264]. Among these, insects are primary candidates as they inherently adapt to the surface to achieve propelling force on their favoured terrestrial habitats. In general, this mechanism is deemed to be an energy conversion process as part of the surface energy is transformed into kinetic energy enabling them to move over variable surface ambience. Most of the soft robotics being designed achieves motion behaviour based on their stored elastic energy in the soft tissues and how they interact with the surface conditions. Making the most from the augmented functionalities rendered by

such surface interfaces, multiple locomotion and maneuvering convention have been demonstrated on soft robots(**Fig. 2.18a**) [264].

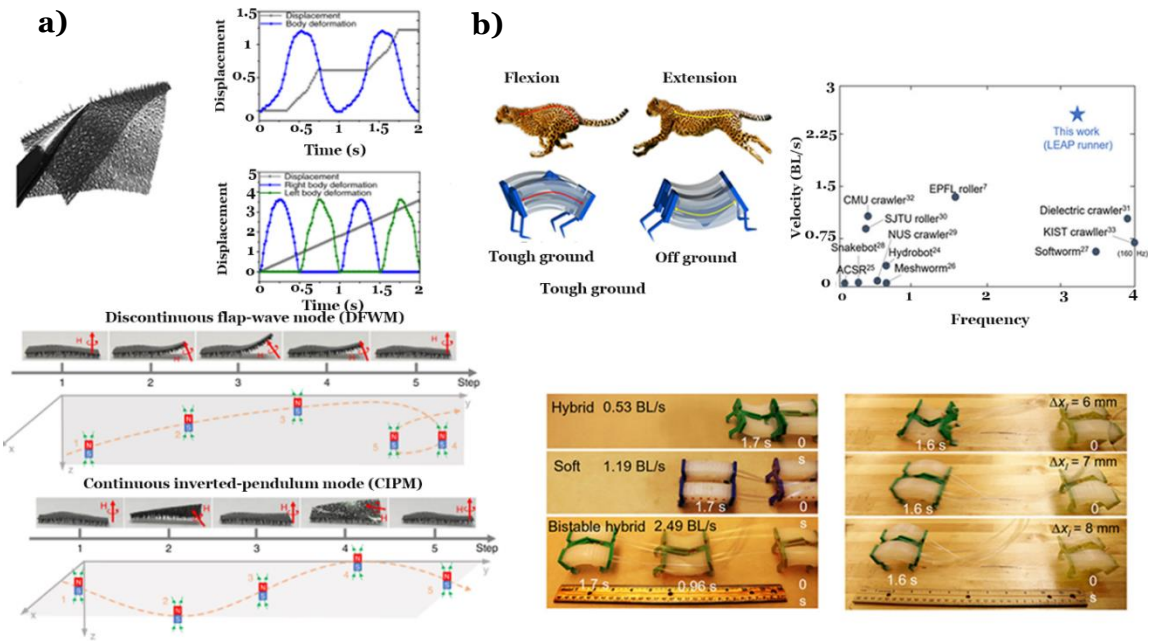

Figure 2.18. Nature inspired locomotion behaviour of soft systems on various surface topographies **a)** soft robot decorated with tapered feet, **b)** high performance soft machines based on elastic instabilities[264,265].

Recently, Tang et al. (**Fig. 2.18b**) reported an elastically reconfigurable soft robot inspired by cheetah with a multiple tapered soft feet architecture, which exhibited superior adaptivity to various harsh surface environments with an ultrafast locomotion speed and an excellent obstacle-crossing ability[265]. Inspired by the surface structure of the organisms, a soft robotic fish whose wrinkled surface assists in undulating locomotion through water. An osmotically actuated tendril-like soft robot was designed which works on the principle of immobilized ions on the surface and introduction of osmotic pressure difference[266]. Making the most from the augmented functionalities rendered by such surface interfaces, multiple locomotion and maneuvering convention have been demonstrated on soft robots(**Fig. 2.18a**) [264]. Effectively modifying the surface physics has been reported to assist soft robots to travel between different liquid and solid terrains,

under a constant external stimuli[267]. Of deeper interest, by modifying the surface geometry, soft robot manipulator could adapt its toing and frogging behaviour exhibiting advantageous over constant external stimuli. Development of mini-robots for biological applications have also shown the selective manoeuvring of the above without raising host body responses. Thus, it can be envisaged that by selectively choosing the surface/interfacial physics, highly reconfigurable and more conformable soft machines can be created for improving quality of life of mankind.

2.7 Summary

In general, we shed light on the exponential expansion of nature mimicry surfaces and interfacial regimes with respect to scientific community within numerous disciplines in science and engineering. The window towards controlling the overall wetting phenomenon at surfaces and interfaces have been a primordial driving factor for a menu of applications including self-cleaning, energy harvesting, anti-icing, etc. The inspiration from the surface effects of lotus leaves towards liquid behaviour has been a forte towards understanding how different nature abundant surfaces and interfaces gives rise to wide range of surface energetics as seen on slippery surfaces, porous structures. Bioinspired surfaces and interfaces provide a remarkable array of useful properties, such as gas-cushioned interfaces or functionalized surface structures that can restructure the system when contacts under extreme conditions. These properties originate from the ability of how the system interacts with the surface and interface Meanwhile, this literature survey highlights the great potential applications of mimicking the naturally existing surface interfaces and exploiting the theories

governing their characteristics for various practical applications. Meanwhile, the high cost for designing and fabricating such systems with stable property and large-scale size needs to be significantly lowered and, thereby improving the longevity and durability of both substrate and interfaces. To maintain/ escalate the innate property posed by the surface and interfaces under various stimuli should also be considered. The devising and usability of such surface and interfacial materials with several unexplored dynamic states will become an unprecedented research focus in exploring several applications under extreme environment. For example, the role of Leidenfrost condition which promotes large amount of waste heat found in industrial chimneys can be efficiently harvested and converter into useful energy. Research into extreme device fabrication in the case of harvesting waste heat from Leidenfrost effect also needs to be extended to cases in which the active material is not liquid(for example soft materials which can exhibit reconfigurabilty and provide continuous kinetic energy for longer time). Such systems are important in energy devices which can harvester not only at low temperature but also high temperature and convert them into useful energy. Tremendous windows are opening in the arena of exploiting nature inspired surfaces and interfaces for developments of novel concepts and ideas that could invent our understanding of exploiting such natural principles for improving quality of life.

2.8 Research Problem

Revealing the mechanism of extreme surface conditions existing in nature such as butterfly wings, lotus leaves, hot solid surface have an innate surface physics that enables enhancement on specific function, i.e. droplet repulsion[268], wettability [269]. These nature-inspired smart properties have arisen a growing

interest for their potential environment based applications, include wetting control[270], energy harvesting[271], micro-fluidic[272], aerospace engineering[273], thermal transport[274] etc. Up to date, extreme surface conditions are becoming more commonly used in industrial and commercial areas. By our definition, nature-inspired surface engineering is based on unravelling the fundamental mechanisms with design philosophy that adopts some of the systematic model to fulfil borrow the traits of natural model. Thus, nature-inspired designs may not even superficially or morphologically resemble their natural counterparts, but rather adapts to fulfil different contexts of technology. Examples of such extreme nature inspired surfaces can be found in many different areas of nature with varying purposes such as a hot kitchen hob which provides anti-water repellent capabilities at extremely high temperature or a wrinkled structure that has super lipophobicity properties. Recently, researchers have initiated attempts to exploit such surface conditions for advance engineering level by developing responsive structures under various external stimuli[49,256,260,268]. The studies will focus on developing extreme device applications that are capable to harness the fundamental surface physical or chemical transitions to facilitate controlled nanostructures twowards versatile surface features, smart liquid/oil separation, surface energy translations, wetting induced morphing transducers through exploiting naturally inspired surface and interfacial conditions.

Chapter 3

Experimental Methods

This methods chapter holistically summarizes the general methodologies exploited throughout the thesis, both in the fabrication process of the devices and characterisations of these device functioning such as high speed imaging setup, electronic circuit board, droplet shape analysis, etc. and related characterization approaches. A few standard sets of techniques were used throughout the entirety of the thesis, with some of the finer details been modified and tailored to specific applications as the project progresses.

3.1 Fabrication of Controlled Thermoanodized coatings

3.1.1 Fabrication of black CTC layer

Anodizing is a traditionally followed electrochemical approach which expands the thickness of the natural alumina formed over an Al alloy upon exposure to oxygen. A sample slice of AA2024 Aluminium alloy (40 mm × 40 mm × 2 mm), containing high silicon and magnesium was obtained from AA(Guangzhou) Aviation Materials Co Ltd. Prior to electrochemical reaction of the sample in an alkaline degreasing bath, the Al surface was mechanically polished with SiC and sand papers (from grit #1000 to #2500) to reduce surface roughness and remove the alumina layer naturally formed on the alloy. After a second rinsing step, it was etched in 1 mol/L NaOH for 12 min and washed by deionized (DI) water to remove contaminants. Here, the anodizing process, the

Al sample was served as an anode and were connected to a direct current (DC) power supply with temperature controller attached to the anodic end(**Figure 3.1**). The anodizing voltage, temperature and time was adjusted to the experiment. In first step, it was mechanically polished with SiC and at last, the samples were cleaned in a dilute sulfuric acid solution (1 mol/L) for 2~3 min and cleaned by DI water to remove unwanted impurities form the surface.

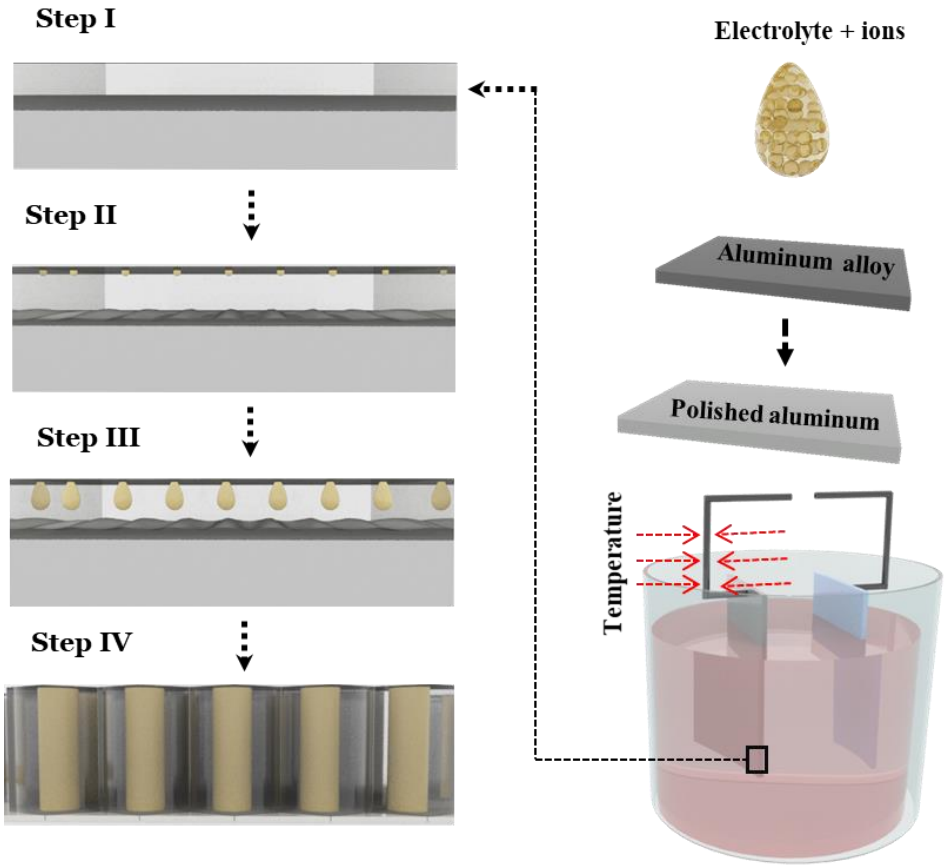

Figure 3.1 Working methodology of the thermo-anodization process

3.1.2 Surface Chemistry modification of CTC layer

To study the anti-icing features of the as-prepared CTC layer, a hydrophobic coating using KH-550 (silane) was applied to the surfaces to produce slippery surfaces as shown in **Fig. 3.2**. The silane coating can be formed on the surfaces with (i) a functional chemical group that can chemically bind to surfaces, (ii) self-organizable aliphatic chain, and (iii) functional group on the top for further surface modification. The purpose of making the surfaces hydrophobic/superhydrophobic is to ensure inhibition of water adhesion in order to preferentially prevent formation of ice crystals. This is because the hydrophobic effect is caused by non-polar molecules wherein, water being highly polar forms polar bonds with itself over non-polar molecules.

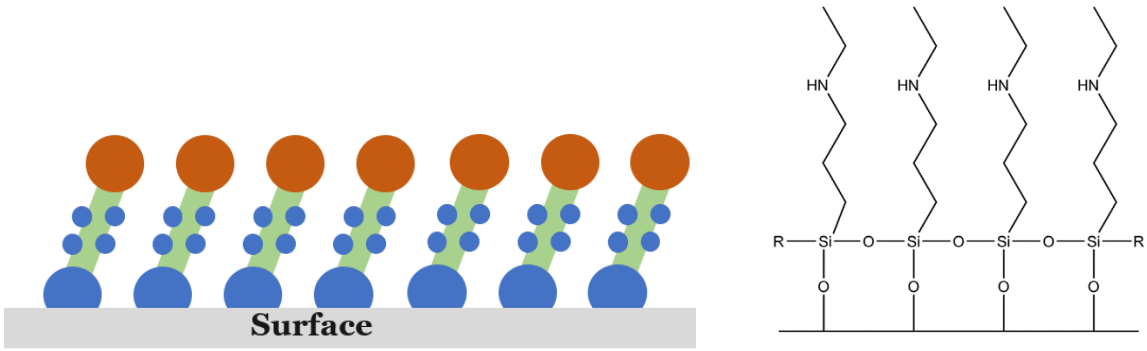

Figure 3.2 Schematic diagram and chemical formula of KH-550 coated on the substrate surface.

3.2 Fabrication of Switchable 3D printed hybrid-groove structures

The switchable 3D printed substrate is made up of an acrylate-based photopolymer, VerowhitePlus (VW) from Stratasys Inc. (Edina, MN, USA) which is printed using a multi-material 3D printer (Strasys® Objet 24) designed with SolidWorks® (Dassault Systems) as shown in **Table 3.1**. Once printed, the parts were immersed in acetone and isopropyl alcohol (IPA) and rinsed using de-ionized (DI) water after which the structure is dried using nitrogen gas. To fabricate the stimuli responsive gel, Poly (acrylamide-co-sodium acrylate) hydrogel was synthesized by mixing known quantities of acrylamide (monomer), sodium acrylate, N, N'- methylenebis(acrylamide) (crosslinker) and DI water. The mixture was then agitated and degassed for 10 mins, followed by adding 0.3 µL of N, N, N', N'-tetramethylethylenediamine and 1.0 µL of aqueous ammonium persulfate solution which aids in polymerization of the synthesized gel. For comparative studies, plain and smooth hydrogel films were also fabricated by pouring into a reaction cell composed of two parallel-separated glass slides with a 300-µm-thick Kapton film spacer to create the gap in-between. The gelatinization of gel solution was kept in the air for 30 mins. In brief, the hybrid groove-hydrogel surface structures were made of 3D printed substrates (30 mm x 10 mm in size) as shown in **Fig. 3.3**. The groove widths (W_{gel}) range from 0.5-1.0 mm, with a depth of h=0.5-0.8 mm, and distance/pitch between each groove (W_d) =0.5-2.5 mm. All the parameters are listed in **Table 3.1.** The hydrogel solution was injected into the grooves via precisely positioned syringes aided by Finnpipette F1, and the mould was then placed into the tube. The water was added from the edge, and the device was kept horizontally for 6 hours. Oxygen

plasma treatment was carried out for 30 sec to enhance the adhesion between hydrogel and substrate (**Fig 3.3a**).

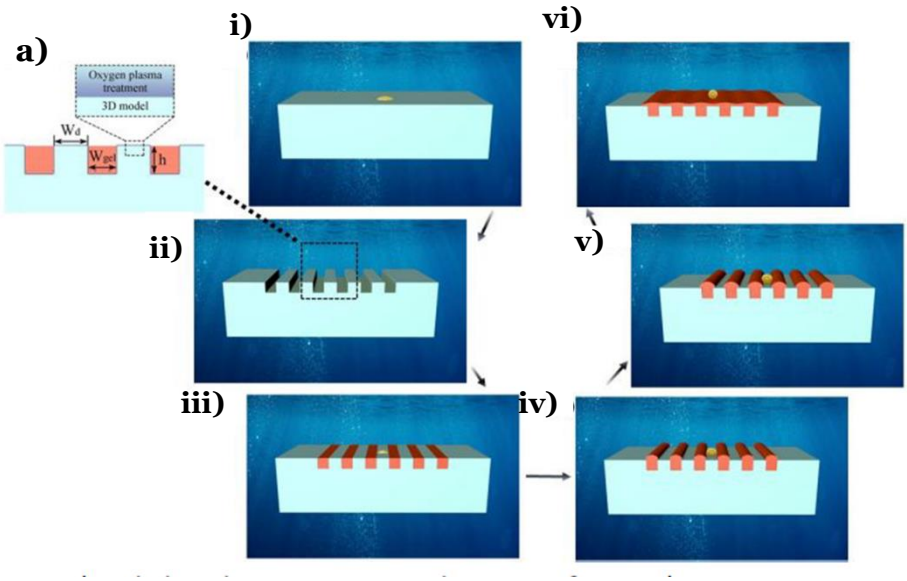

Figure 3.3 Switching of smart surface between oleophilic and superoleophilic.

W gel (mm)	*Wd (mm)*	*H(mm)*	*Contact Angle (°)*
0.5	0.5	0.5	110.99
0.8	0.5	0.5	107.88
1.0	0.5	0.5	110.55
1.0	1.5	0.8	96.7
1.0	2.0	0.8	95.2
1.0	2.5	0.8	83.32

Table 3.1. 3D model dimensions and contact angles

3.3 Fabrication and design of thermoelectric converter

3.3.1 Fabrication of Hydrogel Spheres

Different Elastic moduli spheres were prepared through polymerization of acrylamide(AAm)(Sigma Aldrich) with bis-acrylamide(BisAA)(Sigma Aldrich). The gel solution was agitated and degassed for 10 mins, followed by rapid addition of N, N, N', N'-tetramethylethylenediamine(TEMED) and aqueous ammonium persulfate(APS) solution to synthesize the gel. After 1 hour and swollen into the desired size using two different solvents by DI (de-ionized) water and PBS. The overall swelling nature of the spheres were calculated using the formula:

$$\%H_2O = \frac{(W_{wet} - W_{dry})}{W_{wet}} \quad (17)$$

where W_{wet} is the weight under equilibrium swelling in water and W_{dry} is the dry weight.

3.3.2 Electronic circuit design

To understand the conversion efficiency of the waste heat into electrical output, the tubes were connected to a customized 3D printed board to which the piezodiscs were attached that generates electrical signals upon mechanical deformation. A bridge rectifier was attached to the input source of the electrical input which aids in converting the AC into DC to power LED electronics. The rectifier was inturn connected to a capacitor (3.7μF) which is optional. The capacitor assists in storing the electrical energy for a longer period of time and discharges when reaches a threshold value. The overall circuit for the

thermoelectric energy harvester and internal circuit design is provided below in **Fig. 3.4a** & **Fig. 3.4b**.

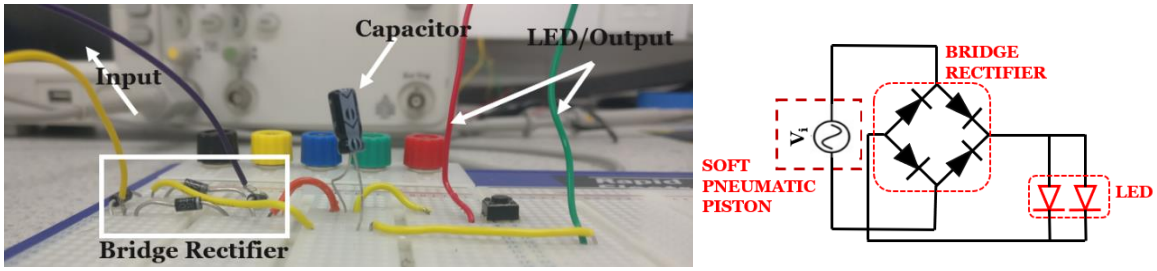

Figure 3.4 a) Electronic circuit connection of the thermoelectric converter. **b)** Circuit blueprint utilized in the conversion of AC into DC to power electronic components.

The output voltage generated from the piezo disc was measured by a mixed domain oscilloscope (Agilent technologies, impedance = 1 MΩ). The mounted piezo discs on the 3D printed holder is placed over the tube which confines the bouncing motion of the gel sphere. **Fig. 3.5** shows the overall design setup of the thermoelectric energy harvester which is connected like a lego and powers the electronic component.

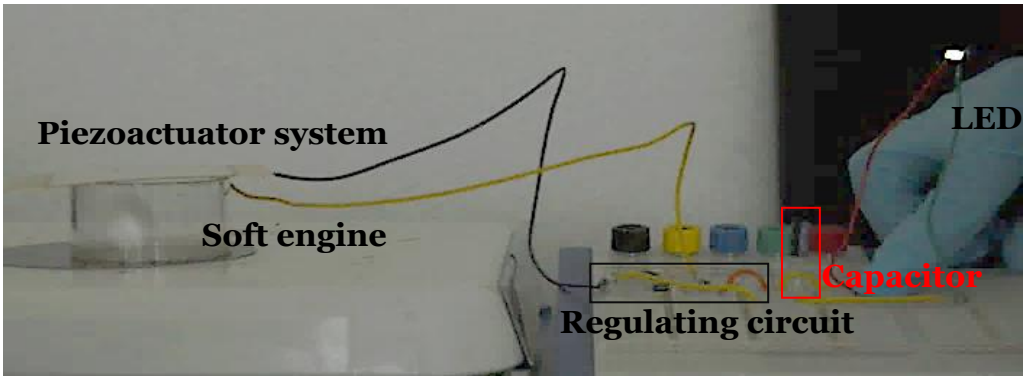

Figure 3.5. Real time demonstration setup of the energy harvester constituting of the soft engine, piezo component, regulating circuit and LED.

For powering multiple electronic light emitting diodes, a special printed circuit board was fabricated as shown in **Fig. 3.6**. The LEDs were soldered specifically onto this board to produce a NC pattern.

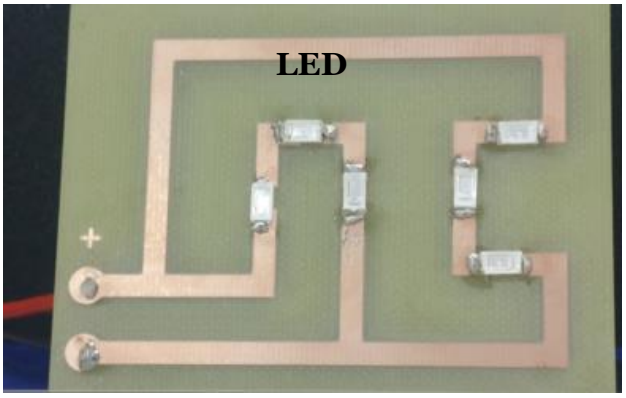

Figure 3.6 Printed circuit board depicting the NC logo.

3.4 Fabrication of 3D conformable soft transducer system

3.4.1 Surface treatment of TPP (Two-Parallel Plate) system

The TPP system consists of a hydrophobically treated poly(methyl methacrylate) (PMMA) acrylic top plate, and a bottom plate (35 × 80 mm rectangle chip cut from polished silicon wafers) with hydrophobic/hydrophilic wetting control patterns. The hydrophilic zone on the bottom plate was 1 μm thermally oxidized SiO_2 layer. And three different types of hydrophobic coating materials were used: spray-coated Glaco Mirro Zero (Soft99), vaporcoated parylene-C (SCS coatings), and FOTS (Sigma–Aldrich). The patterning was done via shadow masking (Glaco Zero and FOTS), or photolithography followed by oxygen plasma etching (parylene-C).

3.4.2 Hydrogel bilayer patterning using TPP system

A detailed recipe of the functional/nonfunctional substrates is listed in **Table 3.2**. A 2.5mL of non-functional PAAm solution was dispensed onto the hydrophobic/hydrophilic bottom plate with a defined gap size and gelled to form a thin film (**Fig. 7.1**). This was followed by 40 μL of PAAm solution with varied Sodium Acrylate(SA) concentration dispensed onto another prefabricated hydrophobic/hydrophilic patterned plate with a spacer to adjust the overall thickness of the functional patterns (**Fig. 7.1**). For pattern transfer, the PMMA plate containing nonfunctional thin film was placed over the multipatterned functional gels and allowed to cross-link. Afterwards, to achieve multi-configurable 3D shape-morphing states, the patterned non-functional substrate was allowed to freestand in different ionic concentrations of PBS and water for 10 min. The pre-gel solutions were dispensed to polymerize and shaped inside a Hele-Shaw cell (TPP) layered by hydrophobic and hydrophilic boundaries inside the TPP system before polymerization.

	Acrylamide (wt%)	*Bisacrylamide (wt%)*	*TEMED (wt%)*	*APS (wt%)*	*SA (wt%)*
Pattern I (1B3S)	18.816	3.494	0.168	1.68	16.128
Pattern II (1B1S)	18.816	3.494	0.168	1.68	5.376
Substrate (nonfunctional thin film)	14	0.45	0.35	3.6	0

Table 3.2 Compostion of high/low swelling functional patterns on a non-functional thin film

3.5 Characterization Methods

Characterization 1: *High Speed Camera imaging:* To, understand how the soft system behaves upon contact with the hot surface, it is important to visually understand the morphological changes underwent at the point of impact and the dynamic behaviour during the time of flight process. The basic principle of this device is centred on the tracking and capturing of rapidly bouncing gel spheres on a hot surface and its dynamic gap oscillation movements at the surface interface. The overall design principle of the imaging process is illustrated in **Fig 3.7**. The dynamic behaviour of the gel sphere was captured at an increased frame rate around 5000FPS using a high-speed camera (HotShot CC) as shown in **Fig. 3.8a** which bounces on a hot plate (IKA C-MAG HS7). The temperature of the wafer surface was measured using a thermal camera (FLIR T660) for accurate measurement.

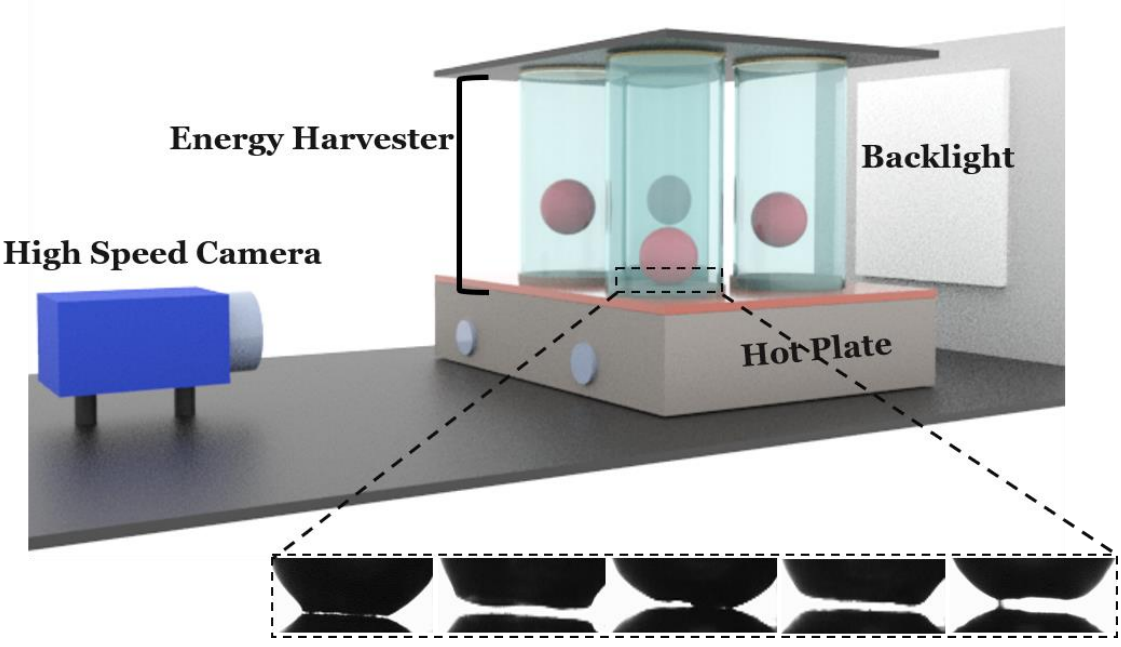

Figure 3.7. Schematic representation of the high speed camera setup to capture the dynamic behaviour of thermoelectric soft engine; real time photographs of gap oscillations taken at 5000 FPS (inset)

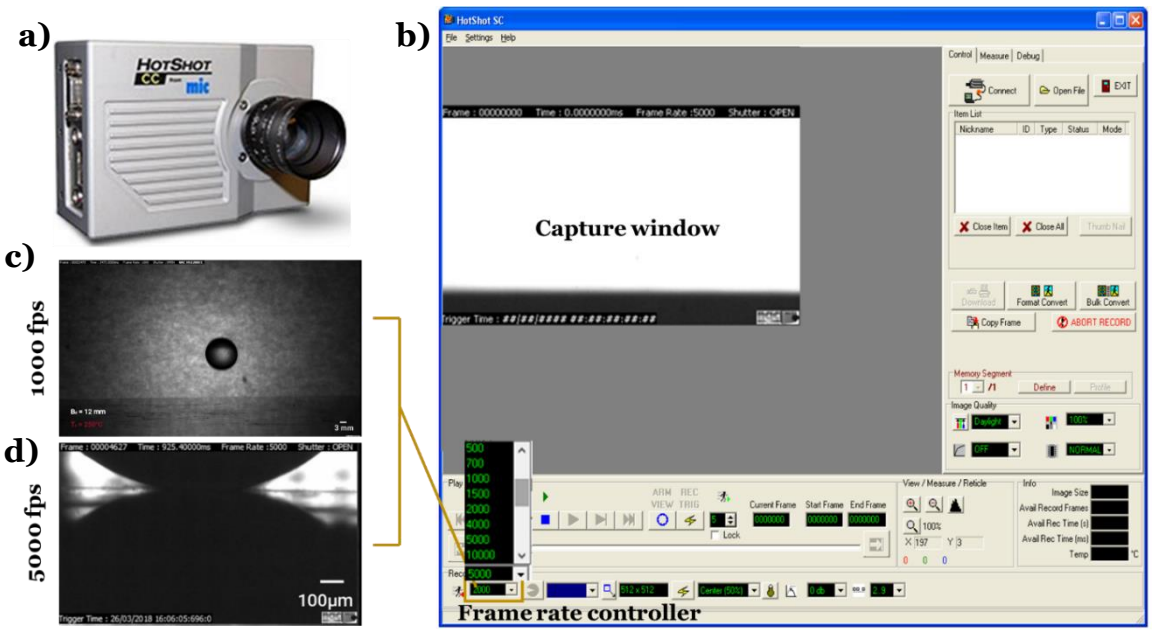

Figure 3.8 a) High speed capture device – Hotshot CC; **b)** Example of high speed motion capture software interface; and High speed captured images of bouncing gel sphere captured at two extreme framerates of **c)** 1000 FPS and **d)** 5000 FPS.

As mentioned earlier, the high speed capture analysis of the invisible gas-oscillation behaviour and deformation of the gel sphere are carried out using the specialized software interface seen in **Fig. 3.8b**. Before the actual capture starts, the background light is adjusted to provide maximum featuristic profile of the gel sphere impact at/away from the surface. By setting the frame rate tool, a range of frame rate conditions can be developed to provide a wholistic dynamic behaviour of the gel sphere (depending on the size of the sample) as shown in **Fig. 3.8c** or a detailed micro-deformation underwent by the gel sphere upon contact with the hot surface as shown in **Fig. 3.8d**.

Characterization 2: *Surface Morphology characterization:* For capturing and measuring the first visual site of designed structure and how its behaviour with strain change, an upright optical microscope (Nikon LV-100, brightfield

reflection mode) and ImageJ 1.50i/Java 1.6.0_24 software were used. Scanning electron microscopy (SEM, MIRA3, TESCAN) was used to observe the surface structures. Atom force microscopy (AFM, D3100, Veeco) and Bruker® GTK interferometer provided a range of in-plane surface morphology change. A KRUSS® DSA 30S Drop Shape Analyser (**Fig. 3.9a**) was used to measure the surface contact angles of different liquid droplets on hybrid groove-hydrogel surfaces (**Fig 3.9b**), and anodized surface under different environmental conditions.

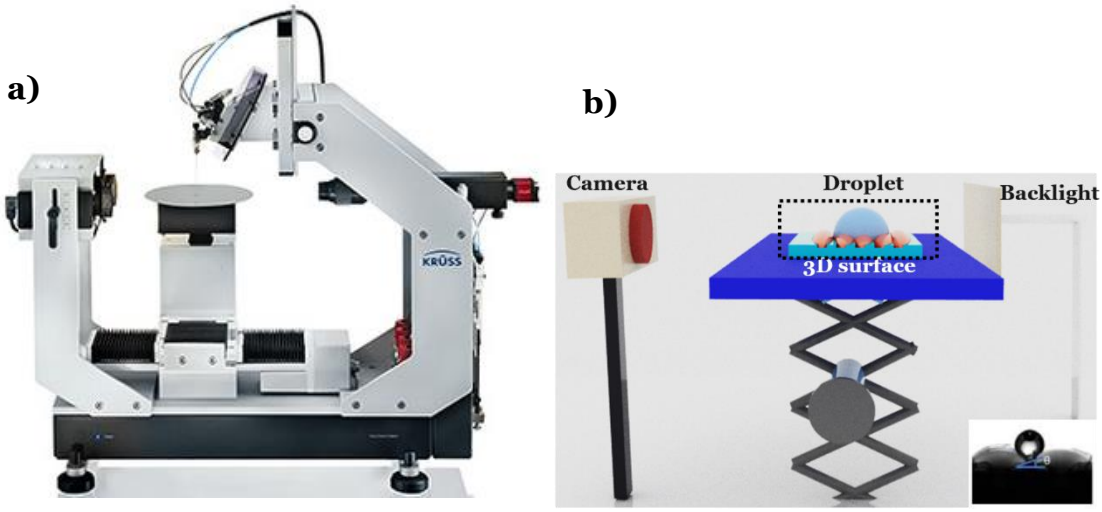

Figure 3.9 a) Droplet shape analyser used to analyse the surface wettability feature; **b)** Schematic illustration of the principle behind surface wetting studies carried out using DSA with a representative droplet behaviour (inset) on a special

3.6 Theoretical methodology

3.6.1 Viscoelastic modelling

The Computational methodology used to understand the theoretical knowledge of the bouncing system was solved by a combination of SOLID168 element geometry and viscoelastic model. SOLID 168 is a higher order 3-D, 10-node explicit dynamic element that uses irregular meshes which are produced from various CAD/CAM systems. The element is defined by ten nodes having three degrees of freedom at each node: translations in the nodal x, y, and z directions as discussed later in the thesis. By default, SOLID168 exploits a quadratic displacement characteristics with five point integration (KEYOPT(1) = 0 or 1) and uses an assemblage of linear sub-tetrahedral shapes (KEYOPT(1) = 2). Such a combination will help to overcome the lumped mass calculations and volume locking inherent to the quadratic elements. There are 4 key parameters: G_0, G_∞, K, and $1/\beta$ which are considered as shown in **Table 3.3**.

	$\boldsymbol{K}=$	$E=$	$\lambda=$	$\boldsymbol{G}=$	$\nu=$	$M=$
(E, ν)	$\dfrac{\boldsymbol{E}}{\boldsymbol{3(1-2\nu)}}$		$\dfrac{E\nu}{(1+\nu)(1-2\nu)}$	$\dfrac{\boldsymbol{E}}{\boldsymbol{2(1+\nu)}}$		$\dfrac{E(1-\nu)}{(1+\nu)(1-2\nu)}$

Table 3.3 Parameters considered for viscoelastic simulation

Along with SOLID168, a viscoelastic model is also used in parallel to study the linear viscoelasticity of a polymer in relation to their relaxation time at the point

of contact with the surface. The viscoelastic model also helps in unravelling the dependencies between the molecular architectures of the polymeric substrate with relaxation time using a simple geometry. Some of the parameters that are widely considered are chain flexibilities, rotational energy between the chemical bonds, molecular interaction forces, and few add-ons such as solvent, phase transitions of the polymeric composite. A viscoelastic material which imparts a dual characteristics of both viscous and elastic nature during loading is used in our ANSYS LS-DYNA model. In general, a vehicular shock absorber, consisting of a spring and a damper, is a traditional structural component that portrays in a viscoelastic manner. The damper (in our case, the polymeric composite) reduces the shock and absorbs some of the energy, while the spring (crosslinker density) serves to elastically recoil the component back to its original shape. The three main characteristics that defines the viscoelastic materials are creep, stress relaxation, and hysteresis. The elastic recoiling and rebound behaviour of the soft polymeric ball can be approximated by a proper arrangement of springs and dampers. Few of the commonly used spring–damper models are the Kelvin–Voigt model (a spring and a damper in parallel) and Maxwell model (a spring and a damper in series). However, in our study, a commonly used viscoelastic material law based on the linear viscoelastic properties reported by Herrmann and Peterson was used. This material is chosen by superposition of a linearly viscoelastic material and an elastic material under hydrostatic pressure. Hence, we define the overal behaviour of a viscoelastic material by its shear deformation, with the time-dependent shear relaxation modulus defined as follows:

$$G(t) = G_{\infty} + (G_0 - G_{\infty})e^{-\beta t} \tag{18}$$

Wherein, G_0 is the unrelaxed sheer modulus or short-term shear modulus, G_{∞} is the relaxed shear modulus or long-term shear modulus and β is the decay

constant. In the model, the overal elastic bulk behaviour is considered when calculating the incrementally integrated viscoelastic pressure from the volume, $V: p = K \ln V$. The major advantages of this explicit approach are that it provides information based on the time-history of the sphere impact and recoil time compared with the experimental tests and has a lower computational cost compared to direct frequency response analysis.

3.6.2 Finite Element Analysis

The commercial finite element software ABAQUS is adopted to conduct the simulations. 2D plane-strain condition is assumed. Both the functional gel blocks and the non-functional substrate are modelled as hyper-elastic incompressible neo-Hookean material. For the functional gel, a non-zero thermal expansion coefficient is introduced. Moreover, the element type of "Coupled Temperature-Displacement" is selected and the step of "Coupled tempdisplacement" is created to conduct the coupled thermo-mechanical analysis, i.e. solving simultaneously the mechanical equilibrium equation (for deformation) and the heat transfer equation (for temperature) with thermal expansion/contraction considered. The surface heat flux entering the gel is used as thermal load to induce the thermal expansion while the one leaving the gel is used for thermal contraction.

By immersing the gel structure in the PBS solution, the functional gel blocks will expand (swell) or shrink (de-swell) depending on the concentration of PBS solution. The mismatched strains between the expanded/contracted functional gel blocks and the non-functional substrate will induce an internal stress, which leads to the bending behaviour of the gel structure. To simultaneous

simulate the expansion (swelling) and contraction (de-swelling) of different gel blocks under the same ionic environment (i.e. same PBS solution), complex diffusion kinetics must be developed, and the resulted coding and computation will be time consuming. Therefore, we used the thermal expansion and contraction instead, which has already been incorporated in most commercial computing software. It is noted that our aim is to demonstrate a proof-of-concept simulation targeting at structure deformation design, not to precisely model the different diffusion processes. Meanwhile the reconfigurability of the same bilayer heterogeneous structure was also studied.

Three simulation results corresponding to three tests are shown in the paper: (1) one gel block expands with the principal strain around 0.25 and the other one contracts with the principal strain around −0.2, corresponding to the test of immersing the heterogeneous gel structure in the 0.2M PBS solution for 2 minutes; (2) both gel blocks contract with the principal strain around −0.2, corresponding to the test of immersing the gel structure in the 0.5M PBS solution for 2 minutes; (3) one gel block expands with the principal strain around 0.25 and the other one expands with the principal strain around 0.1, corresponding to the test of immersing the gel structure in the DI water for 2 minutes.

Chapter 4

Thermo-anodized porous surfaces with innate UV resistance and anti-freezing facets

4.1 Introduction

Controllable thermo-anodized coating (CTC), a passive and effective method to ensure the operation of spacecraft, has attracted considerable research interests in recent years. Such control coatings have been used in the electronic housing packages of spacecraft with black CTC on the alloys, to facilitate high solar absorptivity and high emittance[210]. Recently, high demand of such coating mechanism was observed in response to the growing applications in aerospace engineering, where the technical focuses are to develop CTC surfaces with resistance against corrosion and icing, as well as high solar absorptivity (α_s) and thermal emittance (ε).

In materials point of view, a superior strength, i.e. strength-to-weight ratio, and durability are key important features for materials to be considered in aerospace and space voyage industries. Aluminum (Al) alloys are the most widely used materials that exhibits mild anti-corrosion behaviour with reduced solar absorptivity and thermal emittance. Studies using Plasma Electrolytic Oxidation on different aluminium alloys yielded a high solar absorptivity with low corrosion resistance whereas treatment using micro-arc oxidation produced improved corrosion resistance with no studies on solar absorptivity and thermal emittance[220]. During anodization of alumina using acidic electrolytes, the

alumina forms porous oxide layer which is protected by a compact barrier layer. The physical properties of the barrier layer such as pore size, pore wall thickness, etc are often influenced by anodizing conditions such as voltage, electrolyte temperature and anodizing time. In addition to maintain a balanced physical characteristic, one should also focus on the corrosion resistance, ice accretion behaviour on aircraft surfaces to reduce safety risk and increase energy efficiency[225]. The ice adhesion properties on the surface can be treated by modifying the wettability of the surface which in turn can be influenced by morphology of the porous alumina while anodizing. Furthermore, posttreatments such as hydrothermal sealing (HTS) and silanization can also be applied to support improved anti-wetting properties. Smart anodic coatings can provide improved cost-efficiency in the aircraft industry with safety and environmental sustainability. Enhanced corrosion resistance can also maintain and avoid replacement of aircraft parts. With less or no ice adhesion, the risk for fatal accidents and fuel consumption can be profoundly declined.

Hence, a conventional processing technique to fabricate high performance Aluminium alloy with improved absorptivity and emittance has not been exploited elsewhere. In this chapter, we propose to investigate the influence of thermoanodization on the porous alumina morphology, draw relationships between ice adhesion and morphology-dependent wettability post treatments to obtain tuned sustainable anodic coatings for extreme applications in space-voyage, aircraft, etc.

4.2 Results and Discussion

4.2.1 Anodization conditions and morphology

We first investigate the effects of anodizing conditions (i.e. temperature and current density) on the formation of microstructure (thickness, surface roughness and porosity), where the microstructure is anticipated to be tuned with dependencies on the current density and/or the anodizing temperature. Therefore, surfaces were anodized under various conditions (**Table 4.1**) and the morphology was studied using SEM. As the conditions were tested using multiple parameters, a comparison between these is given. Thereafter, the effects of the anodizing current, and anodizing temperature on the morphology are presented below.

H_2SO_4 (g/L)	$H_2C_2O_4$ (g/L)	$C_4H_6O_5$ (g/L)	$Fe_2(SO_4)_3$ (g/L)	T °C	I (A/dm^2)	Time (min)
30	40	30	6	0	3-7	60
30	40	30	6	0-10	5	60

Table 4.1 The electrolyte composition and processing parameters for anodization process.

Since the time effect for anodization has been well understood, we have compared the overall surface morphology and polarization curves for the sample fabricated under different anodization duration (**Fig. 4.1**), and find that the quality of coating would decrease if the processing time was more than 60 min due to the increasing rate of the anodic oxide coating dissolution, thus, we choose the

processing time of 60 min for the rest of study. Hence, we focussed on the effects of anodizing conditions (i.e. temperature and current density) on the formation of microstructure (thickness, surface roughness and porosity**, Fig. 4.2**, where the microstructure is anticipated to be tuned with dependencies on the current density and/or the anodizing temperature.

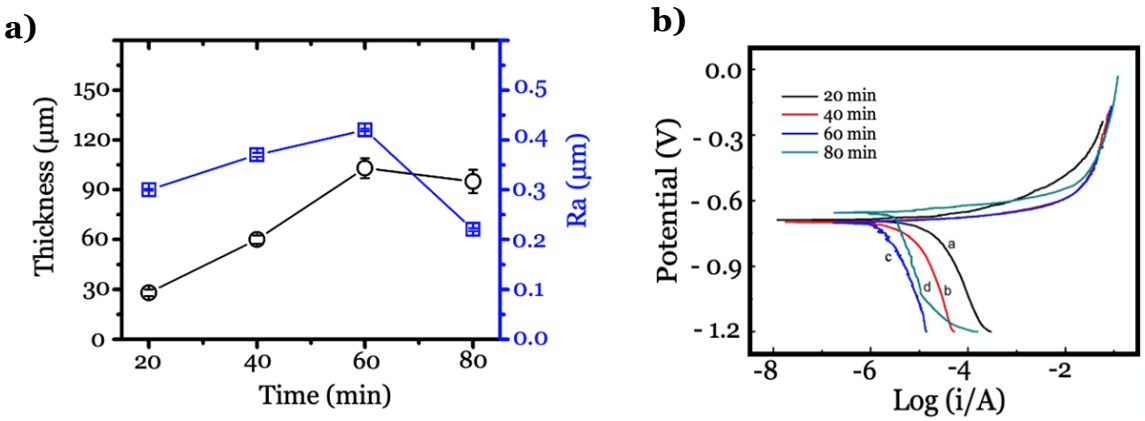

Figure 4.1 a) Effect of processing time on of the anodic oxide coatings thickness and the roughness measurement, **b)** Tafel curves of the anodic oxide coatings under different processing time.

The results from the SEM experiments performed on surfaces anodized with current densities ranging from 1 A/dm² to 9 A/dm² are shown in **Figure 4.2**. The anodization time was kept constant and anodizing parameters such as anodizing temperature and current density were kept changing to facilitate range of microstructures on the anodized surface. The SEM observations suggest a controllable formation of porous surface from the pristine surface under thermo-oxidization, with unravelling of uniform distribution of porous surface spanning around 20 nm in pore diameter at a current density of 5 A/dm² and temperature of 10°C. The experiment also sheds light on the first evidence in controlling the porous size and number depending on the prerequisites of the conditions.

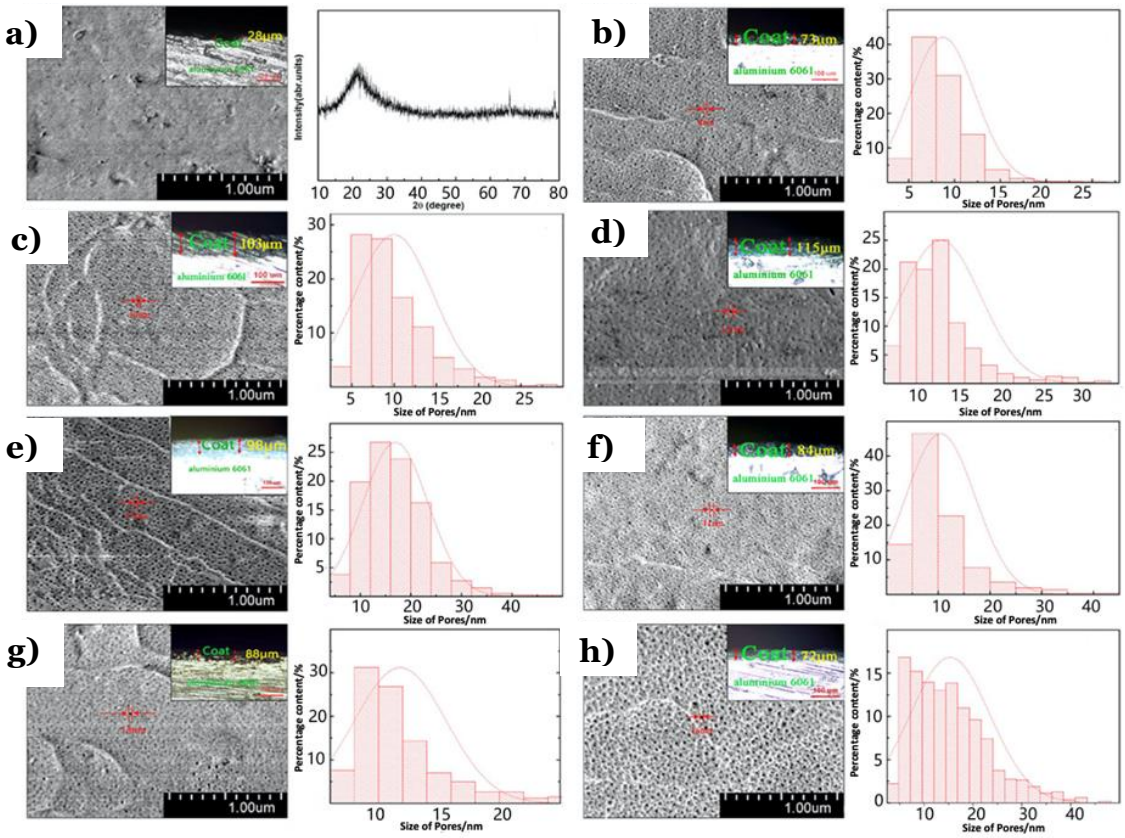

Figure 4.2. **a)** Surface morphology for original aluminum surface and XRD analysis of coating under 0℃ and 5 A/dm² for 60 min. Surface morphologies of coatings at different current densities and anodizing temperatures: **b)** 1 A/dm², 0℃; **c)** 3 A/dm², 0℃; **d)** 5 A/dm², 0℃; **e)** 7 A/dm², 0℃; **f)** 9 A/dm², 0℃; **g)** 5 A/dm², 5℃; **h)** 5 A/dm², 10℃. Samples were anodized in the electrolyte exhibited in Tab.1 under 0 ℃ and 5 A/dm² for 60 min. All the scale bars in the insets are 100 nm.

When the current density increases (**Fig. 4.2**), the thermal effect accelerate the mobility of OH− in electrolyte, thus lead to the dissolution of solid layer and increases the pore size. As shown in **Fig. 4.2 c, 4.2 f - 4.2 h**, such increase in the average pore size (from 10 nm to 16 nm) is discovered when the anodizing temperature increase from 0 ℃ to 10 ℃ results in the formation of black surface. There is an interesting presence of wavy structures in **Fig. 4.2b**, which is formed due to the break in equilibrium of a pristine coating layer before the growth of

porous structure is initiated. XRD results in **Fig. 4.2a**, show a broad, bread-shaped peak in the range of 15°~ 30°, which may be affiliated with the Amorphous amorphous alumina. Other sharp diffraction peaks correspond to those from the γ-Al_2O_3. The appearance of black surface is caused by the formation of magnetite Fe_3O_4. In order to verify the iron ions within the anodic oxide coatings, the XPS analysis were was performed and all binding energies were calibrated at 284.6 eV with an indefinite carbon C1s. The results in **Fig. 4.3a** clearly show C, O and Fe elements on the surface of anodic oxide coatings. **Fig. 4.3b** shows the binding energy of Fe 2p, which can be divided into two different components, representing two different oxidation states for iron in the coatings. At 710.4 and 724.1 eV, the corresponding peak was Fe^{2+}; at 712.3 and 726.1 eV, the corresponding peak was Fe^{3+}. The peaks were related to 2p3/2 and 2p1/2 signals of octahedral Fe^{2+}, Fe^{3+} and tetrahedral Fe^{3+}, respectively, which prove the existence of Fe_3O_4.

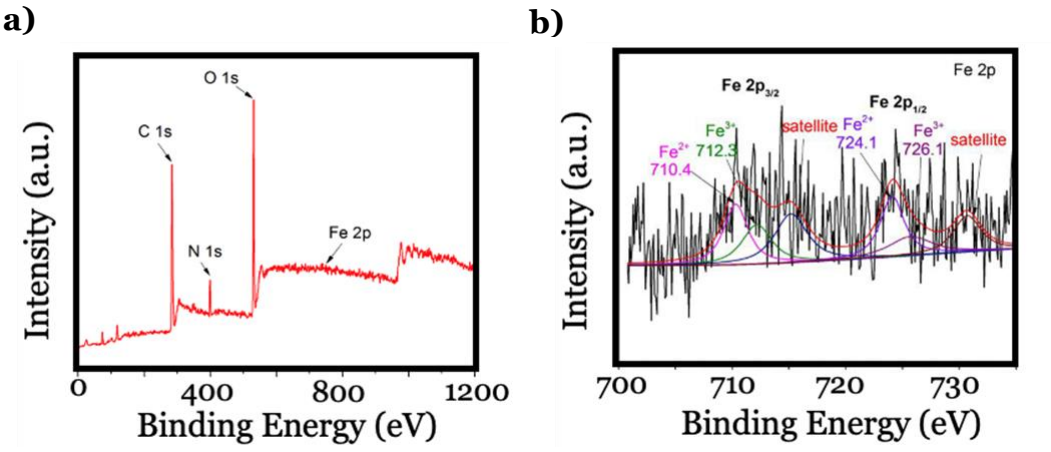

Figure 4.3 XPS analysis of the black coated anodic oxide surface

The morphology of porous aluminium oxide layer is highly influenced by the surface roughness of the aluminium electrode. For this reason, large cavities can be observed in the SEM images as seen in **Fig. 4.2** complemented by dynamic changes in the surface roughness profiles. It is believed that as the anodic current density increases (**Fig. 4.4**), the thermal effect accelerates the mobility of OH^- ions within the electrolyte, and activates the overal dissolution of solid layer with increase in the pore size. These interconnected pores are especially clearer as the anodizing temperature is increased which are observed clearly as bright color on the alloy's microstructure, likely due to topographical height formation of the anodic coating.

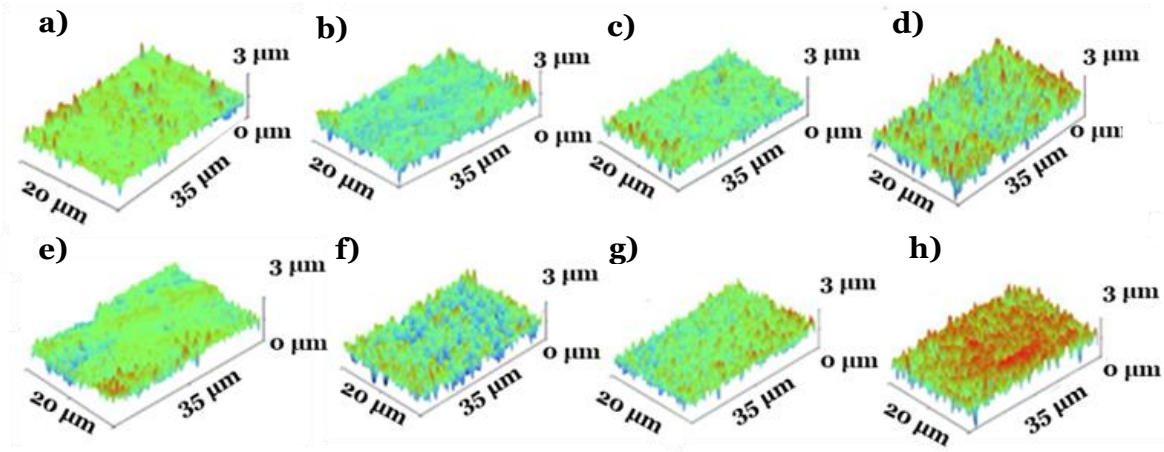

Figure 4.4 Coating thickness and roughness at different current densities: **a)** 1 A/dm²; **b)** 3 A/dm²; **c)**5 A/dm²; **d)** 7 A/dm²; **e)** 9 A/dm². Samples were anodized in the electrolyte exhibited in Tab.1 at the anodizing temperature of 0 °C for 60 min. Coating thickness and roughness at different anodizing temperatures: **c)** 0°C; **f)** 5°C; **g)** 8°C; **h)** 10°C. Samples were anodized in the electrolyte exhibited in Tab.1 under the current density of 5 A/dm² for 60 min.

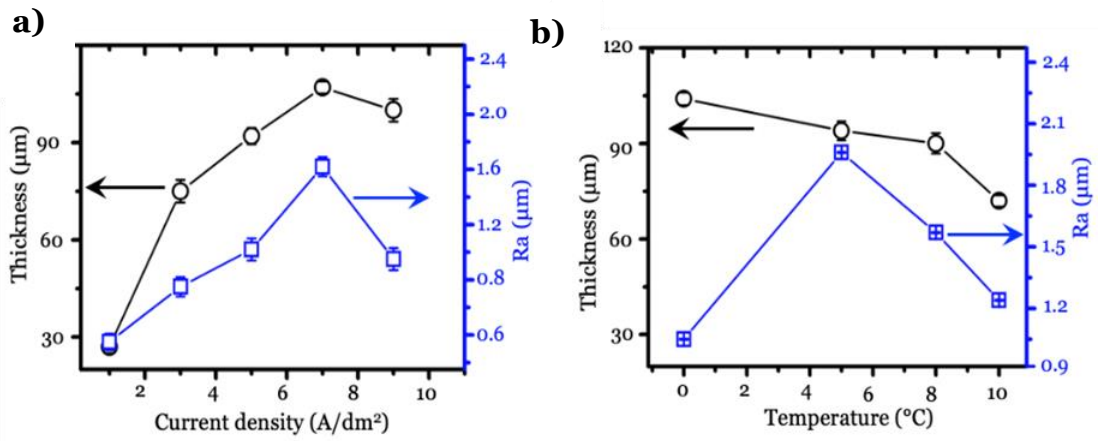

Figure 4.5 a) Oxidization current density at a fixed temperature of 0 °C, and **b)** oxidization temperature at a fixed current density of 5 A/dm²

The thickness of oxide layer formed and surface roughness observed due to current density and anodic temperature are plotted in **Figure 4.5**. All working anodic temperature and current density regardless of the set-up used are included. In **Fig. 4.5a**, the thickness and roughness of coating layer are found to increase as the anodizing current density increases, with a maximum thickness (115 µm) and roughness (1.6 µm) obtained at a current density of 7 A/dm², wherein the reaction efficiency seems to reach the peak since due to the anodization equilibrium can be supported with by the local components of anodization along with with the sustainable mass transportation within solution. In **Fig. 4.5b**, a slightly mixed trend for the coating thickness and roughness are presented when the anodizing temperature (T) increases. The maximum thickness (103 µm) is obtained at T=0 °C, while the maximum roughness (~ 2 µm) is obtained at T=5 °C. While the increased dissolution rate at higher temperature encourages the removal of residuals, supported by drop in surface roughness, the elevating temperature also accelerates the dissolution of anodizing coating (i.e. coating layer), resulting into the reduction of surface thickness. The average pore size vs anodic current density in **Fig 4.6** unveils the trend when tuning the

anodization current density and temperature, but should be noted that the surface will get rougher and achieve inhomogeneity, thus affecting the homogeous distribution of the porous nature quality on the coated surface.

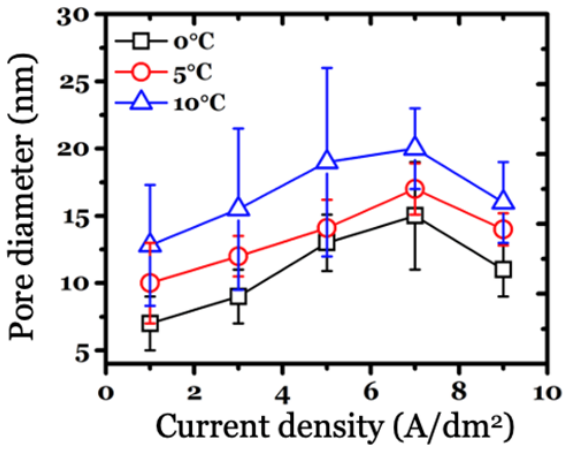

Figure 4.6 The average pore size vs anodic current density for the sample fabricated under different temperature

4.2.2 Performance analysis of solar absorption and emittance behaviour

We next investigate the solar absorptivity and emittance performances for the anodized layers, which are usually considered as key factors in aerospace engineering applications. In **Fig. 4.7a**, the reflectance of coating decreases significantly when the current density changes from 1 A/dm² to 3 A/dm², then reduces gradually with further increase in current density. When the current density reaches above 1 A/dm², the reflectance value drops due to the rapid growth of anodized layer, which breaks the equilibrium to nucleate pristine oxidized coating layer. When the current density further increases above 3 A/dm², the uniform growth of porous structure can be established, therefore

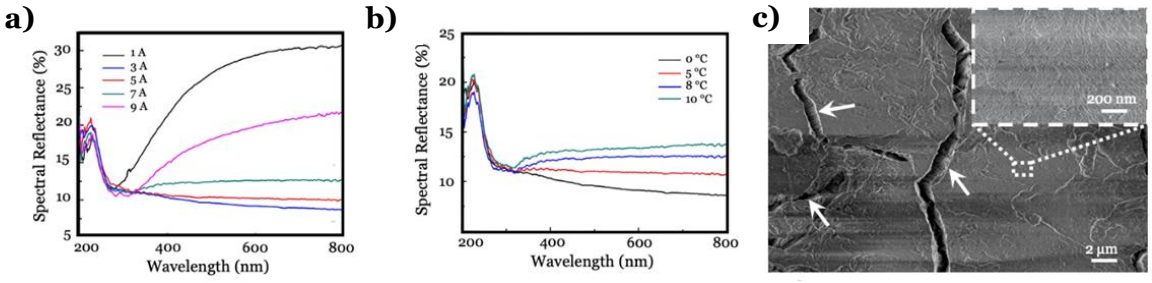

Figure 4.7 The spectral reflectance plots versus **a)** different current densities at 0 °C for 60 min, **b)** different temperatures under 5 A/dm² for 60 min. **c)** The SEM image of thermo-anodized surface at 8 °C.

yields the increase in coating reflectance. It is noticed that the coating reflectance also increase when temperature elevates (**Fig. 4.7b**) at a fixed current density of 5 A/dm², where a higher temperature is thermodynamically favourable to create the anodization equilibrium, leading to a regular growth of porous structure and an increased reflectance. However, cracking seems likely to occur on the coating film (**Fig. 4.7c**) at a higher temperature (8°C or above), due to the local stress localization during the intensive growth of layer.

The solar absorptivity (α_s) and emittance results for the anodized surfaces under different processing conditions are summarized in **Fig. 4.8a - 4.8b**. A set of absorptance (α_s) values are obtained as 0.673, 0.897, 0.921, 0.881, 0.845, at a varying current density settings from 1 A/dm² to 9 A/dm², respectively. Compared with the smooth untreated Aluminium alloy surface with an absorptivity of 0.557 and an emittance of 0.16, significant enhancements are achieved with an absorptivity of 0.921 and an emittance of 0.96 for the anodized layer. When the anodizing temperature increases (**Fig. 4.8b**), the solar absorptivity α_s shows a decreasing trend from a value of 0.921 at 0 °C, to a value of 0.862 at 10 °C. By plotting the absorptivity and emittance as function of coating thickness (**Fig. 4.8c**), we find that both absorptivity and emittance increase

when the thickness increases initially and reached a plateau at around 50 μm. Our hypothesis is that the surface homogeneity at around 50 μm providing the best absorbing feature. However, what we still need is to further explore the hidden mechanism of the porous morphology (incl. film qualities and structures), and present it in the future studies.

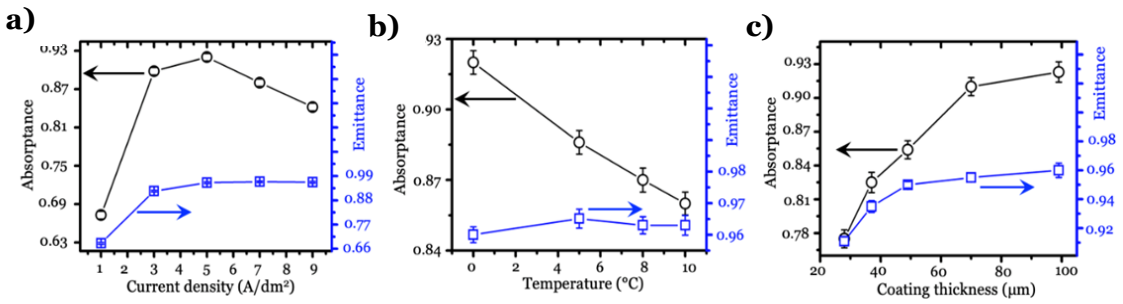

Figure 4.8 Solar absorptivity and emittances at **a)** different current densities and **b)** different anodizing temperatures. **c)** absorptivity and emittance for the coatings versus coating thicknesses.

4.2.3 Corrosion resistance behaviour of black coated aluminium alloys towards UV

We then study the UV-resistance of CTC coating layer under UV irradiation (400 nm). Prior to the UV irradiation, we benchmark the potentiodynamic polarization curves in **Fig. 4.9a** and **4.9c** for the fabricated samples, which show that the most positive corrosion current density and self-corrosion potential of 1.148E-5 A/cm² and -0.545 V are obtained at the current density of 5 A/dm² and the temperature of 0 °C. These result shows the best coating resistance to corrosion. After UV irradiation, the potentiodynamic polarization curves (**Fig. 4.9b and 4.9d**) suggest very little changes on the overall corrosion current density. For the layer fabricated at an optimal state with a current density of 5 A/dm² and a temperature of 0 °C, the most positive

corrosion current density and self-corrosion potential are 1.659E^{-5} A/cm^2 and -0.565 V, which indicate that the anodized porous layer possesses an effective UV shielding feature. As the temperature and anodic current density increases, the rate of dissolution of ions on the surface is accelerated leading to pronounced corrosion/pitted surfaces, resulting in decrease on UV resistance on surface.

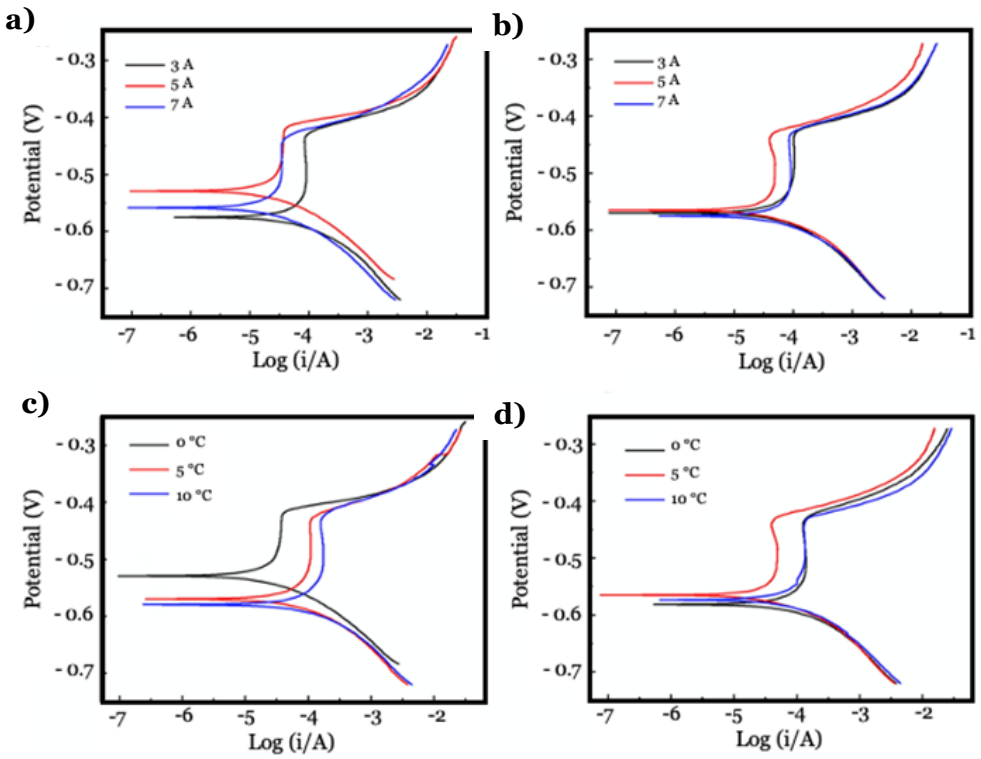

Figure 4.9 Potentiodynamic polarization curves of coated aluminium alloys at 0 °C for 60 min under different current densities in 3.5% NaCl solution, **a)** without UV irradiation, **b)** under UV irradiation (400 nm). Potentiodynamic polarization curves of coated aluminium alloys at 5 A/dm2 for 60 min under different temperatures in 3.5% NaCl solution **c)** without UV irradiation, **d)** under UV irradiation (400 nm).

4.2.4 Silane assisted superhydrophobicity and performance characteristics

Here, we developed a hybrid strategy to apply a salinization layer to seal the anodized surface, through a hydrolysis reaction, where the silanol groups react with the hydroxides to generate strong Si-O-Me metal bonds. The silane reaction on the surface imparts the necessary hydrophobic character due to the controllability over interpore distance present on the thermo-anodized aluminium oxide surface by providing larger effective contact area between liquid impregnating the surface (Wenzel state)[46]. Such Si-O-Me network is expected to work with the anodized porous surface to provide a longer uniform nonpolar alkyl chains that induces superhydrophobicity with prevention of penetration in corrosive solution Such Si-O-Me network prevent the penetration of corrosive solution, so that the remaining silanol groups condense into Si-O-Si bonds, originating highly cross-linked uniform siloxane hydrophobic layer. The above reactions are illustrated as following:

$$NH_2(CH_2)_3Si(OC_2H_5)_3 + 3H_2O = NH_2(CH_2)_3Si(OH)_3 + 3C_2H_5OH \quad (19)$$

$$Al(OH)_3 + NH_2(CH_2)_3Si(OH)_3 = (OH)_2Al - O - Si(OH)_2NH_2(CH_2)_3 + 3H_2O \quad (20)$$

$$NH_2(CH_2)_3SiOH + NH_2(CH_2)_3Si(OH)_3 = NH_2(CH_2)_3Si - O - SiNH_2(CH_2)_3 + H_2O \quad (21)$$

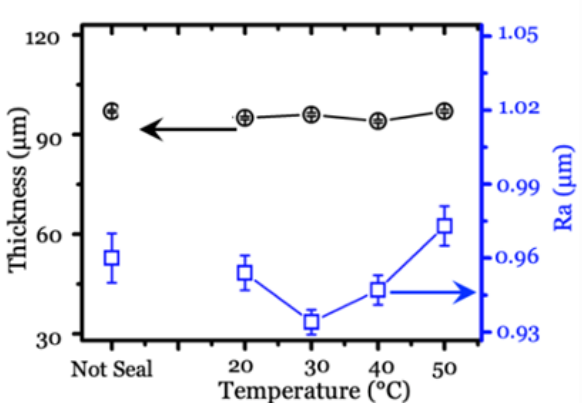

Figure 4.10 The thickness and roughness of coatings after annealing at different temperatures

The optimal surface state is achieved at an annealing temperature of 30 ℃ (**Fig. 4.10**), where the surface roughness value shows a smallest value of 930 nm, and no obvious changes on overall coating thickness (**Fig 4.10**). The reflectance results (**Fig. 4.11a**) indicates limited changes in plateau values due to the stable thickness. While the emissivity results can be measured, the solar absorptance (α_s) values are calculated from following equation,

$$\alpha_s = 1 - \rho_S = \int_{\lambda_1\lambda_2} \rho_\lambda S_\lambda d_\lambda / \int_{\lambda_1\lambda_2} \rho_\lambda d_\lambda \quad (22)$$

where λ is the waverlength dependence, ρ_S is the reflectance of coating, S_λ is the spectral solar irradiance. An emittance peak value (0.975) is obtained at a hydrolysis temperature of 50 ℃ (**Fig. 4.11b**), while the absorptance remains nearly unchanged. Considering the diameter of pores between 10-50 nm, the light wavelength is too large to enter the oxide layer pores caused by uneven roughness on the surface before and after coating with silane layer. Hence, the surface

roughness should be considered before annealing of silane coating on the surface to determine a superior emittance and absorptance characteristics.

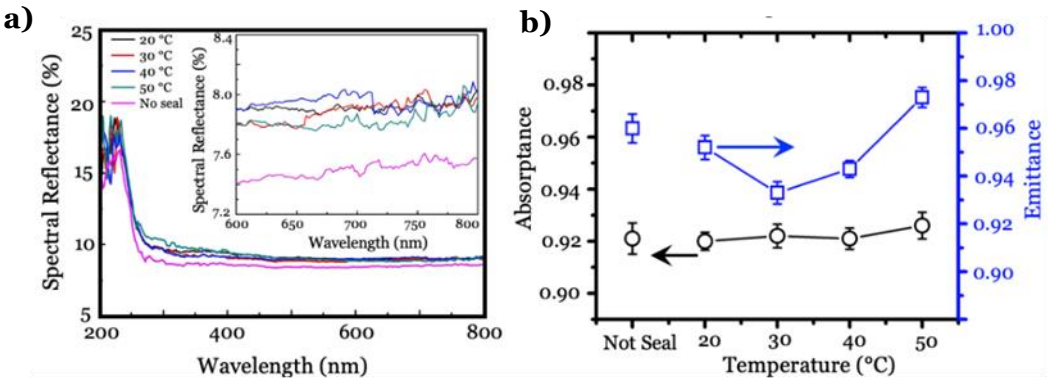

Figure 4.11 a) The reflectance results of untreated coating and hybrid coatings at different temperatures. **b)** absorptivity and emittance for the hybrid coatings annealed at different temperatures.

4.2.5 Anti-icing behaviour

Ice adhesion measurements on the silanized anodic aluminium surface were performed using a contact angle measurement tool. The resistance of water residual onto the silane coated porous anodic aluminium oxide layer to dealy delay the formation of ice can be explained by the hypothesised Wenzel to cassie-baxter transition state (**Fig. 4.12a**). For the porous alumina surface without the addition of silane layer, a contact angle of less than 60° is obtained due to the impregnation of water droplet within the porous surface exhibiting a hydrophilic state. As the porous aluminium surface is incubated with silane layer at lower temperature, a partial/half-porous surface is yielded with increase in CA to 80° under full Wenzel or near-Wenzel intermediate state. However, as the silane coating is incubated at higher annealing temperature of 30°C, a strong adhesion between silane coating and the anodic surface is observed with an increased CA of 125°. This value undoubtedly belongs to a complete or near-cassie intermediate

state. Thus the annealing temperature of the silane coating can also induce the transition between Wenzel to Cassie state for as-prepared porous alumina surface. The surfaces were simultaneously annealed under different temperature conditions and silanized to measure the contact angle prior to and post silane treatment. In **Fig. 4.12b - 4.12e**, contact angle (CA) results clearly demonstrate the shift of CA value from 74° at an annealing temperature 20 ℃, to 134.5° when the silane annealing temperature is 40 ℃. The summary of CA and contact angle hysteresis (CAH) in **Fig. 4.12f** shows that the surface is most hydrophobic and has the lowest CAH value at an annealing temperature is 40 ℃. It should be noted that the CA value decrease at an annealing temperature 50 ℃, which agrees with the rising of roughness in **Fig. 4.12c**. The reason could be the breaking of thermal dynamic equilibrium at a high temperature, yielding an early termination of reaction to generate uniform surface silane network. The icephobic measurement was performed on the surfaces of untreated CTC coating (**Fig. 4.12g**) and hybrid CTC surface at an annealing temperature of 40 ℃ (**Fig. 4.12i**). From **Fig. 4.12g-4.12j**, the icing process takes 15 sec for hybrid surface, which is 150% of the time on untreated surface (10 sec) and clearly demonstrates the anti-icing function for hybrid surface.

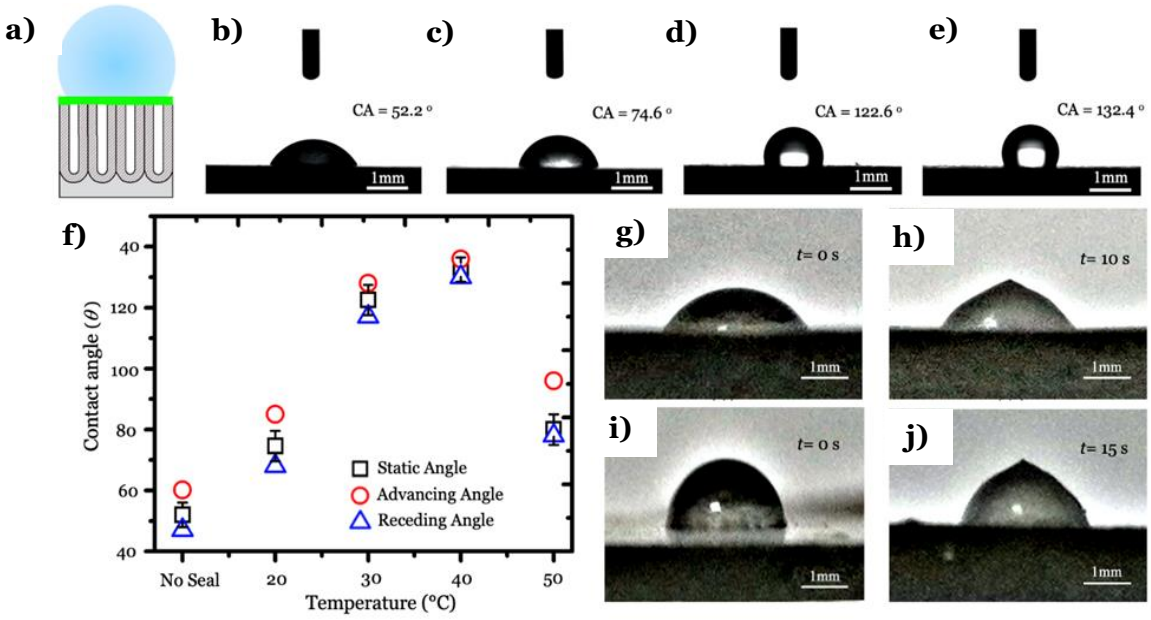

Figure 4.12 Schematic illustration of the hydrophobic state in **a)** Observations of contact angles for sample with **b)** no seal and with AAO coatings annealed at **c)** 20°C, **d)** 30°C, **e)** 40°C. **f)** Summary of contact angles with contact angle hysteresis data. Observations of icing process of a single droplet of DI water on untreated CTC surface (g) liquid as deposited and **h)** frozen state, and on hybrid surface with silane annealed at and 40 °C **i)** liquid as deposited and **j)** frozen

The as-prepared hybrid surface exhibited improved anti-icing feature but the duraility of the silane coating is of primary concern. Du et al reported that the sole Si-O-Me network on flat aluminium does not work effectively to resist the ice. [275] The Si-O-Me network on porous anodized surface remained hydrophobic for 100 hours in water (CA ~ 119°±9°) due to the presence of water environment which would have breached the hybrid layer (**Fig 4.13a**). However, in the absence of water, the hybrid surface posed a superior anti-wettability due to strong hybrid layer and exhibited robustness (~ 150 decrease in static CA) after 50 rounds of icing tests, as shown in **Fig. 4.13b**. We believe this robustness is attributed to compensation of the silane layer that was lost during icing/de-icing process by surface's porous capillary action.

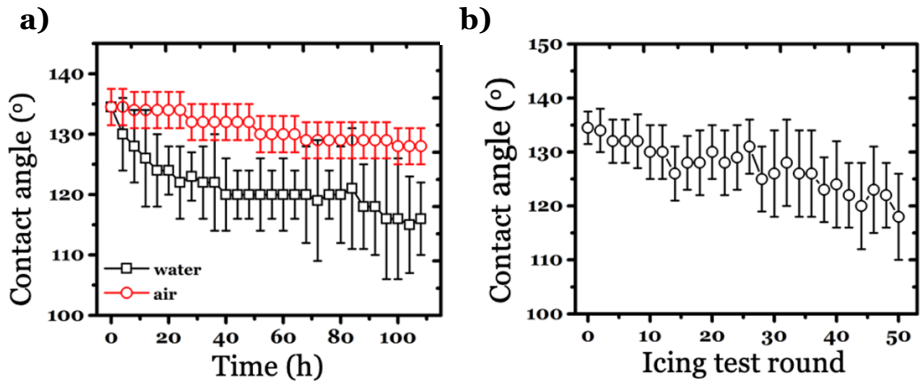

Figure 4.13 Robustness assessments for the hybrid surface by tracking static CA values as functions of **a)** the exposure time to open air and immersing time in water; **b)** the icing testing rounds.

4.3 Conclusion

The conditions tested herein were the anodizing current, anode temperature and anodizing time. In turn, the morphology affects the overall structural and physical parameters of the surface. In this chapter, a high-performance coating technology is described by thermo-anodizing the surface of aluminium alloy to achieve a coating layer with an emittance of 0.96 and an absorptivity of 0.921. The influences of coating conditions on the solar absorptivity and emittance of coatings have been systematically studied, and an optimized coating condition is concluded at the current density of 5 A/dm^2 and anodizing temperature of 0 ℃. It is found that the anodically formed CTC coatings has good resistance to UV irradiation therefore it can provide a UV shielding effects for the applications in civil and aerospace engineering. By further constructing a hybrid layer by creating a salinization layer to seal the CTC surface, a hybrid hydrophobic coating can be facilitated with anti-icing feature that can delay the frozen of water droplet. We expect this thermo-anodization strategy to advance the coating knowledge and technology for future aerospace engineering.

Chapter 5

Gel impregnated reformable surfaces enabled oil-water separation system

5.1 Introduction

Developing novel and controllable wettability approaches using functional surfaces has attracted significant research interests, with underwater super-oleophobic surfaces being one of the hottest areas with promising applications in microfluidics, oil/water separation, marine antifouling coating, and self-cleaning technology. For example, Jiang's group previously found an interesting phenomenon from fish, where its self-cleaning skin has a multi-length-scale hierarchical structure to enable an outstanding under water oleophobic property and on-demand surface wettability control, thus allowing fish to move freely in the oil-contaminated water[4]. Bio-compatible and stimuli-responsive hydrogel materials can sense the environmental changes with adjustable responses controlled by their compositions and physical properties. Suo et al. demonstrated a hydrogel interferometer with adaptive colouration, providing a facilely tuneable way for broader functionalities[278]. Moreover, hydrogels are consisted of unique hydrophilic groups, whose internal three-dimensional (3D) crosslinked polymer network can absorb and retain large amounts of water molecules, which opens up opportunities for interface/surface structure designs to be applied in aqueous environment. For example, Liu's group used hydrogels to simulate fish scales' surfaces, which can be used in underwater super-oleophobic surface[210]. The conventional approach for oil/water separation is heavily relied on the hydrophilic nature of materials, e.g. using the hydrogel structures for oil/water

separation. However, the surfaces of such structures can be easily contaminated by oil residues, while the fabrication cost is normally high.

In this work, we demonstrate a strategy to achieve a smart hybrid surface by combining 3D printed acrylate-based photopolymer and injected hydrogel embedded microstructures. The surface wetting behaviour is therefore designable and controllable by the synergistic effect of surface groove geometries and the embedded hydrogel patterns. Owing to the reversible swelling of hydrogel, this hybrid surface can be switched between the oleophilic state and the oleophobic state. Successful reversible lipophilic/oleophobic property changes have been demonstrated by controlling the swelling ratios of hydrogel.

5.2 Results and Discussion

5.2.1 Wetting behaviour of contructed oil/groove surface

We firstly characterized the wetting behaviour on plain and smooth surfaces. In open air, the measured contact angles of oil droplets on the 3D printed smooth plain substrate and wet plain hydrogel film were 53° and 21.1°, respectively. Under water, the contact angle of oil droplet on the 3D printed smooth substrate surfaces was 48.9°, whereas on the fully wetted hydrogel film, the contact angle was close to 165° (**Fig. 5.1a**). Therefore, the smooth substrate surface presents a hydrophilic/oleophilic property in the air and under the water, respectively. The contact angles were decreased with the increase of solid surface fraction (**Fig. 5.1b**). On the hybrid surfaces, the surface wetting can be designed by using the changes of surface structures. The fraction of the solid surface area can be calculated by equation (23):

$$f = \frac{W_d}{W_d + W_{gel}} \quad (23)$$

wherein W_d is the groove widths and W_{gel} is the distance/pitch between each groove.

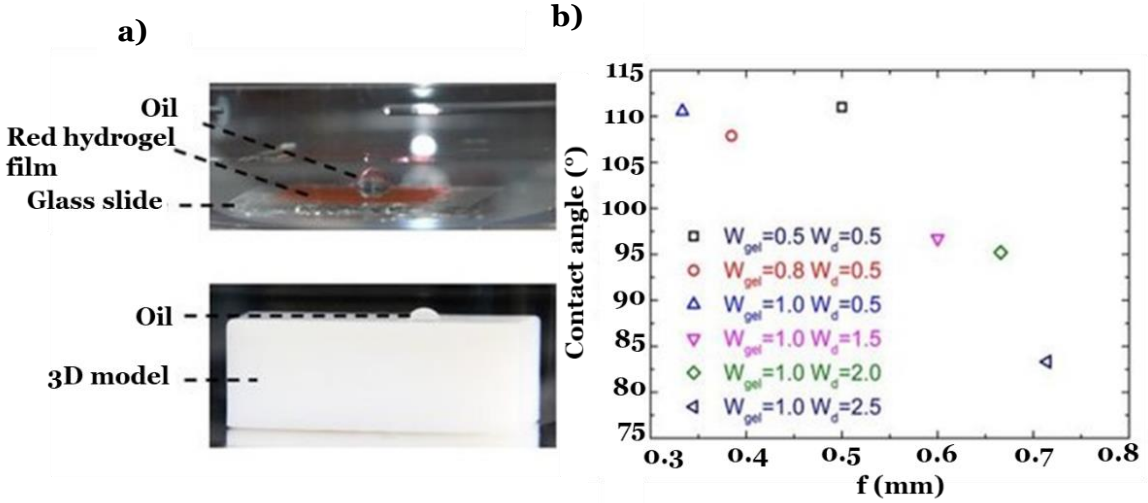

Figure 5.1 a) An oil droplet sits on the hybrid gel impregnated 3D printed surface. **b)** The contact angle summary of oil/hybrid groove surface with in-plane varied surface patterns

5.2.2 Wetting behaviour of structured surfaces after silanization

We then characterized the wetting behaviour of the hybrid surface, at its original "smooth" state without any morphology change. After the hybrid surface being treated with (octadecyl) trimethoxy silane (OTMS), the contact angles of water droplets and oil droplets in the air were found to be larger than 90°, revealing the formation of hydrophobic and oleophobic surfaces. The contact angles of oil droplet and water droplet were gradually decreased over time. After 4 hours, the contact angles were changed from the initial value of 102.6° to 83.4° (**Fig. 5.2 a and b**). The experimental results reveal that the hybrid surface is determined by the hydrophobic and oleophobic

properties of the surface treatment. In addition to the chemical treatment, we also introduced geometric designs in order to generate the functions of changes of surface morphology. Next, the smart surfaces were actuated by immersing the hybrid groove-hydrogel structure in water without other treatment where the swelling hydrogel showed significant changes in the surface morphology (**Fig. 5.2 c**). The smart surfaces underwent a dynamic swelling change, while the gel swelling ratio became stabilized around its maximum value after 120 mins. Experimental results indicate that the hydrogel experienced a two-stage swelling process. In stage-1, the hydrogel was swelled mainly upwards and behaved like a onedimensional swelling. In stage-2, the hydrogel followed a twodimensional swelling until the adjacent gels were contacted and merged with each other, forming a periodic buckling morphology (**Fig. 5.2 d**).

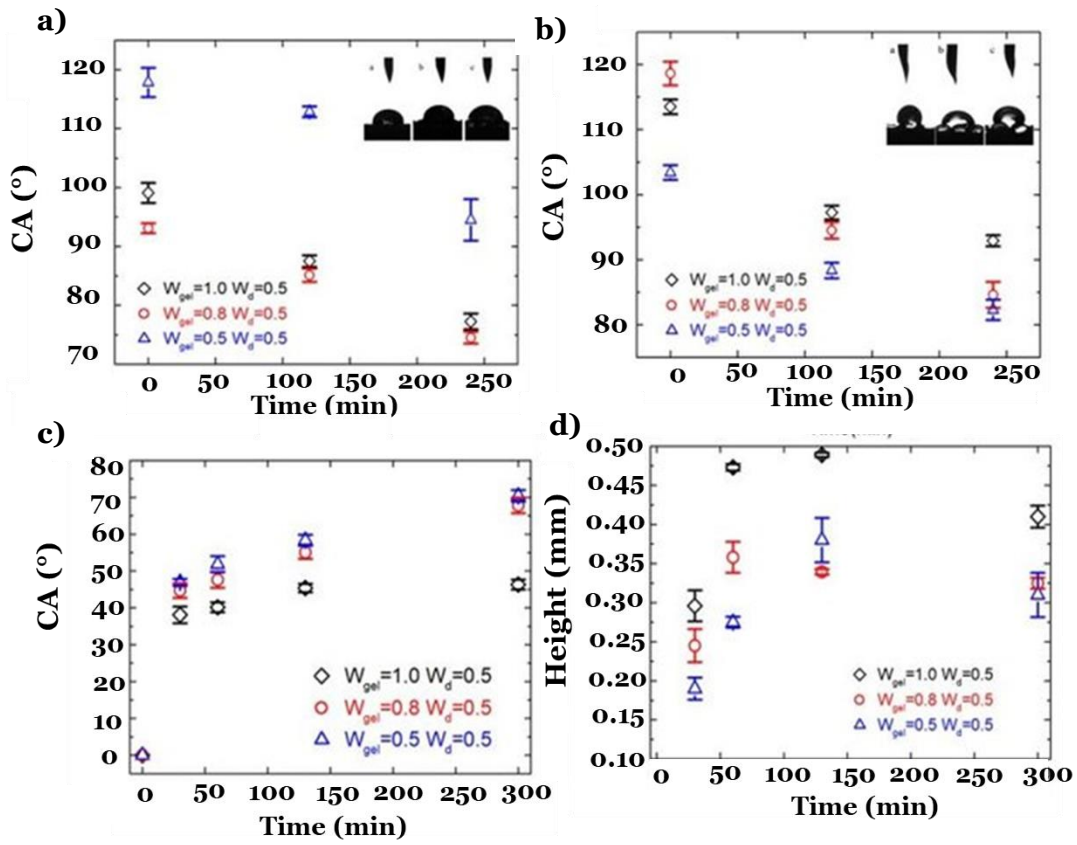

Figure 5.2 a) Oleophobic contact angle after surface treatment. **b)** Hydrophobic contact angle after surface treatment. **c)** The hydrogel without any treatment swelling morphology. **d)** The hydrogel swelling height.

5.2.3 Experimental evidence of reversible morphological swelling

We then studied the oil separation property of the micro-grooved structure patterns by using completely reconfigurable and reversible hydrogel system.In brief, 50 μL oil droplet was dispensed onto the hydrogel surface and the contact angle was measured to start as a reference. By undergoing ionic swelling behaviour within the patterned hydrogel system, the W_d was increased which resulted in a steady decline in the contact angle. When the W_d value was 2.5mm, the contact angle between substrate and oil droplet was maintained 83.2°, which is deemed as oleophilic. For the same groove structure, during reversible morphological swelling, the contact angles between hydrogel and substrate started decreasing until the oil droplet was separated from the 3D substrate as shown in **Figs. 5.3 A1 to 5.3 A4**. Meanwhile, the contact angle between hydrogel and the oil substrate were gradually increased when the hydrogel regained its original shape as shown in **Figs. 5.3 A4 to 5.3 A6**.

Figure 5.3 The experimental observation of reversible morphological change during hydrogel swelling/deswelling, θ is three phase contact angle (3D model, hydrogel and water), scale bar is 2.9mm.

5.3 Conclusion

This chapter reports a novel deisgn philosophy uto study the switchable oil-capture/release behaviour using smart surfaces with hybrid groove-hydrogel structures fabricated by 3D printing and gel injection process. Due to the inherent reversible configurability of the smart hydrogel network, the surface morphology of the structured surface can be tuned in a controllable manner. Through designed experiments, we have studied and evaluated the feasibility of oil-water separation mechanisms from this smart surface by verifying its behaviour using contact angle measurement. During the swelling and merging of hydrogels from the adjacent grooves, the surface was transformed from oleophilic to super-oleophobic and can be switched back to its oleophilic behaviour by deswelling the system.

Chapter 6

Dynamically created gas phase interface over solid surface towards effective energy converter system

6.1 Introduction

Power generation channels are plagued by inefficacies and renounce approximately two-thirds of the immediate energy produced as waste heat[57,58]. A compelling portion of this waste is med-grade heat (generally between 200-400°C) [210], which is both ubiquitous and underutilized. The extraction of this waste heat for energy generation, however, is limited due to complex design, bulky structure, high fabrication cost and insufficient energy conversion capability at lower deformation rate. Most energy converters rely heavily on hard, non-biocompatible electronic control units with reduced soft features which remains constrained by its capabilities. To date, most of energy harvesters, specifically soft adaptable materials are largely adopted in environmentally responsive devices (for example, electronic skin[114], nature mimicking robots[237] etc). Hydrogels are elastic, highly water filled polymer network with wide range of elasticity and tunable hysteresis by effectively modifying the crosslinking density[16]. However, one of the major drawbacks for applications like soft robotics is the thirst for large deformations on the surface to achieve the desired output[225,228]. Despite its drawbacks, one of the easiest solutions for supplying power to soft functional structure is by harvesting naturally viable energy sources such as heat[28], magnetic[229], light[150] etc and making it an excellent candidate

for onboard power source. Reversible stronger crosslinks have been introduced to induce relatively stronger switchable phase with rapid shape fixing at high deformation rate[104]. By contrast, lower deformation behaviour induced functional applications are still in its infancy. This low structural deformation behaviour, in contrast to the above can be used to systematically control the changes in shape and durability of the system with less energy expenditure[41,44]. Compared to the synthetic, these systems have multiple degrees of freedom in their movement and reconfigurable response under defined environmental exposure. Here, we chose novel soft elastically bound systems that can achieve increased power outputs by exploiting multiple shape changes near the contact point via a promising concept called Leidenfrost effect[34,52]. which are seen in different viscous fluids[27], solids[28]. In all the case, the gas-vapor layer acts as a rich source for thermal refuelling aiding in non-contact haphazard motion behaviours along the vapour flow direction due to low friction or increased contact points with the hot surface resulting in increased mass loss and reduced functional output[41]. Recently, a soft solid was inspired to exhibit a new class of Leidenfrost phenomenon wherein, the exiting vapour derived from Leidenfrost phenomenon (ideally dynamic) interacts with the soft system resulting in transfer of thermal energy to elasto-kinetic energy behaving like a fuel-piston model. The elastic solid and the fuel-piston theory[122] have been previously introduced with reduced knowledge about the effect of elasticity and surface temperature condition for dynamic Leidenfrost behaviour with minimum surface energy and maximized recoil nature.

In this chapter, we report a conformable soft waste heat harvesting system inspired from elastic Leidenfrost behaviour that opens new ventures onto capitalizing on nature inspired device fabrications at extremely low cost with

configurability, flexibility even under harsh environments. We also shed light on the initial parameters considered to develop our system that not only provides unique energy harvesting behaviour but also enables an useful energy translation for various power terrains. As a result of such intriguing property, we show fundamental characteristic behaviour of various elastically tuned soft systems and their functionability under range of surface operating temperature environment, their improved bouncing time, with profound output power.

6.2 Results and Discussion

6.2.1 Wettability profile of heated surface

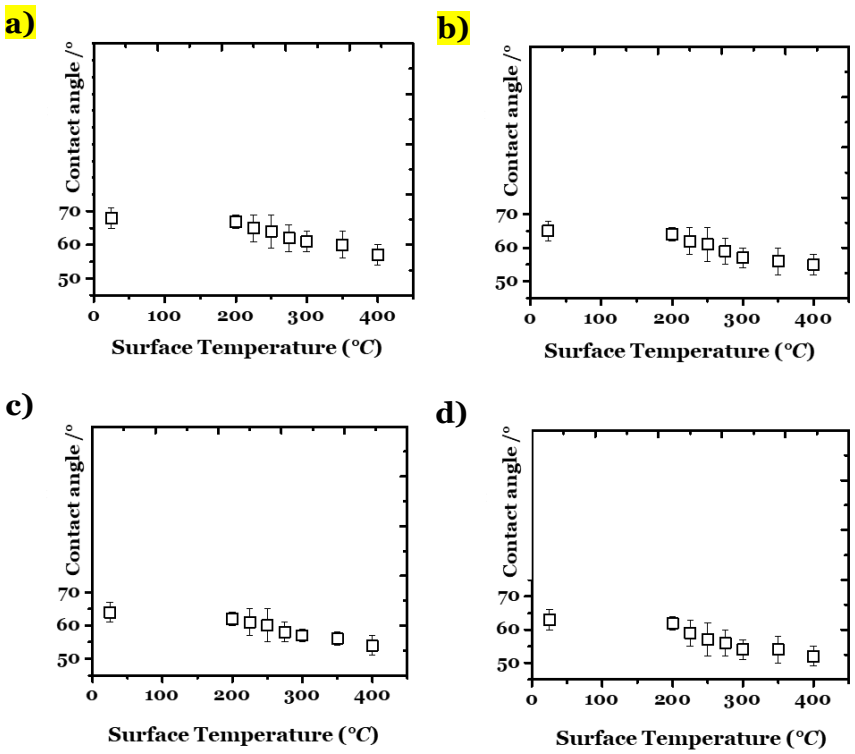

Figure 6.1 Surface contact angle studies after every thermal energy harvesting cycle **a)** n=1; **b)** n=10; **c)** n = 25; **d)** n = 50

As shown in **Figure 6.1**, the surface demonstrates a stable surface contact angle profiles. For testing the dynamic contact profiles, the surface was heated over a range of temperature and the fabricated sphere was bounced onto the heated surface for dictated times. The overall temperature change on the surface is gradual and follows the same trend through-out the experiments.

6.2.2 Mechano-structural properties of the gel spheres

When a water droplet of zero elasticity impacts a low-adhesive Leidenfrost surface, it inherently spreads losing its spherical shape and rebounds translationally with permanent deformation. On the contrary, a water based gel system can overcome the structural complicity via elastic deformation which is controlled by the crosslinking density of the system. To investigate the effect of elasticity on jumping and bouncing behaviour of hydrogel drops, we first created gel spheres of various diameters exhibiting compression modulus as shown in **Fig. 6.2.**

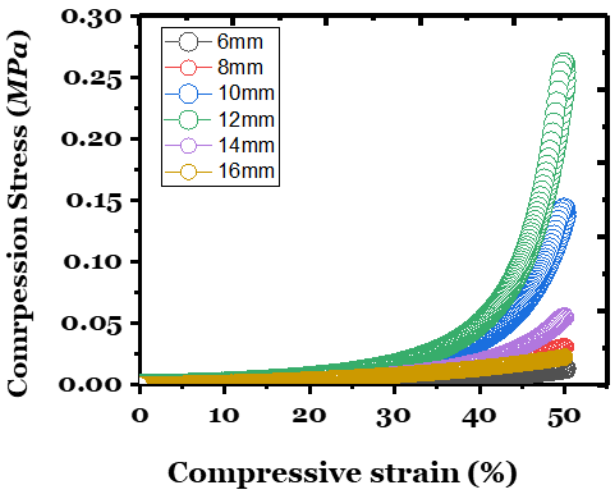

Figure 6.2 Mechanical measurements by compression testing of the elastic gel spheres. The data represents different ball diameters respectively.

With zero elastic water system the evaporation loss increases abruptly from ΔM(change in volume of liquid before and after impact), wherein the impacting droplet nucleates rapidly into a thin lamella until it reaches a broadside of vapour bubbles rupturing the symmetry of the liquid, which is ideally limited by the surface tension or viscosity. However, an elastically tuned water system with specific specimen's stiffness, undergoes an elastic deformation, highlighting the deformation can be reversed based on the specimen's stiffness. These elastic spheres are phase changing material, whose latent heat changes (mass loss) as a function of temperature leading to much stiffer system (**Fig 6.3**).

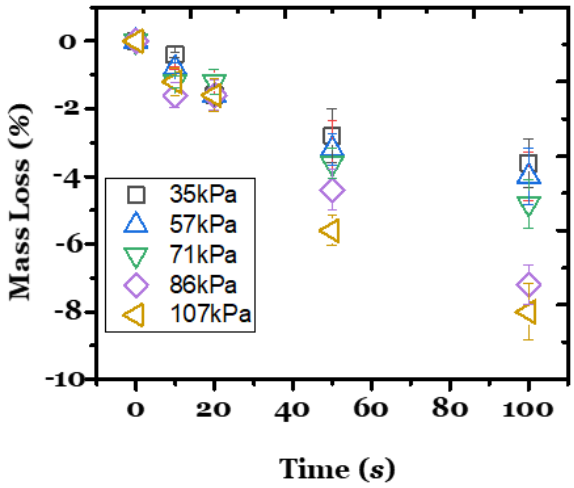

Figure 6.3 Mass loss profile of the bouncing elastic sphere cell for different compression modulus

6.2.3 Thermo-activated elastic bouncing soft spheres

We studied the effect of surface temperature on the dynamic bouncing behaviour of elastically tuned soft spheres under a wide temperature range. With an appropriate Young's moduli and surface temperature, the nature of structural deformation can be controlled as depicted in **Fig 6.4**.

In an ideal bouncing scenario, when an elastic gel is dropped onto a 'cold' (25 °C) surface, the sphere mimicks like an inelastic ball, by losing energy during every impact and eventually dies. Upon exposure to a threshold Leidenfrost temperature (ideally above 200°C), the gel spheres absorb the thermal energy and convert into thermodynamically controlled asymmetric elasto-mechanical vibration of the crosslinking network. Overall, the mechanisms lay over two factors: During the dynamic vapor-sphere interactions, a rapid substantial volume change resulting in a metastable dynamic equilibrium state. The elasticity of the gel sphere acts as a thermal switch which influences the contact point of the gel to under-go three different regimes namely, free convection, stable film boiling and nucleate boiling.

The elastic polymer network provides the opposing force against the sphere spreading which can be seen by analysing the system dynamic at the surface interface. For example, a stiff 105 kPa hydrogel shares similar rebound dynamics to that of the 37kPa gel within the temperature range of 200-300°C which is considered as a Leidenfrost regime. However, as the surface temperature is increased, the capillary adhesion deforms the stiff sphere to form a sticky or no bouncing conditions. For a 37 kPa hydrogel, a different jumping mechanism is observed. Initial jumping by vapor explosion is non-existent below the critical surface temperature and meets the surface leading to pronounced interaction and

rupture on the surface. The existence of rebound behaviour of the elastic spheres indicates that there is a gain in kinetic energy during their interaction with the hot surface which is supported by the elastic nature of the sphere itself.

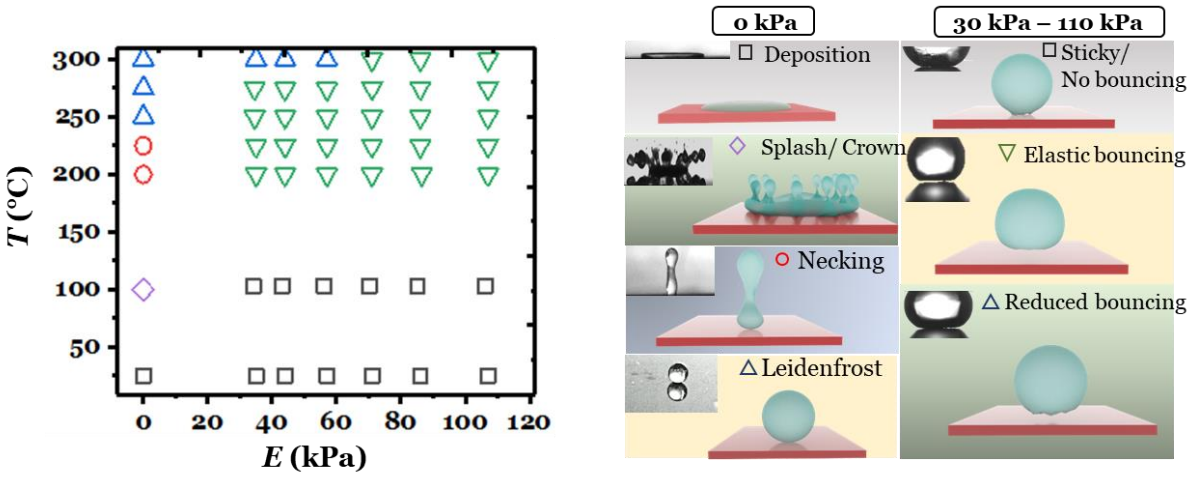

Figure 6.4 Phase diagram comparison of the dynamical regimes on different surface temperature against various Young's moduli

6.2.4 Confinement supported thermo-activated elastic bouncing behaviour of soft spheres

The existence of a rebound behaviour indicates that spheres in the hot experiments harvest thermal energy from the surface and translates into kinetic energy. The kinetic energy is what allows the spheres to bounce in a chaotic manner. Hence, to add value to the injected kinetic energy within the system, a simple tubular confinement was setup and we compared the overall bouncing characteristics of the system. To quantify this, we simply subtracted the maximum height reached during impact onto hot surface from cold rebound height. To ensure the applicability of the system for a potential thermoelectric converter application, we closed the open-top to provide a pronounced bouncing behaviour for the system as illustrated in **Fig. 6.5.** Plotting the bouncing

radiograph for different confinement setup, a steady bouncing height of 3 cm is observed by the gel sphere.

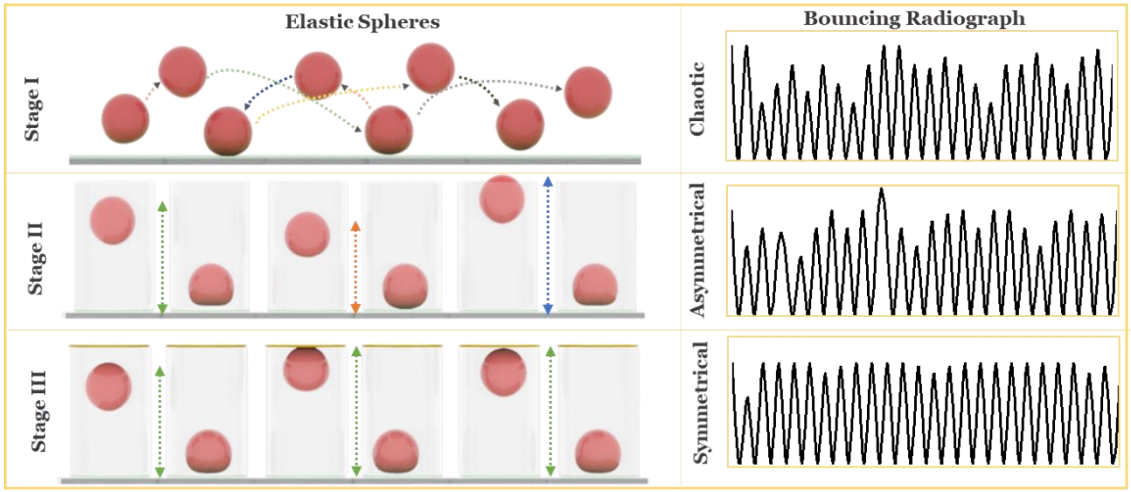

Figure 6.5 A schematic of focused bouncing characteristics of elastically tuned soft sphere under free-state (stage I), roof-less (stage II) and confined (stage III) configurations along with their bouncing radiography

6.2.5 High speed image capture of the thermodynamic work cycles

To understand the jumping mechanism, the underlying hidden physics must be carefully balanced. Previous studies have shown that the ideology of obtaining a carefully balanced Leidenfrost effect can be supported by vaporization, soft elasticity and viscous flow. Liquid systems with zero elasticity makes physical contact with the surface leading to accelerated vaporization rate. Whereas, soft spheres can overcome the nucleation regime by confining the underneath vaporization into potential mechanical energy. This is exhibited by dynamic microscopic working cycles as shown in **Fig 6.6** at the surface-sphere interface that injects kinetic energy by harvesting the invisible heat reservoir. With an appropriate cross-linking density, surface

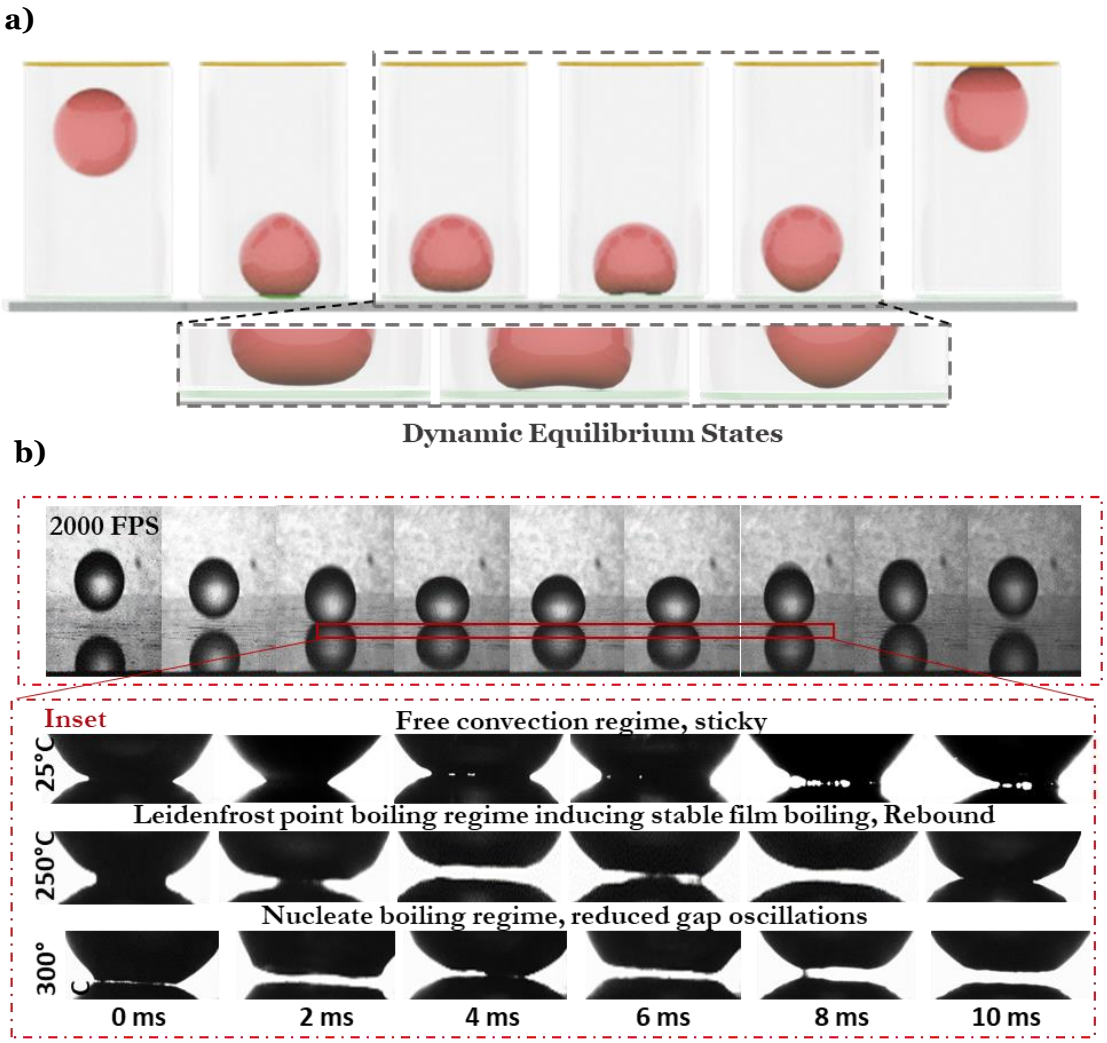

Figure 6.6 a) Representative contactual deformation state of gel sphere upon impact and **b)** real time selected snapshots obtained using high speed camera

temperature and confinement height, the contact area of the sphere impacting the hot substrate reached a local temperature above its glass transition temperature, whereas the other side of the contact area remains as the cold end. The contact region with T>Leidenfrost temperature leads to thermal vibrations within the trapped water pockets inside the crosslinkers leading to asymmetric stretching. The unfolding of self- sustained guided work-cycle is rooted in the invisible vapor layer induced built-in negative feedback loop as shown in **Fig 6.6.** However, at temperatures below Leidenfrost, vapor explosion provides support to dispel the sphere from the surface, however the formation of thin fibrils

inhibits the overall jumping mechanism. With exposure to a threshold Leidenfrost temperature (ideally above 200°C), the gel spheres absorb the thermal energy and converts into elasto-mechanical vibration. By altering the elastic modulus of the impacting gel sphere, we measured the changes in measuring the temporary thermodynamic cycle that fuels the initial uplift of the gel sphere while contacting the surface. As the sphere comes into contact with the surface, the invisible gas-vapor layer increases the contactual pressure which inturn deforms the underbelly of the elastic sphere. The deformation is highly dependent on the thermal energy (fuel) and the elastic energy (decided by the elastic modulus) provides the elastic recoiling towards the substrate leading to successful lift-off. As evident from the **Fig. 6.7**, as the temperature increases, the underbelly deformation increases leading to pronounced capture of the thermal energy and translation into mechanical energy within the system.

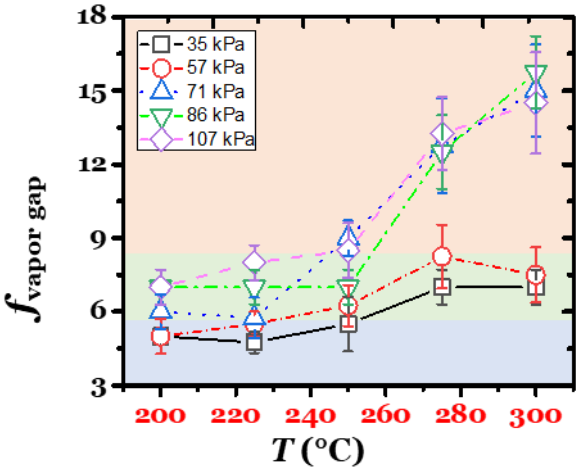

Figure 6.7 Variation in the dynamic gap opening frequency for the system with different water concentration defining the sphere diameter. There is an increase of two folds at temperature above 250°C with increase in elastic modulus

The overall actuation of the cross-linked sphere is dictated by the surface temperature and the number of crosslinkers(elastic modulus) present within the sphere. As evident, the increase in the surface temperature from 250°C increased the gap-oscillation frequency from n(number of gap oscillations)=9 to n=16

which is approximately 200% increase in the amount of energy being consumed during contactual motion behaviour. At lower Leidenfrost temperature, Ts<250°*C* the gap frequency is still present for spheres with elastic modulus ranging from 35 kPa to 110 kPa but with reduced thermal energy consumption which provide more explanation to future studies.

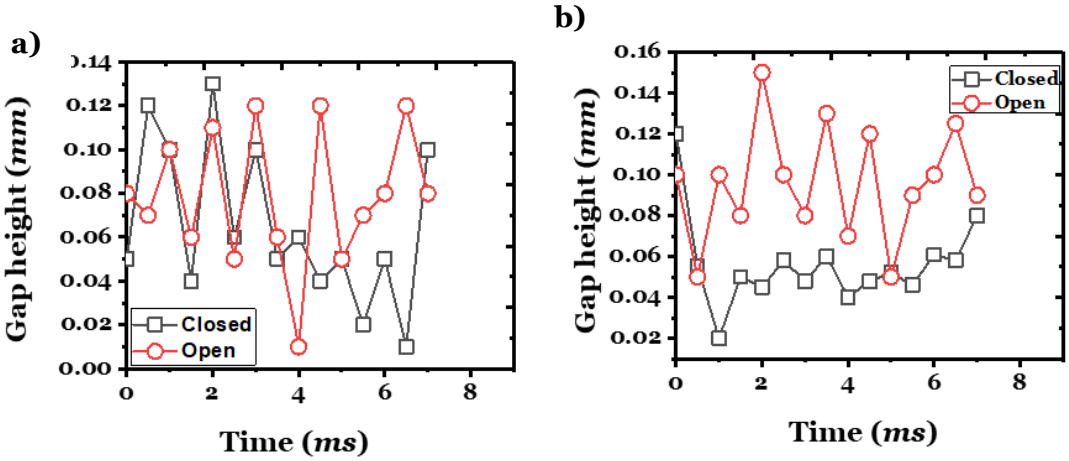

Figure 6.8 Measurement of the vapor layer on a heated surface: Thin vapor layer and growth of its thickness **a)** 250 °C **b)** 300 °C under open and confined conditions

The interfacial gap height of the sphere-vapor was measured after the sphere struck the surface at T_S = 250 °C and T_S = 300 °C under open and confined conditions to understand the variation in the underlying vapor layer thickness (**Fig. 6.8**). We know that the vapor layer should exist when nucleation does not occur, even if surface temperature is high enough. An approximate measurement of the vapor layer could shed light on the effect of surface temperature on the oscillation behaviour of the soft sphere and possibly a relation can be drawn between the surface thermal energy and elastic energy. At a high T_S such as 300°C under confined conditions resulted in a lower gap height which could be due to to an imbalance between vapor generation and escape. Initially at T_S = 250°C, the vapor layer generated under both open and closed conditions through

thermal conduction can sufficiently escape from the center to the edge of the drop resulting in increased vapor layer thickness with formation of vapor dome. However, over time, an increase in the vapor layer thickness allows for increase in the amount of vapor that can escape, so the imbalance between vapor generation and escape could be pronounced to provide uplifting rather than floating on the surface. An ideal thickness of the vapor layer/ gap height will be difficult to distinguish due to the continuous oscillating motion occurring at the solid-vapor interface as evidenced in **Fig. 6.6**.

6.2.6 Effect of Elasticity on the Bouncing time, Incoming Velocity, Restitution Coefficient, and Energy Injection

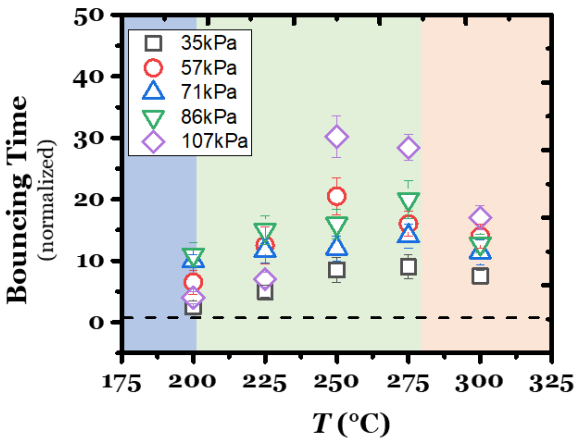

Figure 6.9 Normalized bouncing time against surface temperature for various elastic systems

As evident from our previous demonstration, there is an opposing force that restores the elastic energy of the soft gel under confinement. The bouncing time of the soft system can be completely scaled up by tuning the inner elasticity as shown in **Fig. 6.9**. For a stiff 105kPa hydrogel, we find that the initial jumping mechanism is like that of the 30 kPa gel at temperature ~200°C. However, the initial jump by vapor explosion is observed only on ~50% of the spheres. The presence of extremely low water content within the system cannot deform the stiff

drop, rather falls like an in-elastic sphere which keeps it spherical. This limits the soft system's ability to capture and confine an invisible gas-vapor layer allowing the bubbles to escape and release energy on the side. By observing the fall speed of the sphere as a function of different diameters at 250 °C, we find that indeed the outgoing velocity becomes higher than the incoming without monotonously moving upward as the elastic nature of the soft sphere is increased; which is caused by the elasto-capillary waves (**Fig. 6.10**).

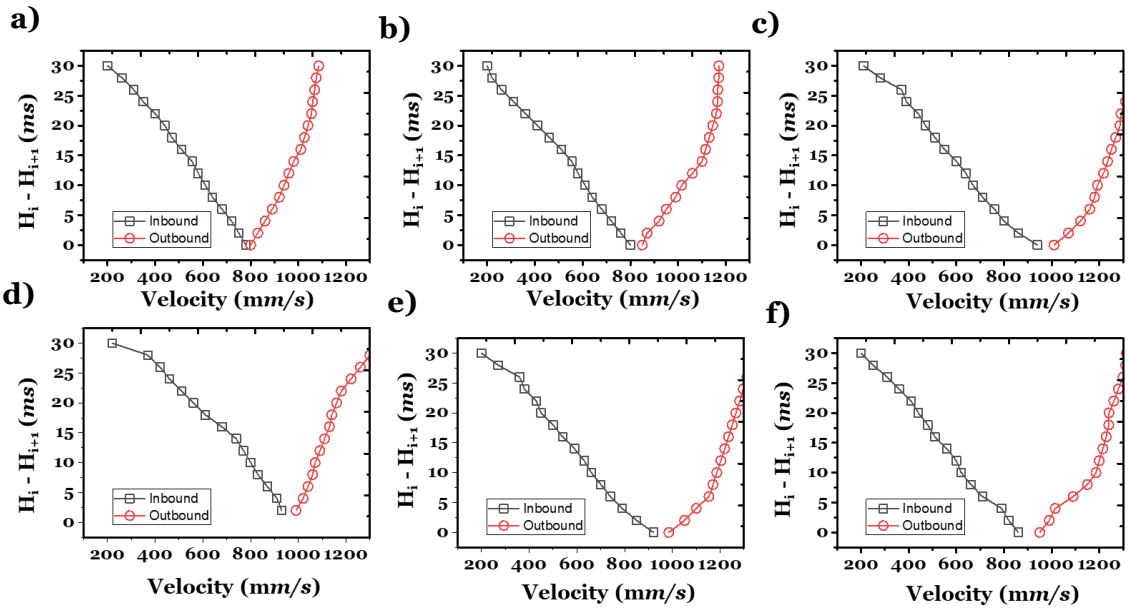

Figure 6.10 Inbound and outbound velocity of different elastic gel spheres diameters (B_d) during impact **a)** 35kPa; **b)** 57 kPa; **c)** 71 kPa; **d)** 86 kPa; **e)** 107 kPa under confined bouncing condition at Ts=250°c.

Interestingly, a similar measurement on the gap oscillations at the contact point revealed a pressure-pulse impact with waves moving through the sphere (**Fig. 6.8**). While it is clear that capillary waves strictly limits the outgoing velocity. trampolining consistently occurs in the Leidenfrost regime, we are not able to strictly limit trampolining to temperatures above the Leidenfrost temperature. Trampolining likely occurs for the pressure-pulse bouncing regime when the initial jump height is less than a few mm. An ideal energy conversion mechanism

should have two principles: thermal to elastic energy in the contact surface and elastic to kinetic within the system. If tailored correctly, the gap heights and gap frequency can be designed such that the two fundamental energy conversion mechanism have disparate timescales, allowing for faster vertical momentum transfer from thermal to kinetic energy within the system and thus allowing early lift-off of the gel sphere from the surface to reduce overall vaporization rate and increased bouncing lifetime.

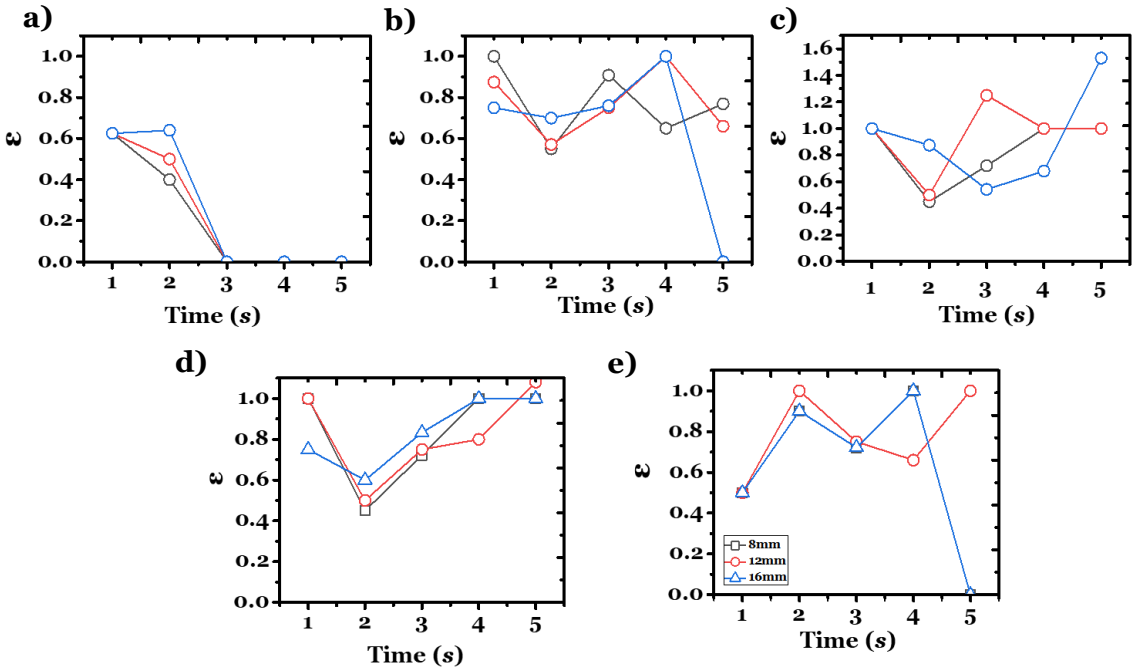

Figure 6.11 Coefficient of restitution profile for different elastic sphere sizes under various surface temperature conditions **a)** 25°c; **b)** 200°c; **c)** 250°c; **d)** 300°c; **e)** 350°c

In this case, we found that the rate of thermal switch dictates the bouncing duration of the gel spheres which inturn is dependent on the crosslinking density/water content. However, as the elasticity is increased, the bouncing time decreases gradually due to reduction in the water content within the system. Also termed as drainage time, the bouncing time depends not only on the properties (density, viscosity, surface tension, and rheology) of fluid system but on temperature, vapor concentration, solubility of the interstitial gas as well. To

account for the rapid attenuation of the thermal vibrations within the elastic system, we confirmed that increased bouncing heights are not due to loss in mass by plotting the coefficient of restitution($\varepsilon = \frac{v_a}{v_b}$, where v_b and v_a are the velocities of before and after the impact) to explore whether the bouncing is due to viscous-dominant or elastic-dominant nature (**Fig 6.11**). For this classification, we found elastic spheres with low elastic modulus (<35kPa) showing ε < 0.8 below a certain temperature and on the other hand, ε is mostly above 0.8 for the same system as the temperature is increased from 200°C which could be due to increase in air pressure within the system. As the gel sphere is heated, it becomes more elastic and the bonds tends to move freely leading to increased energy injection within the system. This becomes more evident when the spheres are dropped at different velocities, wherein, the coefficient of restitution remains above 1 at lower impact speeds and recommended Leidenfrost temperature. As, impact speed is increased there might chances of intermediate contactual behaviour with the hot surface that can increase the vaporization rate of the soft spheres (**Fig 6.12**).

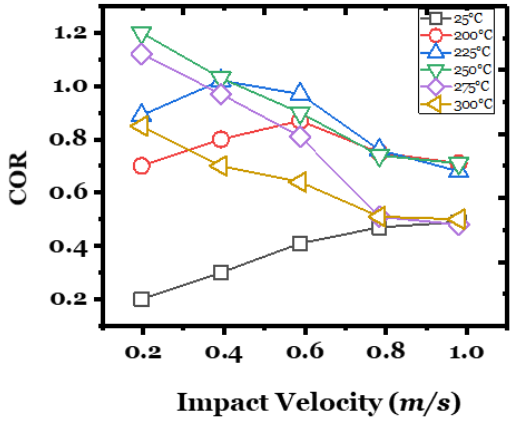

Figure 6.12 Coefficient of restitution profile of the optimum sphere size under different impact velocity on various surface temperatures

The shock wave provided at the vapor-solid interface provides the necessary elasto-kinetic energy (**Fig 6.13**) which is predetermined by the energy being dissipated via elastic deformation of the system. We also calculated the total amount of energy being injected into the system by dropping the gel spheres at variable drop heights to understand the total energy being gained by the system. In general,

$$\frac{E_D}{E_{Impact}} = 1 - \frac{H_{max}}{H} \tag{24}$$

Wherein, $\frac{E_D}{E_{Impact}}$ = total energy dissipation, H_{max} = maximum bouncing height, H = initial potential energy. Nearly 90% of the energy is being transferred from the surface into the soft sphere in the form of elasto-mechanical energy, however, the remaining energy is dissipated via screeching, vaporization and elastic deformation.

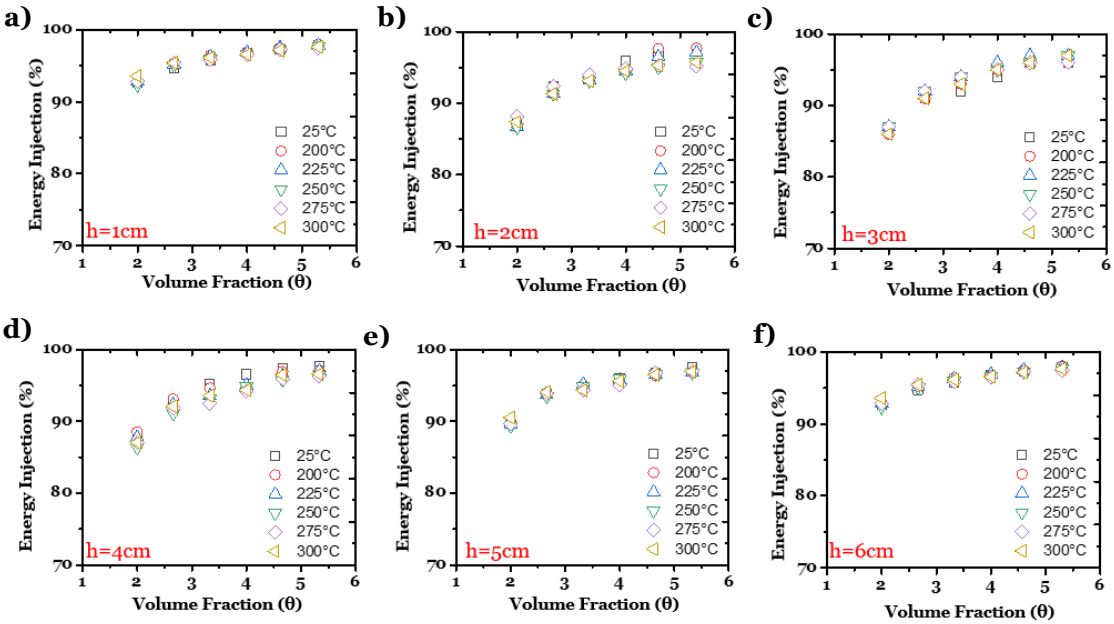

Figure 6.13 Energy dissipation during impact and rebound as a function of the dimensionless group volume fraction (θ) under different drop heights

6.2.7 Effect of Elasticity on the Contact time, Impact Force and Deformation Radius

An ideal energy conversion mechanism should have two principles: thermal to elastic energy in the contact surface and elastic to kinetic within the system. If tailored correctly, the gap heights and gap frequency can be designed such that the two fundamental energy conversion mechanism have disparate timescales, allowing for faster vertical momentum transfer from thermal to kinetic energy within the system and thus allowing early lift-off of the gel sphere from the surface to reduce overall vaporization rate and increased bouncing lifetime. The contact time is different from that of a solid sphere because for a water drop, kinetic energy is transformed into surface tension across the entire drop, as opposed to the localized elastic energy of a solid sphere.

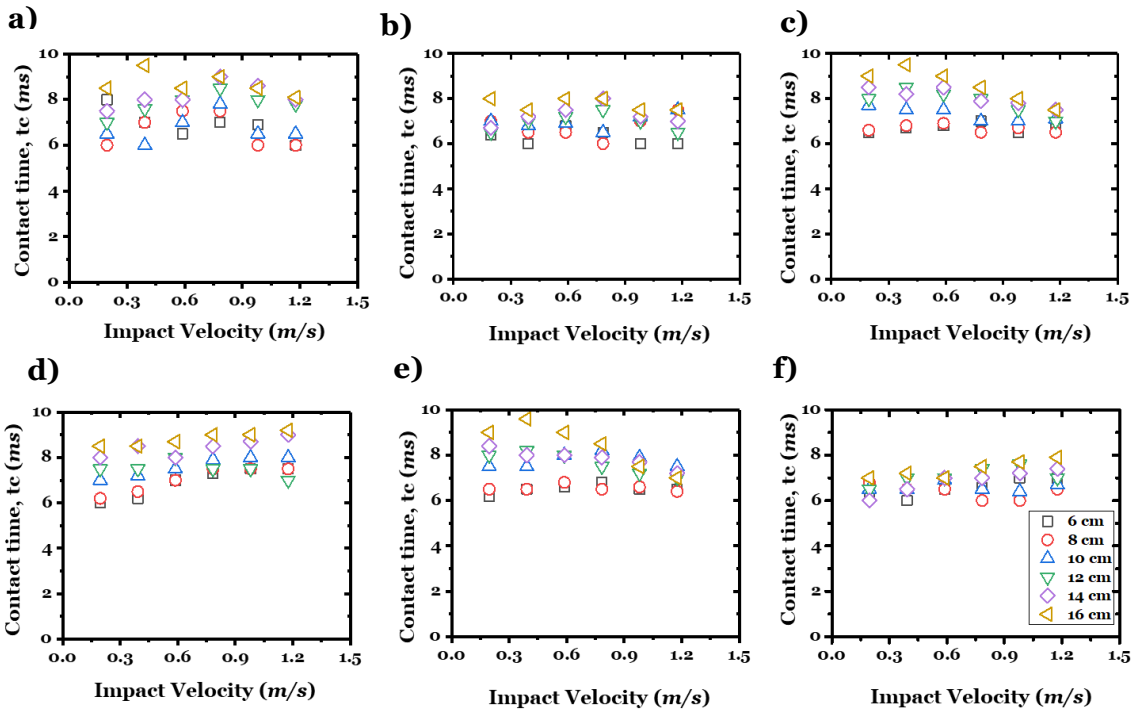

Figure 6.14 Maximum contact time, t_c, as a function of impact speed on cold and hot regimes for different drop heights **a)** T=200°C; **b)** T=225°C; **c)** T=250°C; **d)** T=275°C; **e)** T=300°C

The time spent by the elastic sphere at the surface was calculated using

$$t_c = 3(\frac{M}{k_1})^{\frac{2}{5}} (\frac{g}{H})^{\frac{-1}{2020}} \quad (25)$$

wherein, t_c is the contact time, M is the sphere mass, k_1 spring constant, H drop height. In order to systematically study the effect of substrate temperature on contact times, we conducted gel sphere impact experiments with varying ball Young's modulus (35 kPa< E <110 kPa), surface temperature (25 °C< T_s <300 °C), as well as varying the volume fraction (2< Φ <6) and impact speed (0.2 m/s< v <1.2 m/s). **Figure 6.14** summarizes the contact times for gel sphere impact on surface with T_s=250°C and impact speeds play a major role in controlling the gel sphere contact time to avoid forming physical contact. For our case, the contact is roughly a point contact wherein the elasticity of the system prevents edgewise spreading of the hydrogel and thereby the pressure developed at contact point is transmitted as a shock wave propagating through the sphere leading to shorter contact times. The gel sphere (E=110 kPa) exhibited increased contact time at surface temperature (200 °C – 275 °C) which could explain the formation of thin fibrillary contact points accelerating the rate of evaporation and bouncing efficiency. The burning of the fibrillary contact points could also define the introduction of screeching noises that arises while the gel sphere contacts the hot surface.

We can clearly expand the impact force behaviour by comparing the drop height against different ball diameters of increasing Young's modulus. **Fig 6.15** briefly portrays the impact force achieved during the experiment and plotted against the theoretically predicted values. The impact force was calculated by

$$F(N) = k_1^{0.4}(2.5\ X\ M\ X\ 9.9\ X\ H_i)^{0.6} \quad (26)$$

Wherein, k_1 spring constant, H drop height, M sphere mass. We have also showcased how the impact force varies with different ball diameters of varied Young's modulus dropped at different heights. In brief, keeping Young's modulus constant, increasing the ball diameter (B_d) increases the impact force with the magnitude of 10. Upon comparing the impact force for a specific ball diameter (B_d=12mm), we found the increasing in drop height only increased impact force, however, the contact time remains undisturbed.

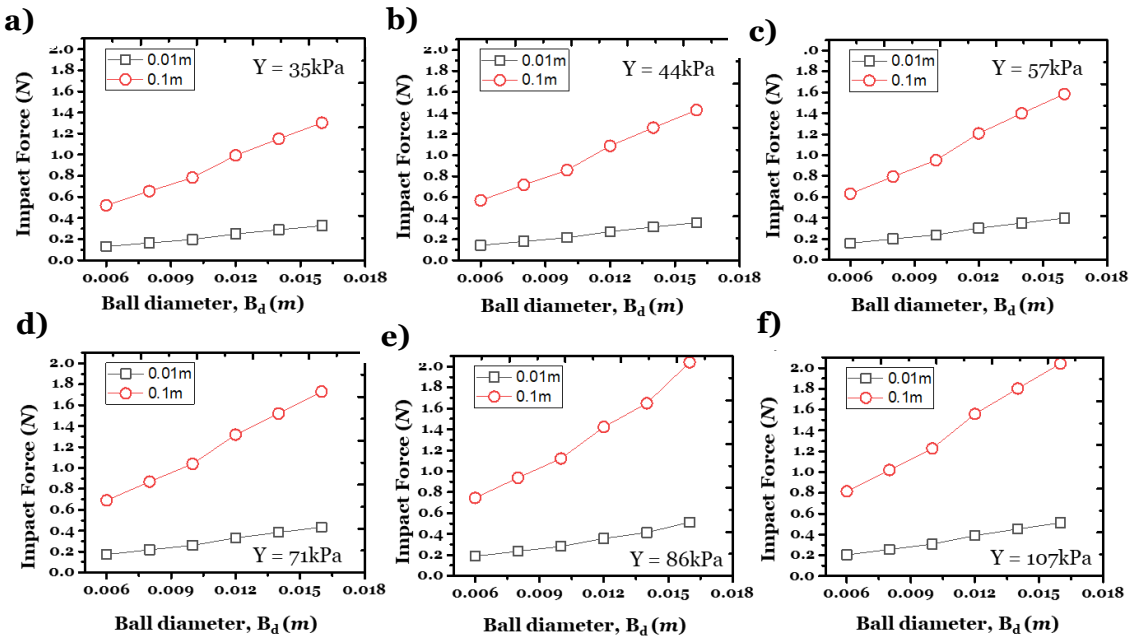

Figure 6.15 The variations of the impact force as a function of different ball diameter with different Young's modulus under two extreme drop heights.

Fig 6.15 also confirms the ideology that increasing the ball diameter and changing the drop height between 1 cm and 10 cm increases the impact force upto 10 times. To the best of our understanding, we could explain the haphazard behaviour of the gap heights at various impact force by looking closely at the contact behaviour of the elastic gel sphere (**Fig 6.16**). For impact force <0.3N, the incoming velocity of the gel sphere was found to be minimum which leads to sticky or direct contact behaviour. Impact force between 0.3N to 0.6N, a film contact behaviour is achieved which provides stable film boiling regime for the

system leading to successful rebound. However, at values above 0.6N, a filament contact regime is seen which exhibits fibrillary bridges that burns away leading to decreased device performance. To achieve a dynamic elastic or super elastic rebound behaviour of the gel system (ε>0.9), variation of the bouncing outputs with temperature shows three regimes: (i) at lower temperatures (<250°C), the outgoing velocity is found to be higher for lower ball diameters and (ii) at high temperatures (>250°C), the Young's moduli of the system comes to play which determines the amount of water present inside the system. Both temperature region demonstrate bouncing behaviour but the transition between inelastic to elastic bouncing occurs at different temperatures for different elastic entities; the substrate with low temperature provides low surface energy for Young's modulus more than 57kPa with B_d=12mm at an optimum drop height of 3 cm.

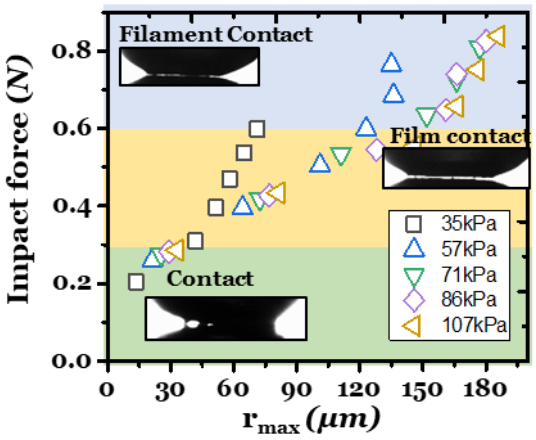

Figure 6.16 Influence on the contactual behaviour (inset) of the elastic sphere due to the impact force and resulting deformation radius

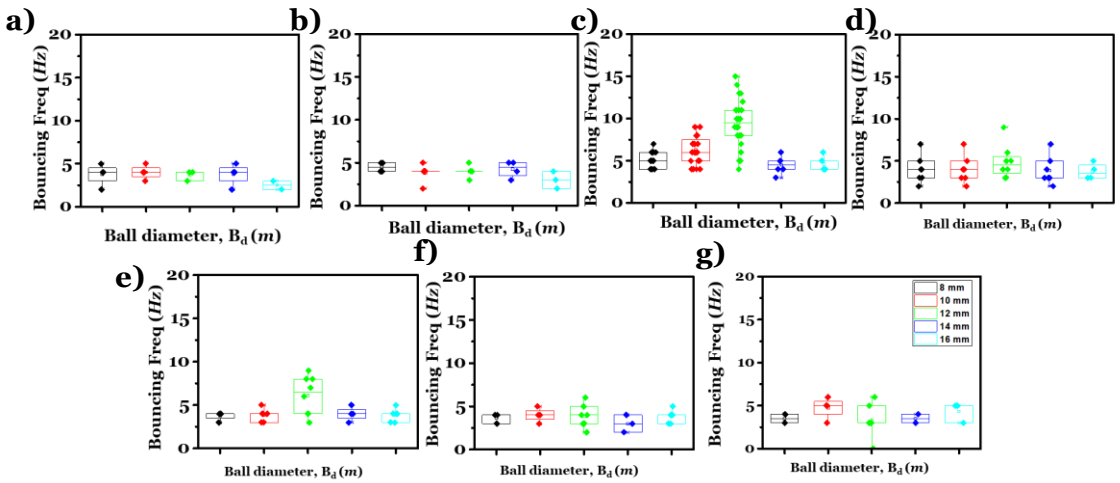

Figure 6.17 Comparison of bouncing frequency for various elastic gel sphere diameter under different surface temperature conditions **a)** 200°C; **b)** 225°C; **c)** 250°C; **d)** 275°C; **e)** 300°C; **f)** 325°C; **g)** 350°C. The bouncing frequency is found to be higher at 250°C but varies among different sphere diameter. However, increasing the surface temperature to 275°C provides optimum pulsed bouncing frequency for varied gel sphere diameters.

6.2.8 Electricity generation of the soft thermoelectric energy converter

To allow the efficient conversion of thermo induced mechano-kinetic energy, we studied the influence of confinement height on the overall work-cycle process. By confining it at various heights (**Fig 6.17**), we found that the thermodynamic work-cycle of the system can be enhanced at surface temperature of 250°C (n=15 per second) compared to 200°C (n=7 per second) which led to increased power output in one second. As we lower the tube size, there is an increase in the bouncing frequency but ultimately leads to reduced life expectancy. As evident from earlier studies on droplet behaviour on hot surface, the overall water saturation temperature is shifted to a higher side to accommodate directional transport with changes in atmospheric pressure which could lead to increase in latent heat vaporization rate.

A Quad-setup multiresonant gel sphere thermoelectric system working at Leidenfrost temperatures have been developed for the application of harvesting heat from natural sources. The structure of the device is schematically depicted in **Fig 6.18**. The silicon surface serves as heat conduction substrate with piezobuzzers attached onto a 3D printed holder on the top. The silicon substrate provides the necessary gas vapour layer for Leidenfrost behaviour to be activated as smoothness also dictates the fate of dynamic Leidenfrost effect.

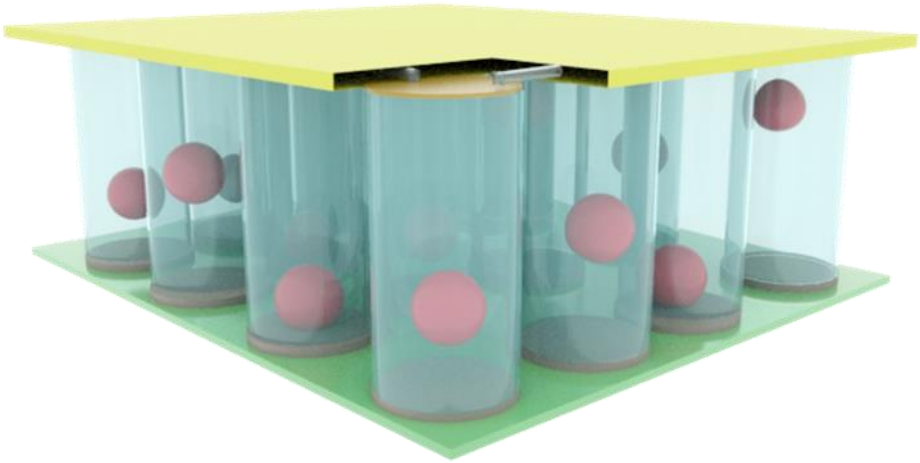

Figure 6.18 Schematic illustration of our integrated thermo-electric converter

The thermally actuating gel sphere scavenges the thermal energy, especially the energy of hot substrate with temperature more than 200°C delivering a novel low pressure thermo-kinetic up conversion propels the soft engine with increased velocity to reach a maximum height and hits the piezobuzzer thereby translating the kinetic energy into electrical energy via deformation of the buzzers. Because ambient conditions are complex and in a tightly closed system increase in pressure could lead to increase in evaporation of the hydrogel spheres.

Figure 6.19a shows the voltage generation test results when a single harvester is tested under different tubular confinements. In general, the tube sizes were varied between 2, 3 and 4 cm height and the gel sphere was dropped.

At surface temperature of T_s = 250°C, the open circuit output voltage measured from 3 different tube heights, and came out to be 4.1V, 3.2V and 2.2V approximately. Irrespective of higher output voltage capacity observed from 2 cm tube height, the overall life expectancy of the device was further downgraded due to vaporization effect.

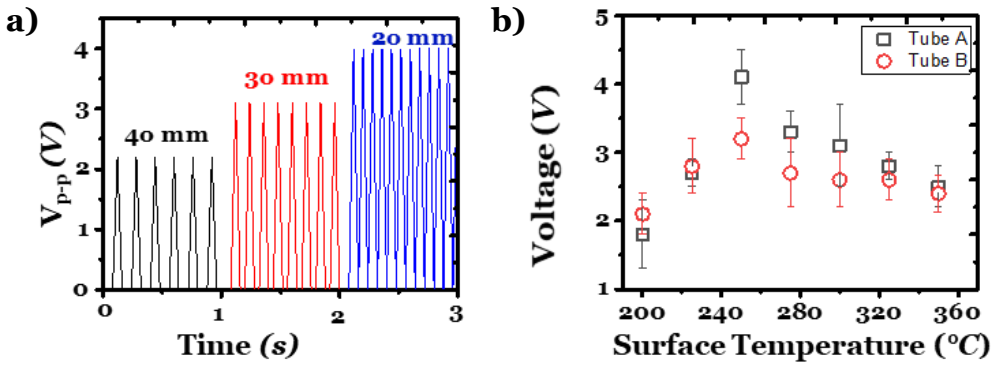

Figure 6.19 a) Comparison of the voltage of energy harvester under different tubular confinement; **b)** Effect of surface temperature on the output voltage at two different tubular confinements of varying heights, tube A (3 cm) and tube B (4 cm)

Figure 6.19b shows the impact of surface temperature on the voltage generation under tubular confinement. As the surface temperature is raised, the gel spheres can harvest enough thermal energy not pertaining to deteriorate its structural disintegration. As the surface temperature is increased to the Leidenfrost limit (T_s = 250°C), there is a steep increase in voltage and declines as the threshold temperature is crossed irrespective of tube A (3 cm) and tube B (4 cm). The overall output voltage increased to a maximum of 4V at Ts = 250 °C and declined gradually to 2.5 V which is due to the specific material attributes and their contactual behaviour at the surface-vapor interface under elevated temperatures.

Note that the energy harvesting system which are soft, biocompatible, are capable of undergoing material tunability to different shape and structural properties which represents a novel standard in soft robot inspired thermal energy harvester. Our quad-setup multiresonant thermoelectric gel spheres can light up 7 light-emitting diodes (LEDs) connected in series directly (**Fig 6.20**).

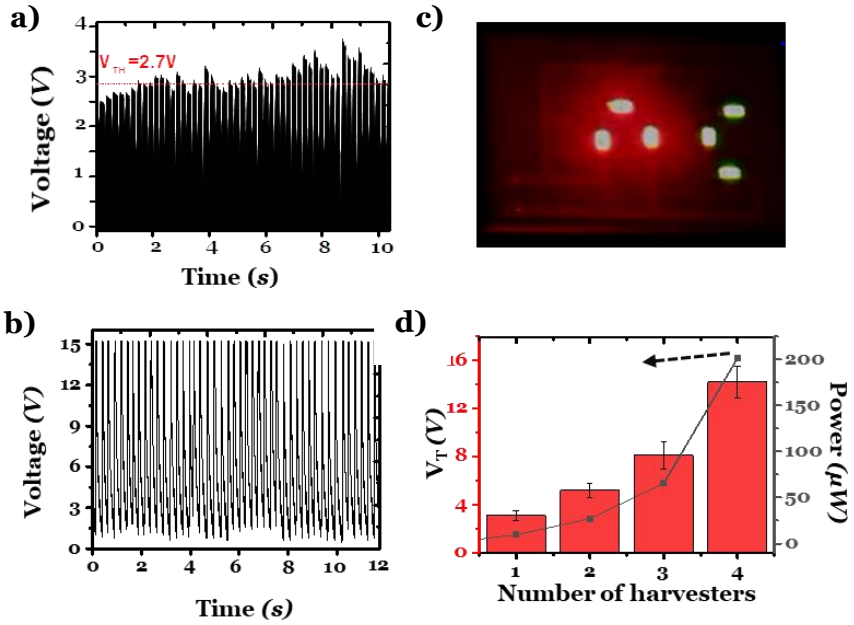

Figure 6.20 **a)** Voltage generated running across LED using a single gel-system at surface temperature of 250°C, **b)** Voltage output of quadruple energy harvester; **c)** Photograph showing the powering of NC Logo using Quadro energy harvester at a surface temperature of 250°C respectively **d)** Generated peak power (solid black symbols) and peak voltage (bar) versus number of energy harvesting units comparison profile of power output with different number of energy harvester showing the scalability of the power by connecting multiple identical units in series .

A steady amount of potential is provided across the LED for pulsed power supply (**Fig 6.20a**) and can easily be converted into continuous feed with the help of an external capacitor. By connecting four identical soft engines, we find that the device can provide an output voltage of 16 V which can be tuned to achieve

constant power supply. and a quadro-setup energy harvester the total output can be tailoring to number of such pocket systems to deliver an amplified output voltage signal (**Fig 6.20b**). If the letter shaped NC was further cut into two independent letter buttons, each of these buttons can be individually light up using the Quadro converter unit (**Fig 6.20c**). In additional experiments (**Fig 6.20d**), we noticed a strong proliferation in the overall power output of the system by a factor of 5 while integrating systems from single to quad-mode.

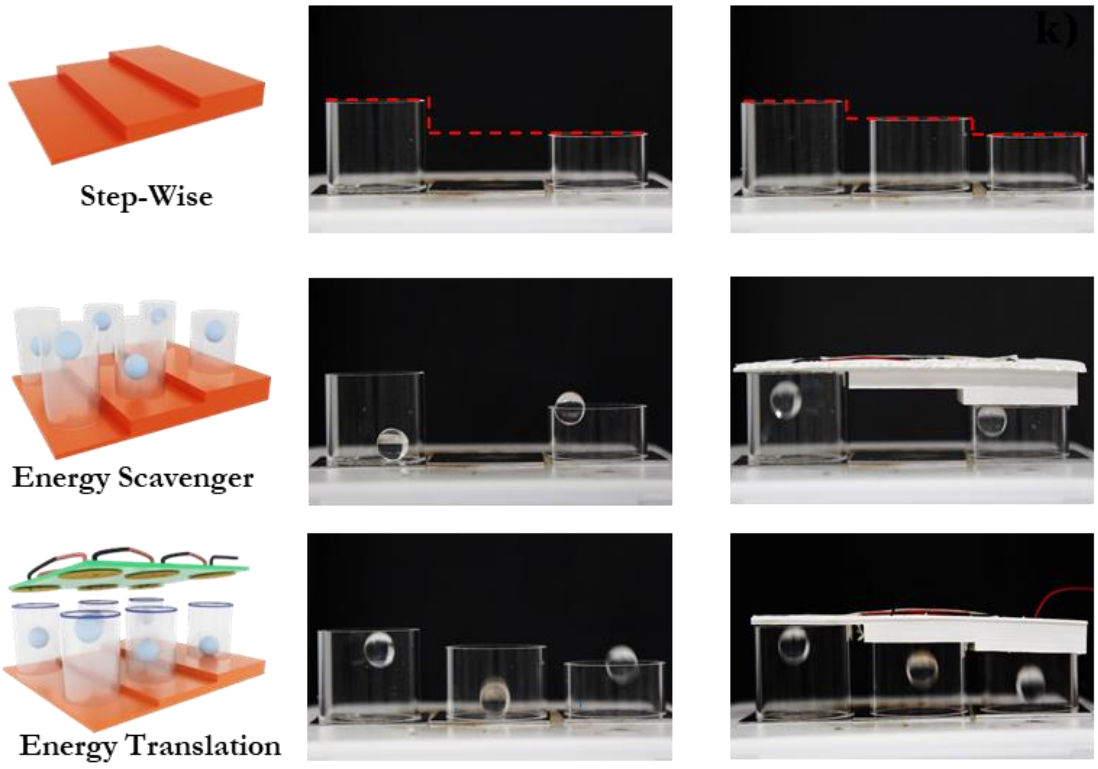

Figure 6.21 Photographs of structurally conformable phase optimized bouncing spheres under different tubular confinement on a heated surface.

The enhanced stability and robustness inherited by the soft thermoelectric harvester can be extended to various conformable surface to impart wider functionalities in extreme environmental conditions. As a proof of concept demonstration, we fabricated ladder like surfaces (**Fig. 6.21**) on a flexible steel surface. Briefly, we first 3D printed the top lid which provides structural functionalities to the device by allowing the total optimum to be about 3 cm (optimum bouncing height). Under a bending state/ curved surface (**Fig. 6.22**), the device still functions until a threshold curved limit is achieved on the surface, which is comparable to that on the structured surface. Moreover, we also scaled the amount of kinetic energy being converted to electrical output by balancing the impact regime of the sphere at the hot surface and piezocrystal as follows:

$$\frac{1}{2}mu^2 - \frac{1}{2}mu_o^2 \sim F\tau \sim mg\tau \qquad (27)$$

Wherein, m is the mass of the ball, τ is the contact time, u^2 is the final velocity and u_o^2 is the initial velocity of the ball, F is the force exerted on the piezo-disc.

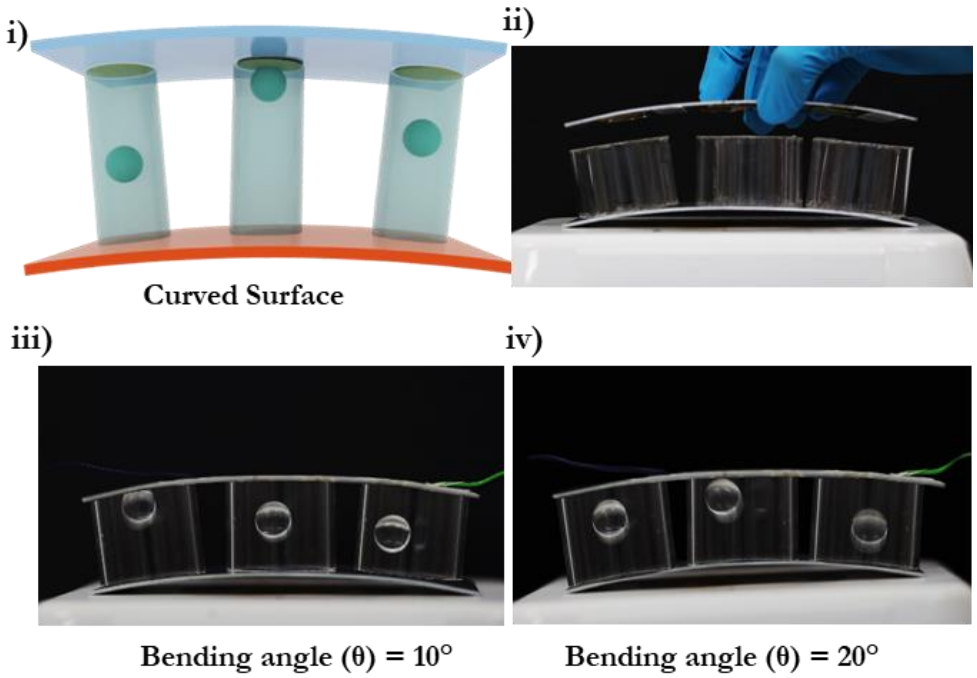

Figure 6.22 Real-time snapshots of energy harvester on different curved surface. structurally conformable phase optimized bouncing behaviour under different tubular confinement.

Fig 6.23 shows the linear relationship between the ratio of electrical output and the fraction of kinetic energy created within the soft system after harvesting the underlying thermal energy. The adaptability of the bouncing behaviour to different conformable structural surfaces makes it possible to open new avenue for the rational design of novel energy devices that are capable of scavenging abundant heat sources with long term stability and durability via material and surface chemistry.

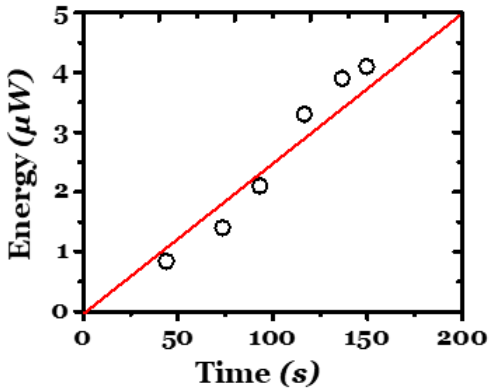

Figure 6.23 Energy output dependence versus contact time of the elastic gel sphere on a hot surface derived using a simple scaling law.

6.3 Conclusion

In summary, we report the design of a novel soft- Leidenfrost inspired thermoelectric converter, which exhibits many new venture into utilizing naturally abundant waste heat by configurability, autonomous, flexibility, and power generation stability, in a wide range of working environments. Unexpectedly, inspiration from material chemistry can pronounce the overall bouncing efficiency of the soft sphere for a longer duration with reduced contact time to avoid increased vaporization rate. Moreover, we show that there exists a critical confinement height to support increased work-cycles, at which the

conversion of thermal energy into useful electrical energy is enhanced. The formation of different structural gestures at the vapor-solid interface governs the overall system efficiency. Such an intriguing efficiency parameter can be altered by playing the soft sphere's elasticity, sphere's surface functionality, functional surface textures, etc though the fundamental mechanism remains to be elucidated. The lego-shaped re-configuration of individual energy scavenger/translation units can avoid the limitation of scaling up for wider surface temperatures. We envision that the marriage of these two seemingly totally different arenas (Leidenfrost and soft system) provides a paradigm shift in the nature inspired physics for robust and versatile energy devices that can be used as a clean and longer lifetime alternative in various working environments which are rich in geothermal resources, waste heat conversion in household gadgets, spaceships, etc.

Chapter 7

Cooperative Wetting Promoted Heterogenous Structured Morphing transducers

7.1 Introduction

One of the desirable developments is to make the morphing process programmable[276] and reversible[277] through structured soft functional materials, which enable effective shape configuration design according to the applications. As one of the popular candidates, hydrogels have drawn more significant attentions due to their open network structures, and ability to generate large changes (therefore high deformation) in volume responding to various external stimulation. The through-thickness gradient approach typically employs a hydrogel bilayer structure where the swelling behaviour remains dissimilar across the thickness[278]. The differential swelling leads to internal stress mismatch and influences out-of-plane 3D morphing configurations, resulting in a single configuration at certain external conditions (e.g., temperature, ion concentration)[279]. When external conditions are altered, a wider range of deformation magnitude and/or a reversed shape (e.g., bending towards opposite direction, "C" becomes"Ↄ")can be achieved, and more complicated configurations can be accomplished via advanced 2D shape patterning. On the other hand, the in-plane gradient approach typically employs 2D heterogeneity via a single layer of patterned functional hydrogel on the same plane, resulting in a bistable status where the buckling could happen in either directions. Combining the ideas from

both through-thickness and in-plane gradient modes, through a controlled "preswelling" process that determines swelling direction, programmable complex deformations were demonstrated by the "site-specific" patterned hydrogel blocks. The resultant shape-morphing structure generated due to in-plane elastic mismatch between nonswelling substrate and controlled swellable gel blocks was more or less fixed. Inspired by natural biostructures, a single layer of encoded heterogeneous hydrogel building blocks has been exploited to form hierarchical complex hydrogel architectures, using droplet microfluidics (DMF) surface wetting control to guide the gel formation. We hereby propose a facile approach to achieve not only programmable, but also reconfigurable maskless swelling/ deswelling morphing structures that change shapes between various cooperative states responding to ionic strength.

7.2 Results

7.2.1 Hierarchical patterned gel configuration

The hierarchical patterned gels are prepared by two-step polymerization method, as shown in **Fig. 7.1**. A thin film nonfunctional substrate is polymerized to form polyacrylamide (PAAm) gels without the presence of sodium acrylate (SA). PAAm exhibits good biosafety characteristics towards human cells, which makes it a popular candidate in smart biomedical applications[33]. Alongside the nonfunctional substrate fabrication, a series of patterns made of different concentrations of SA containing PAAm mixtures was dispensed onto the precoated hydrophilic/hydrophobic template forming the functional blocks. The functional polymer droplets were allowed to cross-link with the prefabricated thin-film substrate to achieve multipatterned 2D hydrogel complex (**Fig. 7.1**).

The dispersed PAAm gels with various concentrations of SA are shown in **Table 3.2**. This method provides a no wash "zero-waste," simple step, and uniform thickness alternative to conventional fabrication methods such as photopolymerization, extrusion, direct ink writing, etc. The multistate 3D shape reconfiguration mechanism with maskless swelling/deswelling was then developed and demonstrated (**Fig. 7.1**). The number of possible configurations of 3D morphing response to external stimulation can be estimated according to the simple equation, for combined through-thickness and in-plane gradient modes

$$2^n X\ 1^m = 2^n \tag{32}$$

where n is associated with the number of in-plan gradient units, while m is associated with the number of through-thickness gradient units. Applied to our proposed structure, the bilayer gave m = 2, and two dissimilar functional blocks on the same plane gave us n = 2, which theoretically leads to four possible shape change configurations besides the original state.

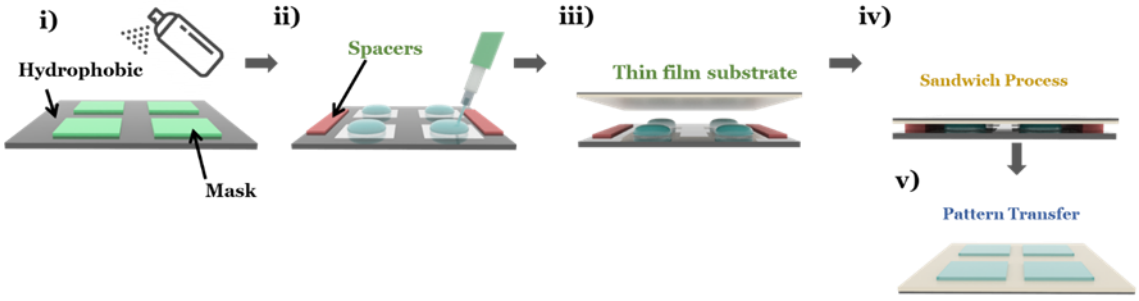

Figure 7.1 Concept of hetergenous structured surface to create structured 3D using wetting controllability. i) Spray coating of glaco on a acrylic plate to produce hierarchical patterned surface; ii) dispensing of dissimilar swelling behavioured polymeric gel composite onto Hele-Shaw cell system; iii) Transfer of non-swelling thin film substrate; iv) Sandwiching of the thin film substrate onto TPP system before polymerization of the patterned gels and v) Heterogenous bilayered system with multi-functional swelling blocks.

7.2.2 Wetting controllability in TPP system

First, the static CAs of pre-gel droplet on various surfaces were characterized as shown in **Fig. 7.2a**. These CA values were similar to those of deionized (DI) water droplets on the same surfaces. The pre-gel droplet dispensing volume was calculated based on the pattern area (x–y plane in **Fig. 7.2b**) and the gap distance g. When droplet volumes between the two plates were properly dispensed, the CA θ' (**Fig. 7.2c left**) remains between 90° and the advancing CA of the hydrogel on the hydrophilic surface (slightly larger than static CA—70° for SiO_2). When the volume is slightly larger (**Fig. 7.2c right**), the gel will still be pinned to the wetting pattern boundary if the θ' lies within the pre-gel advancing CAs on hydrophobic surfaces. The advancing CAs are typically larger than the static CA values as shown in **Fig. 7.2a** —91°, 109°, and 138° for parylene-C (SCS coatings), perfluorooctyltriethoxysilane (FOTS, Sigma–Aldrich), and Glaco Zero (Soft 99), respectively. Capillary-driven flow in a TPP system, where the gap height g is significantly smaller than the dimensions of the droplets (**Fig. 7.2c**), the Reynolds number is small enough for us to assume the dynamics can be studied as 2D Hele-Shaw type flow, where the capillary pressure equation can be simplified to

$$P = K_{xy} + \frac{L}{g} K_z \tag{33}$$

where K_{xy} and K_z are the nondimensional droplet curvatures in TPP geometry (**Fig. 7.2b,c**), L is the droplet length scale at x–y plane that is significantly larger than g. Later work of open microfluidics presented the simplified conditions for the liquid to spread along the hydrophilic area/path when flowing such system, summarized by

$$\frac{g}{w} < \frac{cos\alpha + cos\theta}{2} \quad (34)$$

where g is the gap between top and bottom plates, w is the width of the droplet wetting front (functional block pattern dimensions in this work) perpendicular to the direction of flow, θ and α are the hydrogel static contact angles (CA) on the top and bottom plates, respectively (**Fig. 7.2c**). The droplet will stop spreading when the condition set in Equation (34) is not met, e.g., the fluid hits hydrophobic boundary (CA > 90°), and/ or the gap g is too large (not in our case as $g << w$). Another special consideration is the pre-gel droplet dispensing volume calculation and control. Once the top and bottom plates are in position (g = spacer thickness), a properly controlled dispensing volume should result in a wetting profile as shown in the left-side of **Fig. 7.2c**. However, if the dispensing volume is too large, resulting the θ' > advancing CAs on hydrophobic surfaces, the pre-gel solution will de-pin from the boundary, overflowing the patterns and failing the shape control. Furthermore, due to the relatively small volume changes during this room temperature cross-linking process, nonfunctional substrate wrinkling or bending have not been observed during the functional block polymerization in TPP system.

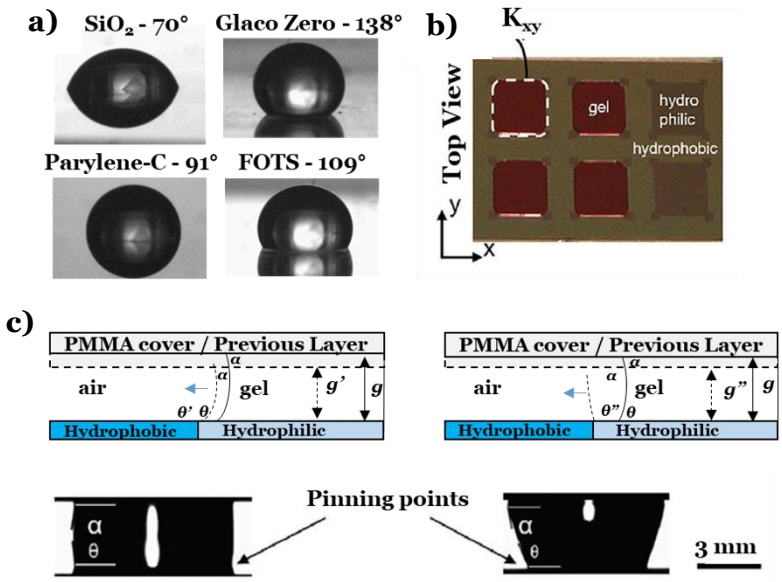

Figure 7.2 The wetting priniciple of the pre-gel PAAm–SA droplets: **a)** Contact angle measurements of the hydrophobic treated surface measured by DSA; **b)** top view experimental evidence of the TPP system with pre-gel droplets (red color dye) assembled and shaped by wetting boundaries; **c)** hydrophobic-hydrophilic interface inspired TPP system showing pre-gel droplets spread on hydrophilic patterns and pinned to the boundaries.

7.2.3 Mechanical characterization of the heterogenous bilayered structures

To understand the deformation behaviour of the heterogeneous hydrogel bilayer structures, mechanical characterization of the functional (PAAm-SA) as well as non-functional (PAAm) hydrogel system was carried out for functional. Due to its porous structure, mechanical properties such as the Young's modulus for hydrogels change during the swelling process. Hence, an in-house designed "clamp-free" tensile testing chamber (**Fig. 7.3**) was developed to characterize the Young's modulus of both functional and nonfunctional hydrogel systems during the swelling process.

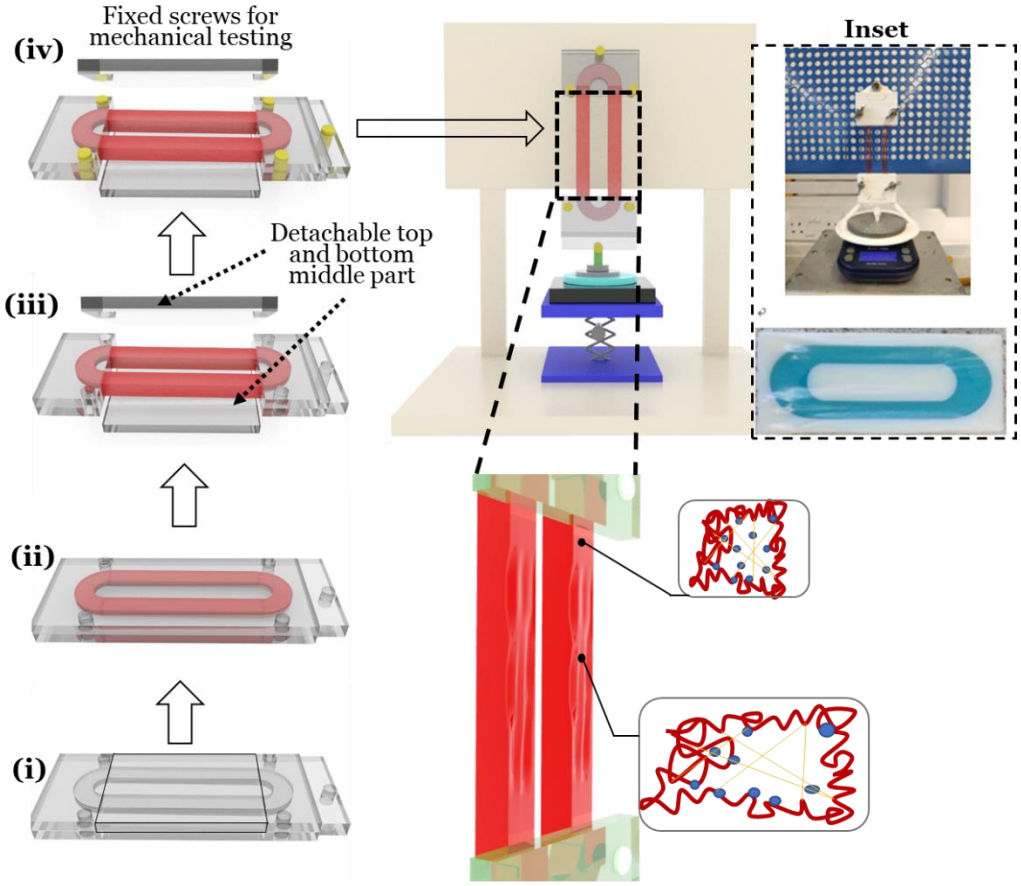

Figure 7.3 In-house developed clamp-free tensile tester for swelling hydrogels, with procedures (i) to (iv) showing the molding setup where as-fabricated PAAm composites can be directly integrated with the tensile tester. (Inset: Working demonstration of the clamp-free tensile tester with prepared gel mold.)

Figure 7.4a shows the strain–stress relationship of the nonfunctional substrate PAAm thin film (**Table 3.2**), immersed in 0.2 and 0.5 M PBS solutions for 10 min. The Youngs modulus is calculated to be ≈10 and ≈7 kPa for the PAAm film swelled in 0.2 and 0.5 M PBS, respectively. **Fig. 7.4b** shows the strain–stress relationship of the functional PAAm-SA hydrogel. It can be clearly seen that the higher PBS concentration resulted in higher Young's modulus in all cases. We attribute this behaviour to highly crystalline nature of the hydrogel molecules reducing the interface defects in the crystalline region and the amorphous area making the elongation longer.

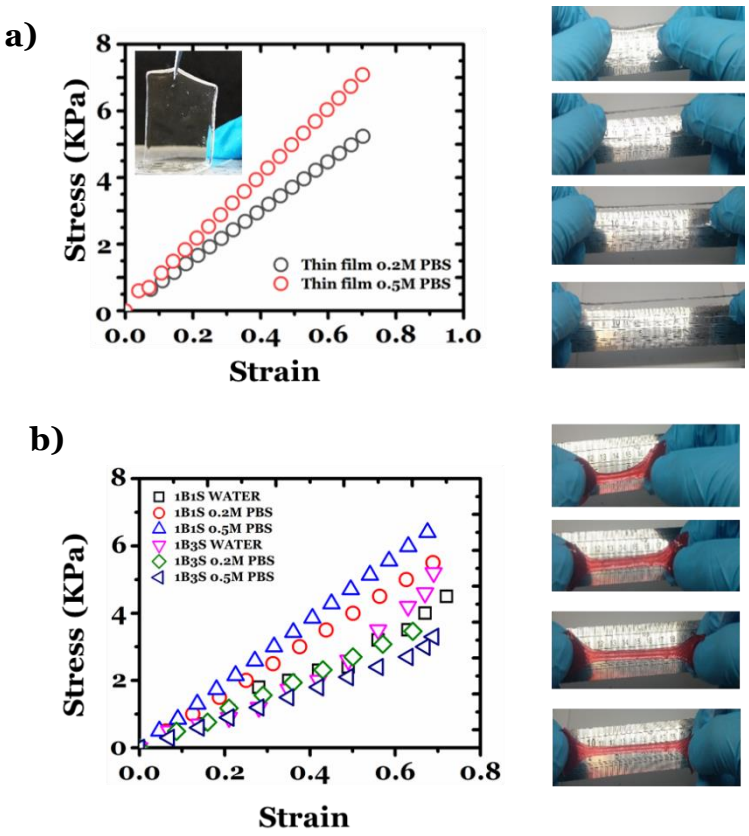

Figure 7.4 Strain–stress relationship of **a)** the nonfunctional substrate PAAm thin film, immersed in 0.2 and 0.5 M PBS solutions for 10 min; and **b)** the functional PAAm–SA immersed in DI water, 0.2 and 0.5 M PBS solutions for 10 min

7.2.4 Swelling characterization of the dynamically responsive heterogenous bilayered structures

The swelling and deswelling ratios dynamically responding to PBS concentration (0–0.5 M) and SA compositions were obtained. In our previous PAAm-SA (different composition) swelling study[280], various boundary confinement conditions were characterized—freestanding, one-side confinement, and ring confinement. In this work, the 3D morphing bilayer structure was placed in "freestand" mode in PBS/water solutions and the swelling ratio characterizations of PAAm and PAAm-SA hydrogel spheres were conducted (**Fig. 7.5**). The swelling ratio was given by

$$.Swelling\ ratio = \frac{d_{\text{swell}}}{d_{\text{origin}}} \quad (35)$$

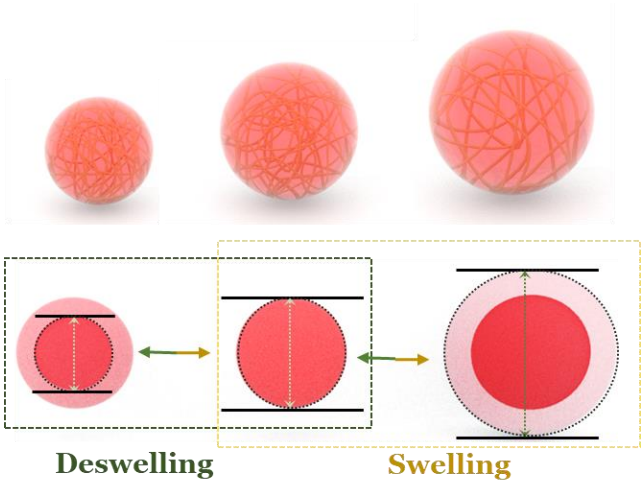

Figure 7.5 Swelling ratio characterization of the functional/non-functional hydrogel spheres under free-standing

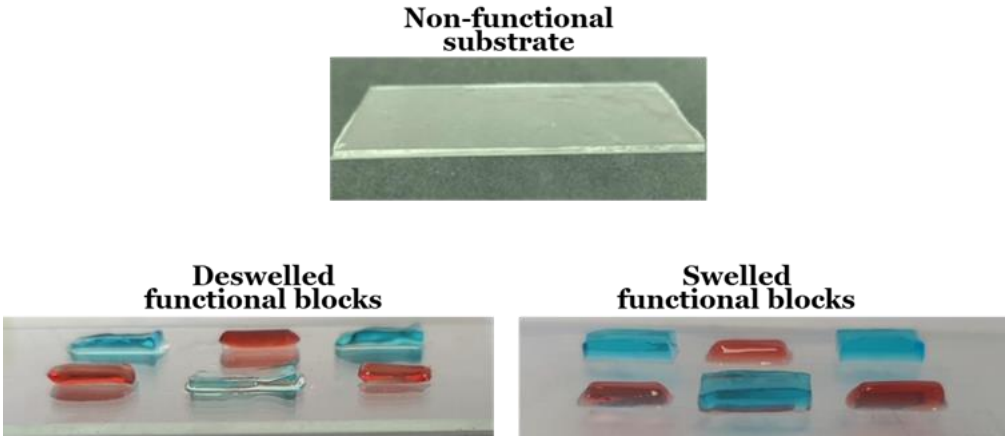

Figure 7.6 Dissimilar swelling behaviour demonstrated on substrate fixed to a PMMA plate.

Fig 7.6 shows the demonstration of the different degree of responsive swelling blocks on a non-functional/unreponsive soft substrate which is fixed to a PMMA plate. As represented, the swellability of functional blocks can be tuned to selective switch between multiple states of freedom towards reconfigurable transducer applications. The large dissimilarity in the swelling/deswelling morphologies of the functional blocks can potentially result in huge deformation magnitudes. Due to the high aspect ratio ($g << w$) of the TPP molding system, the

functional blocks have a large surface area to thickness ratio, compared with the spheres used in swelling test shown in **Fig. 7.5**. This has successfully accelerated the reaction time of the transducers with typical an onset of shape morphing occurring around 2 min of immersion, which was determined by the swelling and deswelling characteristics of the thin functional blocks.

7.2.5 Reconfigurable multilegged 3D morphing demonstration

The localized swelling and deswelling characteristics of the patterned gels and resulting configurations imparted onto the nonfunctional substrate are closely related to the ionic concentration of the environment. The patterned gel's periodicity can be tuned by adding more hydrophilic features onto the hydrophobic polyacrylic plate. Selective dispensing of functional gels with distinctive SA magnitude results in localized spatial configuration with selective swelling and deswelling behaviour that can be switchable under different ionic environment (**Fig. 7.7**).

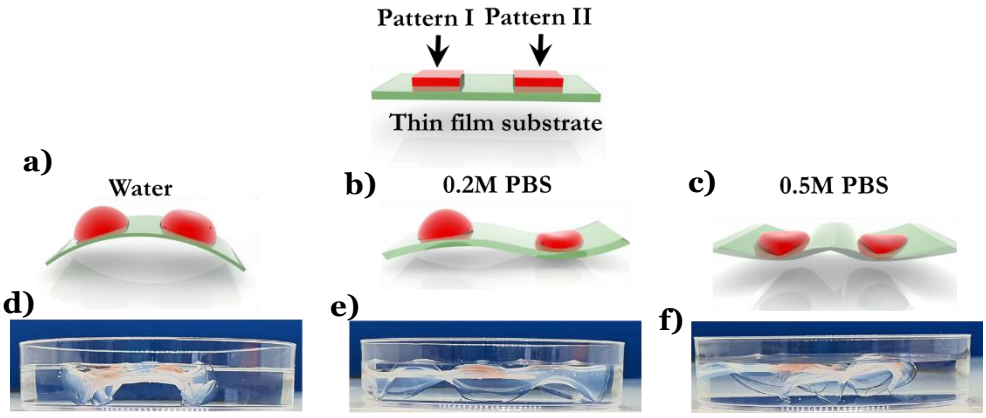

Figure 7.7 Representative complex 3D conformable configurations with mask-free swelling/deswelling, deformed from 2D patterned functional/nonfunctional hydrogels ionic imbalance. **a-d)** Concave deformation achieved by immersing the transducers in DI water with multipatterned demostrability. **b-e)** Buckling mismatch configuration of hydrogel transducer in 0.2 M PBS. **c-f)** Cooperative deswelling of both high and low SA patterns in 0.5 M PBS.

When more than two patterns were involved, complex surface convex and concave buckling can be observed that transients over time with changing diffusion coefficients and ionic equilibrium. As shown in **Fig. 7.7a-d**, both the low (pattern II) and high concentration (pattern I) SA functional blocks swell in DI water at alternative rate due to ionic equilibrium and thus forming a concave shape of the nonfunctional layer. At 0.2 M PBS, due to the osmotic imbalance, high concentration SA patterned functional block undergoes a positive swelling leading to upward buckling of the nonfunctional substrate. Whereas, the low concentration SA functional block undergoes negative swelling leading to downward buckling resulting in a "S"-shaped configuration (**Fig. 7.7b-e**). At 0.5 M PBS, due to increase in PBS concentration, both the functional groups undergo deswelling forming a "W"-shaped configuration that matches our theoretical simulation results (**Fig. 7.7c-f**). We believe, the buckling conformation is achieved due to the influence of high transient swelling forces with swelling mismatch occurring in one of the functional blocks.

7.2.6 Numerical Modeling of the Reconfigurable Deformation

Based on the mechanical characterization results obtained, numerical modeling was conducted to help design/programme the morphing configurations under certain external stimulation. The deformation process of the heterogeneous gel structure is simulated by solving the following matrix model mechanical equilibrium equation

$$\frac{\partial s_{ij}}{\partial X_j} = 0 \qquad (36)$$

where i, j are the rows and columns in matrix, S is the nominal stress tensor and X is the coordinates of the material point in the reference state, i.e. the initial state

of the gel without swelling or de-swelling. The in-plane gradient gel structure composed of only two functional blocks can exhibit three different configurations, i.e., straight (nonactivated), “S”, “C”, and “W” shapes as shown in **Figure 7.8**. When the functional gel block expands (swells), it will induce an internal tensile stress (σ) on the top surface of the nonfunctional substrate, which will generate a clockwise bending moment (M) and bend the unit to a convex configuration (**Fig. 7.8a**). On the other hand, the contracting (deswelling) gel block induces an internal compressive stress on the top surface of the substrate, which will bend the unit to a concave configuration due to the generated counterclockwise bending moment (**Fig. 7.8a**). The radius R of curvature of the unit depends on the swelling ratio (ρ) of the gel, and the thicknesses of the gel (t_g) and the substrate (t_s). Then by scaling analysis, we have

$$\frac{R}{t_g} = f(\rho, \frac{t_s}{t_g}) \tag{37}$$

In the simplest case where both the gel block and the substrate are homogeneous and the unit is simplified as Euler– Bernoulli beam, we can further approximate the scaling as

$$\frac{R}{t_g} = -\frac{t_s/t_g}{2(\rho-1)} \tag{38}$$

where $R < 0$ corresponds to convex configuration and $R > 0$ corresponds to concave one. **Fig. 7.8b** shows the three different cases (reconfigurable states), programmed with two dissimilar functional gel blocks responding to external ion concentration. In the first case where the left gel block (pattern I) expands (swells) and the right one (pattern II) contracts (deswells), the left unit bends to a convex configuration while the right unit bends to a concave one, which leads to an “S” shape of the structure. In the second case, both gel blocks expand, so the two units bend to convex configurations, which make the total structure exhibit a “C” shape. In the third case, both gel blocks contract and the units bend

to concave configurations, leading to a "W" shape. The in-plane gradient gel structure of two different functional blocks is the basic element. By combining more elements, structures exhibiting more complex 3D configurations/shapes can be obtained.

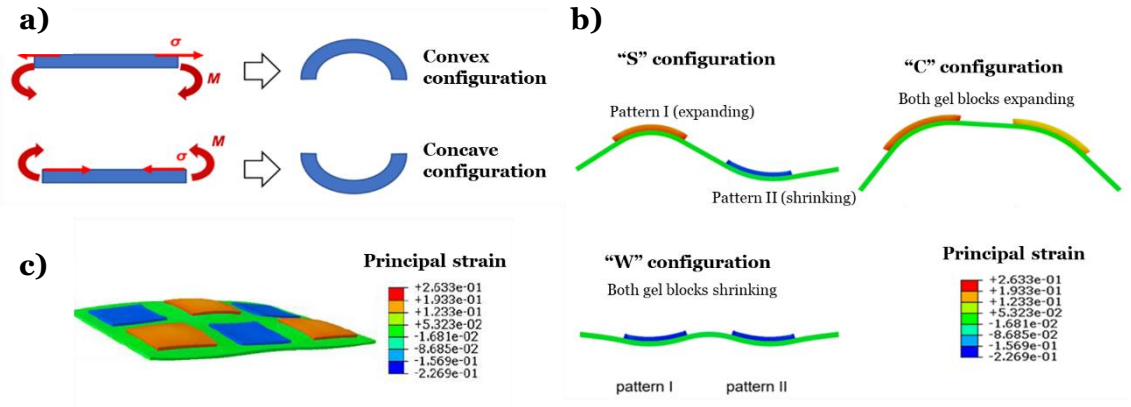

Figure 7.8 Mechanical model of the reconfigurable deformation: **a)** convex and concave configuration due to bending moment; **b)** numerical simulation results showing three different configurations induced by swelling and deswelling of patterns I and II, based on the obtained mechanical property and swelling ratio results and **c)** 3D simulation of multiple elements

7.2.7 Conclusion

Reconfigurable multistate 3D morphing has been achieved through PAAm/PAAm-SA hydrogel bilayer structure that was created in a "TPP" (Hele-Shaw cell) open-microfluidic configuration. The mechanical characterization was carried out to understand the gel property change during the swelling and deswelling processes. The numerical analysis was performed to help understand the morphing states and swelling configurations, which agrees with the experimental observation. The gel structure switching between three different morphing configurations was demonstrated, driven by in-plane and throughthickness heterogeneity during stimuli-responsive swelling subject to ionic concentration change. For example, a triple-layered (or more)

heterogeneous structure exhibiting a dual responsive thermoelectric behaviour can be manufactured to display multiplexed in/output configurations. On the other hand, the reconfigurable morphing structure could also be employed for topography-induced actuations such as complex topo-optical pattern generation. They can also be attached as a replacement for conventional metallic electrodes, organic electrochemical transistors, with tuneable geometry/curvature to be conformal with complex biological surface topography.

Chapter 8

Theoretical developments on Configuring the Deformation induced Rebound behaviour in soft system

8.1 Introduction

The mechanism of self-sustained oscillation within the soft system is rooted in the thermal energy induced self-oscillatory effect (**Fig 8.1**) coupled with rapid elastic vibration at the contact area leading to faster water diffusion with largest elastic energy on the cold end (state 1-state 2). After a brief contact period, due to rapid swelling of the gel and a large elastic energy feedback loop, the sphere gains momentum to overcome the gravitational force and recoils upwards breaking the equilibrium between Leidenfrost force and gravitational force, which in-turn presents an out-of-equilibrium behaviour to impact the piezocrystal attached to the top (state 3) and deforming it to generate electrical pulse (state 4). The theoretical approach in this chapter is carried out both numerically and modelled by considering the comrpession cycle present during the energy injection phase into the sphere. The theory developed was used for predicting scalar relationship profile between the deformation behaviour of the sphere against different surface temperature conditions.

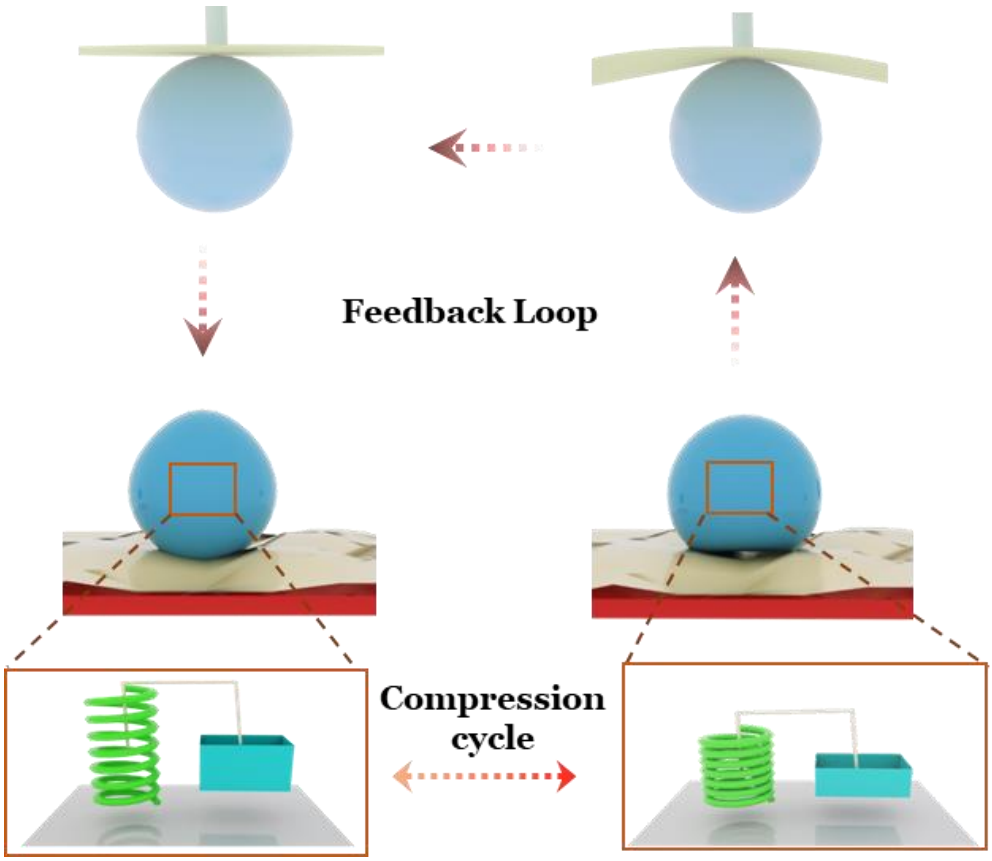

Figure 8.1 Dual stage mechanism of the energy converting unit: The dynamic work-cycle is controlled by an invisible hot gas-vapor layer present over the hot substrate with the piezo-crystal deformation upon sphere impact. Among the work-cycles, the temperature, gap frequency, and specific volume of the gel experience periodic change over time.

In this case, the object soft sphere behaves like a mass-spring model which generally includes elasticity, surface temperature, viscosity, surface energy. The soft sphere was designed with multiple masses and elasticity to yield varied range of elastic deformation profiles under multiple temperature profiles.

8.2 Results

8.2.1 Theoretical Development of the compression cycle

We calculated the total amount of energy injected into the system under variable volume fraction (**Fig 6.13**) to understand the sphere's screeching, vaporization effect on the elastic deformation behaviour. We assume that the net deformation ε is much smaller than the ball's diameter d or $\varepsilon/d << 1$. We modelled the whole impact process as a mass attached to mass-less spring with plates. For the combination, ignoring the viscous forces, the equation of motion for the impact process can be written as

$$m\frac{d^2x}{dt^2} - Kx - mg + F = 0 \qquad (28)$$

From the experimental observation, after the completion of the expansion cycle, the sphere ejects steam which provides the upward energy injection to sustain continuous work cycle. For smaller compression, the kinetic energy is stored as elastic energy and the reaction force (F) and the weight of the sphere is balanced as

$$m\frac{d^2x}{dt^2} - Kx = 0 \qquad (29)$$

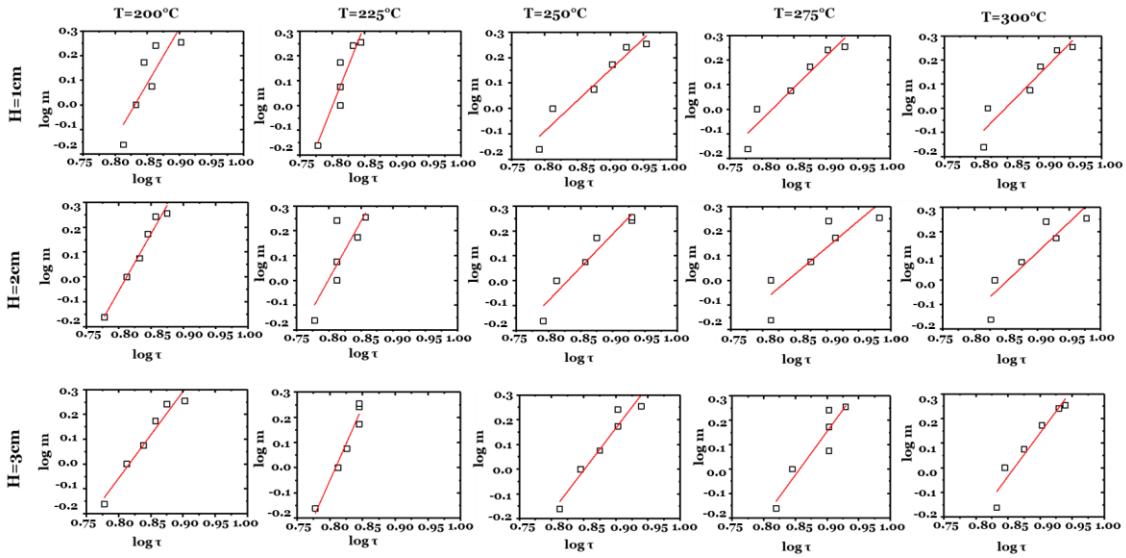

Figure 8.2 Dynamic compression curve for an elastic gel-ball plotted on a log-log scale.

The overall timescale of an impact can be scaled as τ=√(m)/k), wherein, τ is the sphere's contact time at surface, m is the sphere' mass and plotting a log-log scale will yield the spring constant (k) (**Fig 8.2**) at various temperature profiles.

F Δl is the energy provided by the hot substrate which can be scaled as $k`d^2\Delta T\tau$ where k` is the thermal conductivity of the sphere,

$$\eta d\frac{\Delta l^2}{\tau} \sim k`d^2\Delta T\tau \sim k`d^2\Delta T\sqrt{(\mathrm{m}/\mathrm{k})} \qquad (30)$$

From equation (30), the elastic deformation(Δl) of the hydrogel sphere can be scaled as follows,

$$\Delta l \sim \sqrt{\frac{k`md\Delta T}{\eta K}} \qquad (31)$$

Wherein, η is the sphere's viscosity, d is the sphere's diameter, ΔT is the temperature difference between water's boiling temperature and surface temperature,

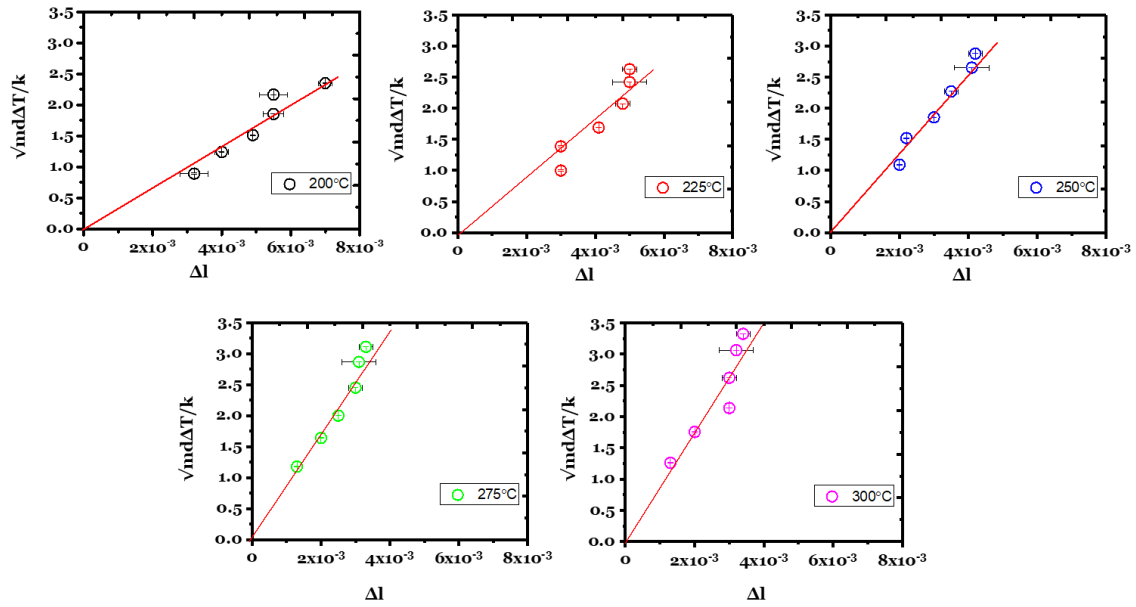

Figure 8.3 Scaling law for deformation of the gel sphere for different surface temperature.

Equation (31) shows that the elastic deformation of the sphere can be scaled over a wide range of temperature (**Fig 8.3**). As evident, the deformation length of the gel sphere is shifted to higher side to accommodate directional transport of increase in latent heat vaporization rate. The kinetics of this elasto-deformation process under thermal diffusion environment is complicated as it corresponds to the parameters such as temperature, atmospheric pressure, vaporization rate, thermodynamic heat transfer, etc, we therefore differ this understanding to the future study.

8.2.2 Theoretical Simulation using ANSYS LS-DYNA

We used solid 168 10-node tetrahedral element for the geometry modelling. The geometry of the element and the meshing results are shown in (a) and (b). We also adopted the viscoelastic model in the simulation.

In the simulation, the Young's modulus E was decided to be ranging between 1-10 Kpa. Then G_0 and K were calculated using the **Table 3.4** above considering a nearly incompressible material (ν=0.49). G_∞ was decided to be equal to $0.85G_0$. $1/\beta$ represents an intrinsic relaxation time. I tested the influence of $1/\beta$ in my simulation by studying the viscoelastic model using solid 168 element geometry and F**ig. 8.4** shows the meshing results.

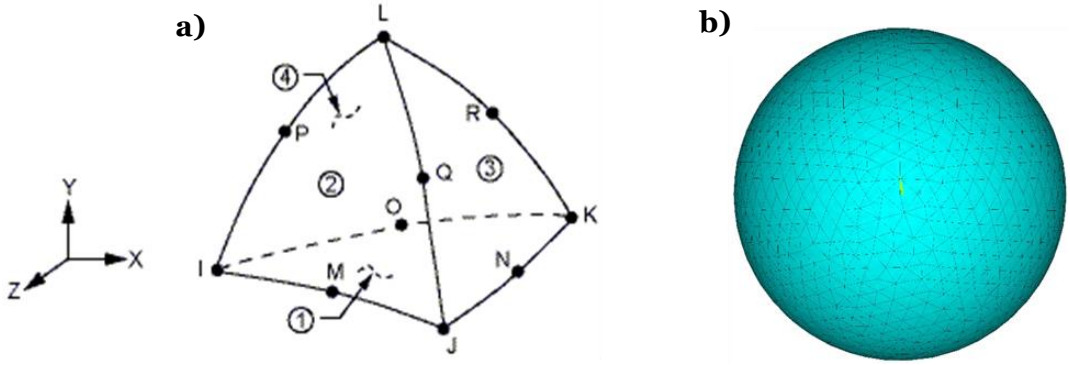

Figure 8.4 Viscoelastic material model **a)** solid 168 element geometry **b)** Meshing results

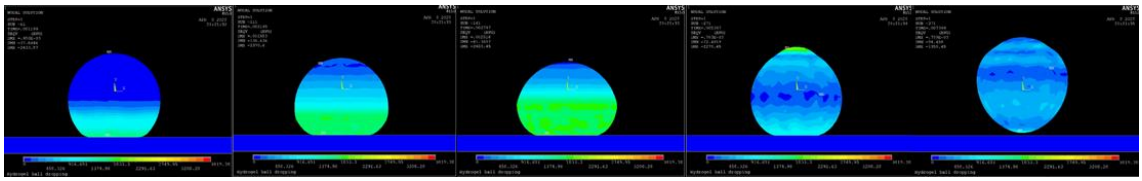

Figure 8.5 Simulated hydrogel deformation upon contact with solid surface

Fig. 8.5 shows the simulated elastic sphere bouncing process with the color legend describing the Von Mises stress distribution. I chose two points (**Fig 8.6a**) and tracked their velocity through out the entire simulation. As shown in **Fig. 8.6b**, the black line represents the velocity of the point at the bottom. We can see high frequency vibration before and after it separates from the plate. By considering the cross-point of the elastic ball, the contact time was found to be near 10 ms and a rebound velocity of 0.77 m/s was seen. More series of simulation was carried out to test the influence of each parameters on the bouncing behaviour including the elastic modulus, impact velocity, relaxation time and ball diameter.

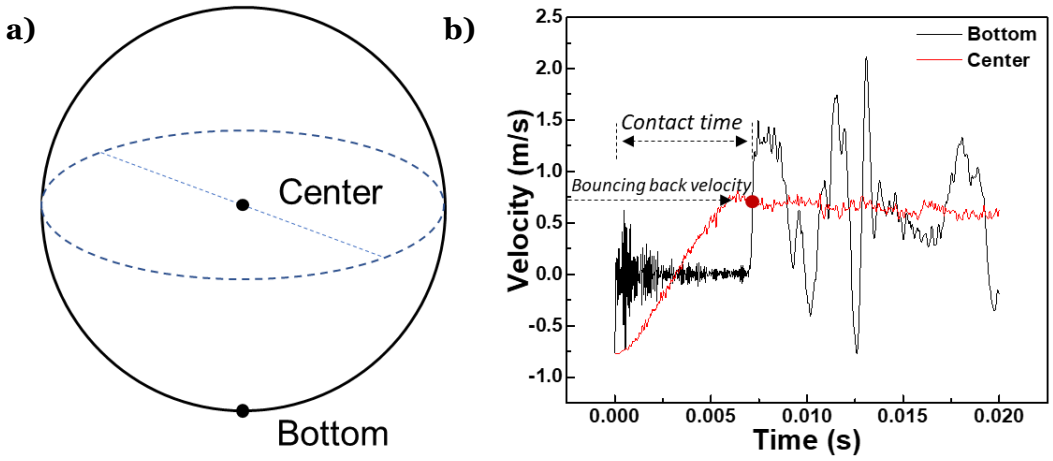

Figure 8.6 Calculated velocity and contact time profile of the elastic sphere at the cross-point

The relaxation time of any hydrogel material found in literature is usually larger than 10s. However, since the specific relaxation time of our material was unknown, a series of simulation was tested to analyse the relaxation time. We can see that a distinct deviation would not take place until the relaxation time is short enough(**Fig. 8.7**). If the relaxation time is comparable to 1ms, its influence on the vibration amplitude and the bouncing back velocity would be significant.

However, any relaxation time longer than 0.01s would not cause significant change on the bouncing behaviour.

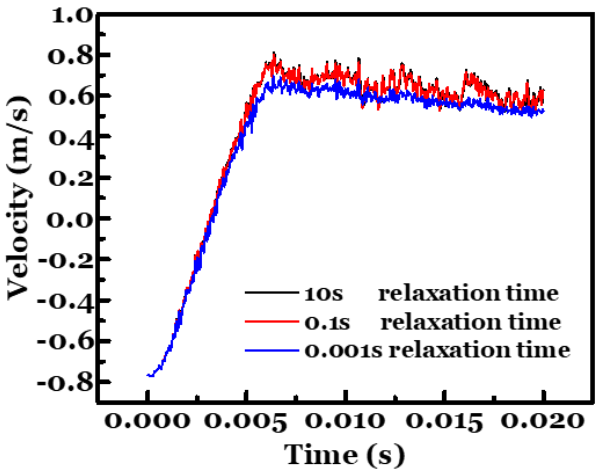

Figure 8.7 Influence of relaxation time on the contact time and velocity ratio

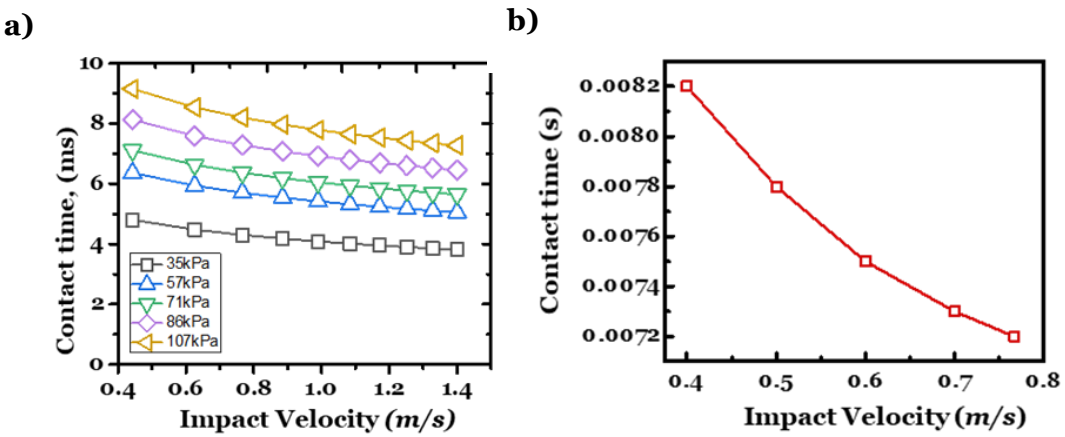

Figure 8.8 Influence of initial velocity on the contact time and impact velocity **a)** Experimental and **b)** Simulated

The results show that larger initial velocity would lead to smaller V_ratio and shorter contact time as shown in **Fig. 8.8**. This could be due to the large energy being spent during elastic deformation and the ideal energy restoration occurs when the sphere is refuelled by extracting thermal energy from the surface to maintain sustainable bouncing. The velocity ratio would not drop until the

Young's modulus is small enough (**Fig. 8.9**) which is attributed to the internal elastic energy.

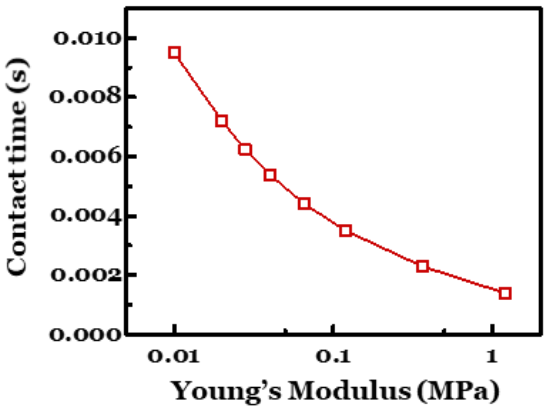

Figure 8.9 Influence of Young's modulus on the contact time

8.3 Conclusion

In this chapter, several theoretical approaches were used to investigate the extreme behaviour conditions of the soft elastic system. A linearity was investigated first to catch a glimpse of the relationship between the influence of surface temperature on the elastic deformation of the soft sphere during impact. The result suggests a near-linear relationship between the two factors, but the model design needs to be further improved to provide an universal scaling law to understand the elastic-Leidenfrost behaviour at extreme surface conditions. For the current technological applications, related parameters were calculated to satisfy the experiment requirements. Moreover, the viscoelastic ANSYS model also sheds light on the influence of multiple parameters that dictates the sustained bouncing effect of the soft sphere system on a solid surface. Although the specific model created controllable macroscopic deformation evolution of the soft system, the microscopic work cycles at the contactual interface of the soft system near hot surface has not yet come to a success due to complex physical

parameters, giving us more room for future studies for high temperature induced elastic-recoil behaviour to achieve continuous bouncing.

Chapter 9

Conclusion and Future Possibilities

9.1 Overall Conclusion

Various surface and interfacial systems enable a convenient strategy of micro-engineering structures imparting unique surface physics and interfacial chemistries. In chapter 4, the thermo-anodized coating technology in order to facilitate supreme thermal, physical and chemical properties on an aluminum surface was investigated. The high performance coating technology produced porous anodic surface with controllability over the porous microstructures and also maintaining its intrinsic characteristics. The influences of coating conditions on the solar absorptivity and emittance of coatings have been systematically studied, and an optimized coating condition is concluded at the current density of 5 A/dm^2 and anodizing temperature of 0 °C. The anodic aluminum alloy obtained showed a thermal emittance and solar absorption of 0.96 and 0.921. Upon exposure to the UV irradiation, the fabricated samples showed the best coating resistance to corrosion by providing a positive corrosion current dentisy. While the anti-corrosion behaviour is an important property, for coating technology in aerospace engineering, surface icephobicity is a crucial criterion as well. On the coated aluminum surface, it is noticed that a droplet can start to resist itself from attaching and spreading as the annealing temeprature of the surface was increased. To achieve highly controlled anti-icing feature, the surface was coated with a silane layer to initialize localized hydrophobic moeities that induced non-adherent chemical groups to prevent droplets from frosting. The static, advancing and receding contact angles were measured before and after

silane treatment under increasing temperature profile, showing the enhancement of the anti-icing features due to changes in the surface chemistry, morphology and roughness.

In chapter 5, a strategy towards fabricating a stimuli-responsive smart hybrid surface combined with 3D printed miniature groove structure and injected acrylate hydrogel embedded microstructures was realized. The smart surface was designed in such a way that they could realize and adapt to liphophilic and oleophobic regime depending on the stimuli. Successful geometrical change of the hydrogel surface was predicted due to the inherent structural confinement and continuous transition of the gel surface topology. By controlling the swelling ratios of hydrogels, successful reversible lipophilic/oleophobic property changes have been demonstrated which are a prerequisite in providing a barrier layer for liquid separation. However, a quick shift in the patterned structure for efficient oil-liquid separation transition can be realized by selectively actuating the gel constructs on command for potential applications as an autonomous system for future sub-sea/off-shore engineering applications to separate oil and water.

Chapter 6 is focussed on the recent, not fully studied elastic Leidenfrost behaviour which is seen in soft elastic solids that periodically bounce with improved elastic energy. By introducing elastically tunable soft spheres, the overal elastic instabilities present in the previous studies can be compensated to provide a long-lasting kinetic energy. The experimental patterns and thresholds were understood by considering a simple elastic gel composite decorated by various Young's modulus for improved substrate-deformation. The experiments also show localized gap oscillations (work cycles) that can be further tuned by altering the soft sphere's Young's modulus yielding a modest deformation at

various surface temperature. By varying the geometrical inputs of the Leidenfrost surfaces, the control over the stepwise evolution of energy translation was demonstrated. These results demonstrate considerable control over both soft sphere and surface textures. Finally the realization of such an unexplored extreme surface phenomenon into useful emerging applications was carried out. The sucessful integration of soft sphere into a tubular confinement to direct their bouncing behaviour in order to impact piezocrystal was realized. The amount of electrical energy being produced during a single work cyle is sufficient enough to light up LEDs or be stored in a capacitor for future energy discharge. Such a novel, upcoming extreme devices can be used as a waste-heat harvesting system, energy translation devices to power electronic gadgets in locations with high geothermal sources.

Chapter 7 sheds light on a facile open-microfluidic approach inspired by Hele-Shaw cell to create a multipatterned reconfigurable 3D soft morphing transducer. The technique uses switchable soft materials guided by an in-plane and through thickness heterogenity which can be actuated by external stimuli such as variation in ionic concentration. Moreover, the 3D configurations achieved by the structure is also infleunced by the swelling and deswelling characteristics of the individual soft patterns which provides a multifaceted in/output configurations. We also explored the evidence of morphing states and swelling configurations experienced through the experiments via numerical analysis. Such, a novel multiadjustable and intrically tunable soft system will finds in way in extreme transducer applications and shape adaptable soft robotics towards soft transport, cargo delivery, etc.

In chapter 8, two different theoretical approaches was presented to understand the elastic soft sphere behaviour at the surface under centain surface temperature profiles and velocity profiles. Initial theoretical understanding sheds light on the simple scaling property that provides linear realtionship between the elastic deformation of the sphere at multiple surface temperature profiles. Another model studied by ANSYS uses a viscoelastic theory which is proceeded with different paramenters that affect the sphere's physical parameters such as rebound velocity, contact timem etc. The experimentally structured elastic recoiling profile was simplified into a simple bouncing ball to reduce the computer working process. The deformation induced bouncing elastic recoiling along with impact velocity induced rebound behaviour was analysed and achieved reasonable relationship parameters. However, an in-depth understanding of the surface phenomenon (Leidenfrost effect) influencing an elastic system is still a mystery for further analysis that corresponds to provide a profoundly attenuated bouncing profile for future extreme application developments.

9.2 Future Possibilities

Further to the work discussed in this thesis, some research challenges remain and more works are required to realize further system optimization.

In chapter 4, there has been some progress in utilizing a novel route that uses anodic temperature effect to control the porous nature of the aluminum substrate resulting in the formation of a black layer that poses superior solar absorptivity and thermal emittance. Anti-corrosion and anti-icing also proved to be extremely compelling. However, there still exists issues on the ice formation at the surface.

Improvements could always be made to reduce the water adhesion and ice formation at low annealing temperature by a highly vaporizable silane solution that provides improved surface coating.

In chapter 5, a smart switchable hybrid groove-hydrogel structure was designed that creates an intelligent surface behaviour towards oil-water separation. Initial experiments on the design and quick response hydrogel system provides a convincing oil-water separation property. However, after 4 hours, the surface contact angles changed from 102.6° to 83.4° indicating a time limit for the process. And also, in addition to chemically treating the surface to render them super-oleophobic/hydrophobic, different geometric designs were introduced. The system could be significantly improved by playing around with different fast swtiching/responding polymeric constructs which can be tuned to be selectively sensitive towards a specific stimuli. And by tuning the junction gap between neighboring gel systems, a quicker buckling stature could be realized to improve the longevity of the device. Most qualitative performances demonstrated in this thesis was carried out in a static environment. The future plan is to make the system more reliable on a dynamic scale wherein a fluid stream containing oil and water could be tested for real-time application.

As described in chapter 6, the polymeric system wears off its bouncing motion eventually due to the presence of water as an solvent which has its boiling point at 100°C and vaporizes as the temperature crosses the boiling point. Currently the system can bounce for a lifetime of more than 10 minutes and also maintain the bouncing height of 3 cm due to the physical confinement. To further improve the system, future work will focus on testing different solvents being used to prepare the polymeric system for an improved life time to weeks or even longer.

Morever, much more complex textured patterns on the surface can be realized to provide better gas-vapor flow that could not only fuel the system but also allow further cooling of the system by dissipating heat through the topographical features. And the applicability of connecting more such pocket systems made of elastic sphere and piezocrystal could be realized to provide scalability on a larger scale (currently 4 systems can work simulataneously) and improved stepwise electrical signal by modifying the piezocrystal that translates towards more output power.

Chapter 7 poses an important deal in the domain of wetting-enabled gel assembly process. Inspired by the widely available printing techniques such as ODF (one droplet filling) employed in liquid crystal display manufacturing, controllability over shape during the gelation process can provide superior scaling up /down. Further study involving the one drop filling technique (ODF) will be of prime interest to adopt this technology towards open-microfluidics configurations.

Chapter 8 poses an important deal in the theoretical development of the elastic ball bouncing upon impacting the surface and its rebound behaviour. The chapter provides an insight into the understanding of developing a scalable law which includes surface temperature and -induced elastic deformation behaviour which is believed to control amount of energy being harvested from the thermal source. In order to understand how much thermal energy is being translated into the polymer system during the contact time would be of profound value to unravel in the future. Furthermore, currently the understanding of the Leidenfrost behaviour in liquid systems has advanced, the number of satisfactory models available in the public domain is very few. Hence, the Leidenfrost model has always been a complex myth and developing a compelling model that covers

surface energy, elastic energy, vaporization rate, would be a task to play around in the future.

BIBLIOGRAPHY

[1] R. N. Wenzel, Ind. Eng. Chem. Res. 1936, 28, 988.

[2] G. D. Bixler, B. Bhushan, Adv. Func. Mater. 2013, 23, 4507.

[3] A. Alizadeh, V. bhadur. A. Kulkarni, M. Yamada, MRS Bullet. 2013, 38, 407.

[4] Y. Cai, L. Lin, Z. Xue, M. Liu, S. Wang, L. Jiang, Adv. Funct. Mater. 2014, 24, 809.

[5] D. Quere, Nat. Mater. 2013, 11, 915.

[6] R. Mezzenga, J. M. Seddon, C. J. Drummond, B. J. Boyd, G. E. Schroder-Turk, L. Sagalowicz, Adv. Mater. 2019, 1900818.

[7] T. Sun, G. Qing, B. Su, L. Jiang, Chem. Soc. Rev. 2011, 40, 2909.

[8] H. Guo, Z. Wen, Y. Zi, M.-H. Yeh, J. Wang, L. Zhu, C. Hu, Z. L. Wang, Adv. Energ. Mater. 2016, 6, 1501593.

[9] Y. Park, G. Vella, K. J. Loh, Sci. Rep. 2019, 9, 18609.

[10] Y. Liu, K. He, G. Chen, W. R. Leow, X. Chen, Chem. Rev. 2017, 117, 12893.

[11] T. R. Ray, J. Choi, A. J. Bandodkar, S. Krishnan, P. Gutruf, L. Tan, R. Ghaffari, J. A. Rogers, Chem. Rev. 2019, 119, 5461.

[12] H. Wang, Y. Yang, L. Guo, Adv. Energ. Mater. 2016, 7, 1601709.[13] Q. Li, A. P. H. Schenning, T. J. Bunning, Adv. Opt. Mater. 2019, 7, 1901160.

[14] B. Maiti, A. Abramov, L. Franco, J. Puiggalí, H. Enshaei, C. Alemán, D. D. Díaz, Adv. Func. Mater. 2020, 30, 2001683.

[15] Y. Li, D. Wang, J. Richardson, B. B. Xu, Macromol. Symp. 2017, 1.

[16] W. Xu, L.-B. Huang, M.-C. Wong, L. Chen, G. Bai, J. Hao, Adv. Energ. Mater. 2016, 1601529.

[17] H. Zhang, H. Zeng, A. Priimagi, O. Ikkala, Nat. Commun. 2019, 10, 3267.

[18] H. Qin, T. Zhang, N. Li, H.-P. Cong, S.-H. Yu, Nat. Commun. 2019, 10, 2202.

[19] L.-W. Xia, R. Xie, X.-J. Ju, W. Wang, Q. Chen, L.-Y. Chu, Nat. Commun. 2013, 4, 2226.

[20] A. K. Denisin, B. L. Pruitt, ACS Appl. Mater. Interfaces 2016, 8, 21893.

[21] L. M. Lira, K. A. Martins, S. I. Torresi, Eur. Polym. J. 2009, 45, 1232.

[22] B. Xiong, R. D. Loss, D. Shields, T. Pawlik, R. Hochreiter, A. L. Zydney, M. Kumar, npj Clean Water 2018, 1, 17.

[23] D. A. Z. Wever, F. Picchioni, A. A. Broekhuis, Ind. Eng. Chem. Res. 2013, 52, 16352.

[24] X. Li, Z. Xu, H. Yin, Y. Feng, H. Quan, Energy Fuels 2017, 31, 2479.

[25] S. Wang, G. Kim, Y.-E. K. Lee, H. J. Hah, M. Ethirajan, R. K. PandeyR. Kopelman, ACS Nano 2012, 6, 6843.

[26] Y. Zhang, T. H. Tao, Adv. Mater. 2019, 1905767.

[27] Z. Rao, F. Ershad, A. Almasri, L. Gonzalez, X. Wu, C. Yu, Adv. Mater. Interfaces 2020, 2000233.

[28] T. Ma, E. Balanzat, J.-M. Janot, S. Balme, ACS Appl. Mater. Interfaces 2019, 11, 12578.

[29] C. Martín, S. Merino, J. M. González-Domínguez, R. Rauti, L. Ballerini, M. Prato, E. Vázquez, Sci. Rep. 2017, 7, 10942.

[30] M.-J. Yin, Y. Zhang, Z. Yin, Q. Zheng, A. P. Zhang, Adv. Mater. Tech. 2018, 3, 1800051.

[31] C. Appiah, C. Arndt, K. Siemsen, A. Heitmann, A. Staubitz, C. Selhuber-Unkel, Adv. Mater. 2019, 31, 1807747.

[32] Y. Sun, Z. Guo, Nanoscale Horiz. 2019, 4, 52.

[33] Y. Tian, B. Su, L. Jiang, Adv. Mater. 2014, 26, 6872.

[34] D. Quere, Annu. Rev. Mater. Res. 2008, 38, 71.

[35] A. Lafuma, D. Quere, Nat. Mater. 2003, 2, 457.

[36] F. E. Bartell, J. W. Shepard, J. Phys. Chem. 1953, 57, 211.

[37] V. Hejazi, A. D. Moghadam, P. Rohatgi, M. Nosonovsky, Langmuir 2014, 30, 9423.

[38] D. Wang, N. Cheewaruangroj, Y. Li, G. McHale, Y. Jiang, D. Wood, J. S. Biggins, B. B. Xu, Adv. Func. Mater. 2017, 1704228.

[39] D. Kim, N. M. Pugno, S. Ryu, Sci. Rep. 2016, 6, 37813.

[40] B. M. L. Koch, A. Amirfazli, J. A. W. Elliott, J. Phys. Chem. C. 2014, 118, 23777.

[41] T. L. Liu, Z. Chen, C.-J. Kim, Soft Matter, 2015, 11, 1589.

[42] A. B. D. Cassie, S. Baxter, Trans. Faraday Soc., 1944, 40, 546.

[43] D. Xia, L. M. Johnson, G. P. Lopez, Adv. Mater., 2012, 24, 1287.

[44] M. S. Sadullah, J. R. Panter, H. Kusumaatmaja, Soft Matter 2020, 16, 8114.

[45] G. McHale, R. Ledesma-Aguilar, G. G. Wells, J of Bionic Engineering 2020, 17, 633.

[46] C. Howell, A. Grinthal, S. Sunny, M. Aizenberg, J. Aizenberg, Adv. Mater. 2018, 30, 1802724.

[47] J. D. Smith, R. Dhiman, S. Anand, E. Reza-Garduno, R. E. Cohen, G. H. McKinley, K. K. Varanasi, Soft Matter 2013, 9, 1772.

[48] N.-X. Zhu, Z.-W. Wei, C.-X. Chen, D. Wang, C.-C. Cao, Q. F. Qiu, J.-J. Jiang, H.-P. Wang, C.-Y. Su, Angew. Chem. Int. Ed. 2019, 58, 24.

[49] R. David, A. W. Neumann, Langmuir 2013, 29, 4551.

[50] H. Li, W. Fang, Y. Li, Q. Yang, M. Li, Q. Li, X.-Q. Feng, Y. Song, Nat. Commun. 2019, 10, 950.

[51] A. M. J. Wdwards, R. Ledesma-Aguilar, M. I. Newton, C. V. Brown, G. McHale, Sci. Adv. 2016, 2, e1600183.

[52] S. Yun, Sci. Adv. 2017, 7, 17699.

[53] Y. Liu, L. Moevius, X. Xu, T. Qian, J. M. Yeomans, Z. Wang, Nat. Commun. 2014, 10, 515.

[54] L. Wang, R. Wang, J. Wang, T.-S. Wong, Sci. Adv. 2020, 6, eabb2307.

[55] T. M. Schutzius, S. Jung, T. Maitra, G. Graeber, M. Kohme, D. Poulikakos, Nat. Commun. 2015, 527, 82.

[56] M. K. Chaudhury, G. M. Whitesides, Science 1992, 256, 1539.

[57] D. Baratian, A. Cavalli, D. van den Ende, F. Mugele, Soft Matter 2015, 11, 7717.

[58] J. Oh, C. E. Dana, S. Hong, J. K. Román, K. D. Jo, J. W. Hong, J. Nguyen, D. M. Cropek, M. Alleyne, N. Miljkovic, ACS Appl. Mater. Interfaces 2017, 9, 27173.

[59] Q. Wang, X. Yao, H. Liu, D. Quere, L. Jiang, Proc. Natl. Acad. Sci. U. S. A. 2015, 112, 9247.

[60] J. B. Boreyko, C. H. Chen, Phys. Rev. Lett. 2009, 103, 4184501.

[61] A. L. Biance, F. Chevy, C. Clanet, G. Lagubeau, D. Quere, J. Fluid Mech. 2006, 554, 47.

[62] T. Tran, H. J. J. Staat, A. Prosperetti, C. Sun, D. Lohse, Phys. Rev. Lett. 2012, 108, 5036101.

[63] P. Bourrianne, C. Lv, D. Quere, Sci. Adv. 2019, 5, eaaw0304.

[64] S. Lyu, V. Mathai, Y. Wang, B. Sobac, P. Colinet, D. Lohse, Sci. Adv. 2019, 5, eaav8081.

[65] D. Quéré, Annu. Rev. Fluid Mech. 2013, 45, 197.

[66] A. Hashmi, Y. Xu, B. Coder, P. A. Osborne, J. Spafford, G. E. Michael, G. Yu, J. Xu, Sci. Rep. 2012, 2, 797.

[67] I. U. Vakarelski, N. A. Patankar, J. O. Marston, D. Y. C. Chan, S. T. Thoroddsen, Nature 2012, 489, 274.

[68] H. Snoeijer, P. Brunet, J. Eggers, Phys. Rev. E 2009, 79, 036307.

[69] J. C. Burton, A. L. Sharpe, R. C. A. van der Veen, A. Franco, S. R. Nagel, Phys. Rev. Lett. 2012, 109, 074301.

[70] J. G. Leidenfrost, Duisburg, 1756.

[71] L. Zhong, Z. Guo, Nanoscale 2017, 9, 6219.

[72] P. Zhang, B. Peng, J. Wang, L. Jiang, Adv. Func. Mater. 2019, 1904535.

[73] A. Bouillant, T. Mouterde, P. Bourrianne, A. Lagarde, C. Clanet, D. Quéré. Nat. Physics 2018, 14, 1188.

[74] M-Y. Chen, Z.-H. Jia, T. Zhang, Y.-Y. Fei, Appl. Surf. Sci. 2018, 433, 336.

[75] M. Mrinal, X. Wang, C. Luo, Langmuir 2017, 33, 6307.

[76] B. S. Yilbas, A. A. Sharafi, H. Ali, N. A.-Ageeli, RSC Adv. 2017, 7, 48806.

[77] P. Prabhakaran, A. Krekhov, E. Bodenschatz, S. Weiss, J. Stat. Phys. 2019, 175, 598.

[78] P. Agrawal, G. G. Wells, R. Ledesma-Aguilar, G. McHale, A. Buchoux, A. Stokes, K. Sefiane, Applied Energ. 2019, 240, 399.

[79] M. Shi, X. Ji, S. Feng, Q. Yang, T. J. Lu, F. Xu, Sci. Rep. 2016, 6, 28574.

[80] G. G. Wells, R. Ledesma-Aguilar, G. McHale, K. Sefiane, Nat. Commun. 2015, 6, 6390.

[81] A. L. Biance, C. Clanet, D. Quere, Phys. Fluids. 2003, 15, 1632.

[82] J. D. Bernardin, I. Mudawar, Trans. ASME 1999, 121, 894.

[83] T. Zhang, J. Wang, L. Chen, J. Zhai, Y. Song, L. Jiang, Angew. Chem. Int. Ed. 2011, 1.

[84] S. Chandra, C. T. Avedisian, Proc. Royal Soc. A. 1991, 432, 1.

[85] J. T. Ok, E. Lopez-Oña, D. E. Nikitopoulos, H. Wong, S. Park, Microfluid. Nanofluid. 2010, 10, 1045.

[86] C. Ukiwe, D. Y. Kwok, Langmuir 2005, 21, 666.

[87] S. Chen, V. Bertola, Soft Matter 2016, 12, 7624.

[88] S. H. Kim, H. S. Ahn, J. Kim, M. Kaviany, M. H. Kim, Appl. Phys. Lett. 2013, 102, 233901.

[89] H. Kim, B. Truong, J. Buogiorno, L.-W. Hu, Appl. Phys. Lett. 2011, 98, 083121.

[90] S. M. Sajadi, P. Irajizad, V. Kashyap, N. Farokhnia, H. Ghasemia, Appl. Phys. Lett. 2017, 111, 021605.

[91] V. Talari, P. Behar, Y. Lu, E. Haryadi, D. Liu, Front. Energ. 2018, 12, 22.

[92] M. A. J. van Limbeek, M. Shirota, P. Sleutel, C. Sun, A. Prosperetti, D. Lohse, Int. J. Heat and Mass Trans. 2016, 97, 101.

[93] J. Wu, H. Shi, T. Zhao, Y. Yu, S. Dong, Adv. Func. Mater. 2016, 1.

[94] B. Russ, A. Glaudell, J. J. Urban, M. L. Chabinyc, R. A. Segalman, Nat. Rev. Mater. 2016, 1, 16050.

[95] H. Yang, L. A. Jauregui, G. Zhang, Y. P. Chen, Y. Wu, Nano Lett. 2012, 12, 540.

[96] V. E. Nakoryakov, S. Ya. Misyura, S. L. Elistratov, Int. J. Heat Mass Transf. 2012, 55, 6609.

[97] S. Jowkar, M. R. Morad, Soft Matter 2019, 15, 1017.

[98] W. Zhang, T. Yu, J. Fan, W. Sun, Z. Cao, J. Appl. Phys. 2016, 119, 1.

[99] X. Yan, L. Zhang, S. Sett, L. Feng, C. Zhao, Z. Huang, H. Vahabi, A. K. Kota, F. Chen, N. Miljkovic, ACS Nano 2019, 13, 1309.

[100] P. Zhang, B. Peng, X. Yang, J. Wang, L. Jiang, Adv. Mater. Interfaces 2020, 2000501.

[101] M. Liu, J. Li, X. Zhou, J. Li, S. Feng, Y. Cheng, S. Wang, Z. Wang, Adv. Mater. 2020, 1907999.

[102] S. Shi, C. Lv, Q. Zheng, Soft Matter 2020, 16, 5388.

[103] L. Mishchenko, B. Hatton, V. Bahadur, J. A. Taylor, T. Krupenkin and J. Aizenberg, ACS Nano 2010, 4, 7699.

[104] A. Alizadeh, V. Bahadur, S. Zhong, W. Shang, R. Li, J. Ruud, M. Yamada, L. Ge, A. Dhinojwala and M. Sohal, Appl. Phys. Lett. 2012, 100, 111601.

[105] D. V. Svintradze, Sci. Rep. 2019, 9, 6105.

[106] C. Raufaste, G. R. Chagas, T. Darmanin, C. Claudet, F.Guittard, F. Celestini, Phy. Rev. let. 2017, 119, 108001.

[107] S. Pan, R. Guo, J. J. Richardson, J. D. Berry, Q. A. Besford, M. Björnmalm, G. Yun, R. Wu, Z. Lin, Q.-Z. Zhong, J. Zhou, Q. Sun, J. Li, Y. Lu, Z. Dong, M. K. Banks, W. Xu, J. Jiang, L. Jiang, F. Caruso, Adv. Sci. 2019, 6, 1901846.

[108] S. Mettu, M. K. Chaudhury, Langmuir 2008, 24, 10833.

[109] M. K. Chaudhury, A. Chakrabarti, S. Daniel, Langmuir 2015, 31, 9266.

[110] S. Feng, S. Wang, Y. Tao, W. Shang, S. Deng, Y. Zheng, Y. Hou, Sci. Rep. 2015, 5, 10067.

[111] T. Singla, M. Rivera, Phys. Rev. Fluids 2020, 5, 113604.

[112] L. Wang, S. Rong, S. Shen, T. Wang, Z. Che, Int. J. Heat Mass Transfer 2020, 148, 119116.

[113] H. Qi, T. Wang, Z. Che, Phys. Rev. E 2020, 101, 043114.

[114] X. Ma, J.-J. Lietor-Santos, J. C. Burton, Phys. Rev. Fluids 2017, 2, 031602.

[115] J. Li, X. Zhou, Y. Zhang, C. Hao, F. Zhao, M. Li, H. Tang, W. Ye, Z. Wang, Small 2019, 1901751.

[116] C. Liu, J. Sun, J. Li, C. Xiang, L. Che, Z. Wang, X. Zhou, Sci. Rep. 2017, 7552.

[117] R. Yamada, H. Tada, Langmuir 2005, 4254.

[118] Y. Sumino, N. Magome, T. Hamada, K. J. Yoshikawa, Phys. Rev. Lett. 2009, 068301.

[119] J. Li, Q. H. Qin, A. Shah, R. H. A. Ras, X. Tian, V. Jokinen, Sci. Adv. 2016, 2, e1600148.

[120] A. Al-Sharafi, B. S. Yilbas, H. Al-Qahtani, Sci. Rep. 2020, 10, 4594.

[121] P. Zhu, R. Chen, L. Wang, Adv. Sci. 2019, 6, 1900798.

[122] S. Shiri, J. C. Bird, Proc. Natl. Acad. Sci. U. S. A 2017, 114, 6930.

[123] Y. Wen, P. Y. Kim, S. Shi, D. Wang, X. Man, M. Doid, T. P. Russell, Soft Matter 2019, 15, 2135.

[124] J. M. Arter, D. J. Cleaver, K. Takashina, A. T. Rhead, Appl. Phys. Lett. 2018, 113, 24370.

[125] C. Kruse, I. Somanas, T. Anderson, C. Wilson, C. Zuhlke, D. Alexander, G. Gogos, S. Ndao, Microfluid Nanofluidics 2015, 18, 1417.

[126] X. Man, M. Doi, Phys. Rev. lett. 2017, 119, 044502.

[127] D. Liu, T. Tran, J. Phys. Chem. Lett. 2018, 9, 4771.

[128] Á. G. Marín, D. A. del Cerro, G. R. B. E. Römer, B. Pathiraj, A. H. in 't Veld, D. Lohse, Phys. Fluids 2012, 24, 122001.

[129] G. Dupeux, P. Bourrianne, Q. Magdelaine, C. Clanet, D. Quéré, Sci. Rep. 2015, 4, 5280.

[130] B. Sobac, A. Rednikov, S. Dorbolo, P. Colinet, Phys. Fluids 2017, 29, 082101.

[131] Z.-H. Wu, W.-H. Chang, C.-l. Suna, Int. J. Thermal Sci. 2018, 129, 254.

[132] Z. H. Jia, M. Y. Chen, H. T. Zhu, Appl. Phys. Lett. 2017, 110, 5.

[133] H. Linke, B. J. Alemán, L. D. Melling, M. J. Taormina, M. J. Francis, C. C. Dow-Hygelund, V. Narayanan, R. P. Taylor, A. Stout, Phys. Rev. Lett. 2006, 96, 154502.

[134] A. Grounds, R. Still, K. Takashina, Sci. Rep. 2012, 2, 720.

[135] J. Li, W.-Y. Wong, X.-M. Tao, Nanoscale 2020, 12, 1281.

[136] S. Chen, V. Bertola, Phys. Rev. E. 2016, 94, 021102.

[137] S. Chen, V. Bertola, Soft Matter 2016, 12, 7624.

[138] T. C. de Goede, K. G. de Bruin, N. Shahidzadeh, D. Bonn, Phys. Rev. Fluids 2019, 4, 053602.

[139] J. T. Pham, M. Paven, S. Wooh, T. Kajiya, H.-J. Butt, D. Vollmer, Nat. Commun. 2017, 8, 905.

[140] M. Michalska-Domanska, W. J. Stepniowski, L. R. Jaroszewicz, J. Porous Mater. 2017, 24, 779.

[141] Z. Wang, D. van den Ende, A. Pit, R. Lagraauw, D. Wijnperléa, F. Mugele, Soft Matter 2017, 13, 4856.

[142] G. Launay, M. S. Sadullah, G. McHale, R. Ledesma-Aguilar, H. Kusumaatmaja, G. G. Well, Sci. Rep. 2020, 10.

[143] Y. Huang, B. B. Stogin, N. Sun, J. Wang, S. Yang, T. S. Wong, Adv. Mater. 2017, 29, 1604641.

[144] A. Ainla, M. M. Hamedi, F. Guder, G. M. Whitesides, Adv. Mater. 2017.

[145] P. Teng, D. Tian, H. Fu, S. Wang, Mater. Chem. Front. 2020, 4, 140.

[146] S. J. Lee, S. Lee, K. H. Kang, Appl. Phys. Lett. 2012, 100, 081604.

[147] S. Wilderman, C. Sun, Soft Matter 2016, 12, 9622.

[148] W. Hou, Y. Wang, Y. Bian, J. Zhang, S. LI, Y. Zeng, X. Du, Z. Gu, ACS Appl. Mater. Interfaces 2020, 3, 2230.

[149] T. Nakata, N. Phillips, P. Simões, P. J. Russell, J. A. Cheney, S. M. Walker, R. J. Bomphrey, Sci. Adv. 2020, 368, 634.

[150] N. Namdari, B. Mohammadian, P. Jafari, R. Mohammadi, H. Sojoudi, H. Ghasemi, R. Rizvi, Mater. Horiz. 2020, 7, 366.

[151] Y. Chen, J. Meng, Z. Gu, X. Wan, L. Jiang, Adv. Func. Mater. 2020, 30, 1905287.

[152] Y. Zhang, J. Mei, C. Yan, T. Liao, J. Bell, Z. Sun, Adv. Mater. 2020, 32, 1902806.

[153] H. Watanabe, A. Fujimoto, A. Takahara, Soft Matter 2011, 7, 1856.

[154] Y. Zhou, S. Huang, X. Tiang, Adv. Func. Mater. 2020, 30, 1906507.

[155] S. Huang, J. Li, L. Liu, L. Zhou, X. Tian, Adv. Mater. 2019, 31, 1901417.

[156] J. Li, Q. H. Qin, A. Shah, R. H. A. Ras, X. Tian, V. Jokinen, Sci. Adv. 2016, 2, e1600148.

[157] V. R. Stamenkovic, D. Strmcnik, P. P. Lopes, N. M. Markovic, Nat. Mater. 2016, 16, 57.

[158] H. Yang, F. Liang, Y. Chen, Q. Wang, X. Qu, Z. Yang, NPG Asia Mater. 2015, 7, e176.

[159] J. G. Leidenfrost, Duisburg, 1756.

[160] A. Y. Stark, I. Badge, N. A. Wucinich, T. W. Sullivan, P. H. Niewiarowski, A. Dhinojwala, Proc. Natl. Acad. Sci. U. S. A, 2013, 110, 6340.

[161] K. Meister, S. Strazdaite, A. L. DeVries, S. Lotze, L. L. Olijve, I. K. Voets, H. J. Barker, Proc. Natl. Acad. Sci. U. S. A. 2014, 111, 17732.

[162] X. Gao, X. Yan, X. Yao, L. Xu, K. Zhang, J. Zhang, B. Yang, L. Jiang, Adv. Mater. 2007, 19, 2213.

[163] F. Geyer, M. D'Acunzi, A. Sharifi-Aghili, A. Saal, N. Gao, A. Kaltbeitzel, T.-F. Sloot, R. Berger, H.-J Butt, D. Vollmer1, Sci. Adv. 2020, 6, eaaw9727.

[164] D. Wang, Q. Sun, M. J. Hokkanen, C. Zhang, F.-Y. Lin, Q. Liu, S.-P. Zhu, T. Zhou, Q. Chang, B. He, Q. Zhou, L. Chen, Z. Wang, R. H. A. Ras, X. Deng, Nature 2020, 582, 55.

[165] T. L. Liu, J. C. Kim, Science 2014, 346, 1096.

[166] M. Schaffner, J. A. Faber, L. Pianegonda, P. A. Rühs, F. Coulter, A. R. Studart, Nat. Commun. 2018, 9, 878.

[167] A. Miriyev, K. Stack, H. Lipson, Nat. Commun. 2017, 8, 596.

[168] Y. Alapan, O. Yasa, O. Schauer, J. Giltinan, A. F. Tabak, V. Sourjik, M. Sitti, Sci. Robotics. 2018, 3, eaar4423.

[169] C. G. Núñez, L. Manjakkal, R. Dahiya, npj Flexible Electronics 2019, 3, 1.

[170] P. Trogadas, M.-O. Coppens, Chem. Soc. Rev. 2019.

[171] W. Xu, H. Zheng, Y. Liu, X. Zhou, C. Zhang, Y. Song, X. Deng, M. Leung, Z. Yang, R. X. Xu, Z. Lin Wang, X. C. Zeng, Z. Wang, Nature 2020, 578, 392.

[172] Z. Zhang, L. He, C. Zhu, Y. Qian, L. Wen, L. Jiang, Nat. Commun. 2020, 11, 875.

[173] P. S. Owuor, S. Hiremath, A. C. Chipara, R. Vajtai, J. Lou, D. R. Mahapatra, C. S. Tiwary, P. M. Ajayan, Adv. Mater. Interfaces 2017, 1700240.

[174] M. Liu, S. Wang, L. Jiang, Nat. Rev. Mater. 2017, 2, 17036.

[175] Z. Ashrafi, L. Lucia, W. Krause, ACS Appl. Mater. Interfaces 2019, 11, 21275.

[176] T.-S. Wong, S. H. Kang, S. K. Y. Tang, E. J. Smythe, B. D. Hatton, A. Grinthal, J. Aizenberg, Nature 2011, 477, 443.

[177] X. Rong, R. Ettelaie, S. V. Lishchuk, H. Cheng, N. Zhao, F. Xiao, F. Cheng, H. Yang, Nat. Commun. 2019, 10, 1854.

[178] M. Cui, B. Wang, Z. Wang, Adv. Eng. Mater. 2019, 21, 1801379.

[179] A. Gauthier, C. Diddens, R. Proville, D. Lohse, D. van der Meer, Proc. Natl. Acad. Sci. U. S. A, 2018, 116, 1174.

[180] L. E. Dodd, D. Wood, N. R. Geraldi, G. G. Wells, G. McHale, B. B. Xu, S. Stuart-Cole, J. Martin, M. I. Newton, ACS Appl. Mater. Interfaces 2016, 8,22658.

[181] S. Huang, Y. Zhang, J. Shi, W. Huang, ACS Sustainable Chem. Eng. 2016, 4, 676.

[182] F. Geyer, Y. Asaumi, D. Vollmer, H.-J. Butt, Y. Nakamura, S. Fujii, Adv. Func. Mater. 2019, 29, 1808826.

[183] S. Feng, Q. Wang, Y. Xing, Y. Hou, Y. Zheng, Adv. Mater. Interfaces 2020.7, 2000081.

[184] X. Liu , H. Gu , M. Wang , X. Du , B. Gao , A. Elbaz , L. Sun , J. Liao , P. Xiao, Z. Gu , Adv. Mater., 2018, 30 , 1800103

[185] Y. Zuo, L. Zheng, C. Zhao, H. Liu, Small 2020, 16, 1903849.

[186] X. Dai, N. Sun, S. O. Nielsen, B. B. Stogin, J. Wang, S. Yang, T.-S. Wong, Sci. Adv. 2018, 4, eaaq0919.

[187] A. Noojoomi, H. Arslan, K. Lee, K. Yum, Nat. Commun. 2018, 9, 3705.

[188] M. Humood, Y. Shi, M. Han, J. Lefebvre, Z. Yan, M. Pharr, Y. Zhang, Y. Huang, J. A. Rogers, A. A. Polycarpou, Small 2018, 14, 1703852.

[189] S. Peppou-Chapman, J. K. Hong, A. Waterhouse, C. Neto, Chem. Soc. Rev. 2020, 49, 3688.

[190] H. Y. Erbil, Surf. Sci. Rep. 2014, 69, 325.

[191] X. Xia, C. He, P. Zhang, Proc. Natl. Acad. Sci. U. S. A. 2019, 116, 23467.

[192] K. Liu, J. DU, J. Wu, L. Jiang, Nanoscale 2012, 4, 768.

[193] C. Farber, R. Wang, R. Chemelewski, J. Mullet, D. Kurouski, Anal. Chem. 2019, 91, 2472.

[194] W. Liu, S. Xiang, X. Liu, B. Yang, ACS Nano 2020, 14, 9166.

[195] L. Lin, M. Liu, L. Chen, P. Chen, J. Ma, D. Han, L. Jiang, Adv. Mater. 2010, 4826.

[196] Y. F. Fu, C. Q. Yuan, X. W. Bai, Biosurf. Biotribology 2017, 3, 11.

[197] R. Deng, T. Shen, H. Chen, J. Lu, H.-C. Yang, W. Li, J. Mater. Chem. A 2020, 8, 7536.

[198] S. K. Ujjain, P. K. Roy, S. Kumar, S. Singha, K. Khare, Sci. Rep. 2016, 6, 35524.

[199] P. Ge, S. Wang, J. Zhang, B. Yang, Mater. Horiz. 2020.

[200] C. Shan, J. Yong, Q. Yang, F. Chen, J. Huo, J. Zhuang, Z. Jiang, X. Hou, AIP Adv. 2018, 8, 045001.

[201] S. Parvate, P. Dixit, S. Chattopadhyay, J. Phys. Chem. B 2020, 124, 1323.

[202] Z. Zhao, C. Ling, D. Wang, J.-X. Wang, J. Saczek, S. Pramana, S. Sridhar, J. Shang, B. B. Xu, D. C. W. Tsang, J.-F. Chen, S. Wang, Small 2020.

[203] Z. Li, Y. Liu, M. Lei, A. Sun, S. Sridhar, Y. Li, X. Liu, H. Lu, Y. Q. Fu, B. B. Xu, Soft Matter 2020, 16, 1636.

[204] R. Michel, L. Poirier, Q. V. Poelvoorde, J. Legagneux, M. Manassero, L. Corte, Proc. Natl. Acad. Sci. U. S. A. 2019, 116, 738.

[205] Y. C. Wu, K. S. Liu, B. Su, L. Jiang, Adv. Mater. 2014, 26, 1124.

[206] C. Buten, L. Kortekaas, B. J. Ravoo, Adv. Mater. 2020, 32, 1904957.

[207] M. Kaganyuk, A. Mohraz, Langmuir 2019, 35, 12807.

[208] M. Wei, Y. Song, Y. Zhu, D. J. Preston, C. S. Tan, E. N. Wang, Appl. Phys. Lett. 2020, 116, 233703.

[209] B. S. Kim, B. I. Lee, N. Lee, G. Choi, T. Gemming, H. H. Cho, Sci. Rep. 2017, 7, 45323.

[210] M. Michalska-Domanska, W. J. Stepniowski, L. R. Jaroszewicz, J. Porous Mater. 2017, 24, 779.

[211] M. H. Lee, N. Lim, D. J. Ruebusch, A. Jamshidi, R. Kapadia, R. Lee, T. J. Seok, K. Takei, K. Y. Cho, Z. Y. Fan, H. Jang, M. Wu, G. J. Cho, A. Javey, Nano. Lett. 2011, 11, 3425.

[212] M. K. Kushwaha, Procedia Mater. Sci. 2014, 5, 1266.

[213] K. H. Rashid, A. A. Khadom, H. B. Mahood, Met. Mater. Int. 2020.

[214] K. Schwirn, W. Lee, R. Hillebrand, M. Steinhart, K. Nielsch, U. Gosele, ACS Nano 2008, 2, 302.

[215] V. Jothi, A. Y. Adesina, A. M. Kumar, J. S. N. Ram, Met. Mater. Int. 2019, 1.

[216] R. Elaish, M. Curioni, K. Gowers, A. Kasuga, H. Habazaki, T. Hashimoto, P. Skeldon, Electrochem. Acta 2017, 245, 854.

[217] S. Shrestha, B. D. Dunn, Surf. Eng. Light Alloys 2010, 603.

[218] H. Asoh, K. Asakura, H. Hashimoto, RSC Adv. 2020, 10, 9026.

[219] A. B. Rogov, A. Yerokhin, A. Matthews, Langmuir 2017, 33, 11059.

[220] Y. Lin, Q. Lin, X. Liu, Y. Gao, J. He, W. Wang, Z. Fan, Nanoscale Res. Lett. 2015, 10, 495.

[221] W. Lee, S.-J. Park, Chem. Rev. 2014, 114, 7487.

[222] S. Z. Chu, K. Wada, S. Inoue, M. Isogai,Y. Katsuta, A. Yasumori, J. Electrochem. Soc. 2006, 153, B384.

[223] J. F. Murphy, C. E. Michelson, Proc. Of Anodizing Aluminum 1961, 83.

[224] G. E. Thompson, R. C. Furneaux, G. C. Wood, Corros. Sci. 1978, 18, 481

[225] Z. Yao, Q. Xia, P. Ju, J. Wang, P. Su, D. Li, Z. Jiang, Sci. Rep. 2016, 1.

[226] W. Shang, F. Wu, Y. Wang, A. R. Baboukani, Y. Wen, J. Jiang, ACS Omega 2020, 5, 7262.

[227] V. P. Vavilov, S. Marinetti, F. Cernuschi, D. Roba, Russian J. Nondestruc. Testing 2005, 41, 466.

[228] R. Darolia, Int. Mater. Rev. 2013, 58, 1.

[229] G. Kaur, A. marmur, S. Magdassi, Additive Manufacturing 2020, 101669.

[230] Z. Dong, M. F. Schumann, M. J. Hokkanen, B. Chang, A. Welle, Q. Zhou, R. H. A. Ras, Z. Xu, M. Wegener, P. A. Levkin, Adv. Mater. 2018, 30, 1803890.

[231] V. Liimatainen , M. Vuckovac , V. Jokinen , V. Sariola , M. J. Hokkanen , Q. Zhou and R. H. A. Ras , Nat. Commun. 2017, 8 , 1798. [232] Y. Li, H. Mao, P. Hu, M. Hermes. H. Lim, J. Yoon, M. Luhar, Y. Chen, W. Wu, Adv. Mater. Technol. 2019, 4, 1800638.

[233] G.-T. Yun, W.-B. Jung, M. S. Oh, G. M. Jang, J. Baek, N. I. Kim, S. Gap Im, H.-T. Jung, Sci. Adv. 2018, 4, eaat4978.

[234] G. Mondin, B. Schumm, J. Fritsch, R. Hensel, J. Grothe, S. Kaskel, Mater. Chem. Phys., 2013, 137, 884.

[235] H. Li, F.-H. Chen, S. Biria, I. D. Hosein, Adv. Eng. Mater. 2019, 21, 1801150.

[236] Y. Cai , L. Lin , Z. X. Xue , M. J. Liu , S. T. Wang, L. Jiang, Adv. Funct. Mater., 2014, 24, 809.

[237] H. B. Jo , J. Choi , K. J. Byeon , H. J. Choi, H. Lee, Microelectron. Eng. 2014, 116, 51.

[238] H. F. Bohn, W. Federle, Proc. Natl. Acad. Sci. U. S. A. 2004, 101, 14138.

[239] C. Zhou, Z. Chen, H. Yang, K. Hou, X. Zeng, Y. Zheng, J. Cheng, ACS Appl. Mater. Interfaces 2017, 9, 9184.

[240] K. Liu, L. Jiang, Ann. Rev. Mater. Res. 2012, 42, 231.

[241] M. I. Jamil, A. Ali, F. Haq, Q. Zhang, X. Zhan, F. Chen, Langmuir 2018, 34, 15425.

[242] T. Mouterde, G. Lehoucq, S. Xavier, A. Checco, C. T. Black, A. Rahman, T. Midavaine, C. Clanet, D. Quéré, Nat. Mater. 2017, 16, 658.

[243] M. Cui, B. Wang, Z. Wang, Adv. Eng. Mater. 2019, 21, 1801379.

[244] X. Yao, Y. Hu, A. Grinthal, T.-S. Wong, L. Mahadevan, J. Aizenberg, Nat. Mater. 2013, 12, 529.

[245] A. B. Nordvik, J. L. Simmons, K. R. Bitting, A. Lewis, T. Strøm-Kristiansen, Spill. Sci. Technol. Bulletin 1996, 3, 107.

[246] J. Jiang, J. Gao, H. Zhang, W. He, J. Zhang, D. Daniel, X. Yao, Proc. Natl. Acad. Sci. U. S. A. 2019, 116, 2482.

[247] M. Liu, S. Wang, Z. Wei, Y. Song, L. Jiang, Adv. Mater. 2009, 21, 665.

[248] P. R. Waghmare, N. S. K. Gunda, S. K. Mitra, Sci. Rep. 2015, 4, 7454.

[249] L. Lao, D. Shou, Y. S. Wu, J. T. Fan, Sci. Adv. 2020, 6, eaaz0013.

[250] A. Owais, T. Smith-Palmer, A. Gentle, C. Neto, Soft Matter 2018, 14, 6627.

[251] Z. Li, Y. Liu, M. Lei, A. Sun, S. Sridhar, Y. Li, X. Liu, H. Lu, Y. Q. Fu, B. B. Xu, Soft Matter 2020, 16, 1636.

[252] B.-Y. Lee, D. H. Kim, J. Park, K.-I. Park, K. J. Lee, C. K. Jeong, Sci. Technol. Adv. Mater. 2019, 20, 758.

[253] T. B. H. Schroeder, A. Guha, A. Lamoureux, G. VanRenterghem, D. Sept, M. Shtein, J. Yang, M. Mayer, Nature 2017, 552, 214.

[254] W. Xu, H. Zheng, Y. Liu, X. Zhou, C. Zhang, Y. Song, X. Deng, M. Leung, Z. Yang, R. X. Xu, Z. L. Wang, X. C. Zeng, Z. Wang, Nature 2020, 578, 392.

[255] J. Nie, Z. Wang, Z. Ren, S. Li, X. Chen, Z. L. Wang, Nat. Commun. 2019, 10, 2264.

[256] S. H. Kim, H. J. Sim, J. S. Hyeon, D. Suh, G. M. Spinks, R. H. Baughmanm, S. J. Kim, Sci. Rep. 2018, 8, 8712.

[257] X.-Q. Wang, C. F. Tan, K. H. Chan, X. Lu, L. Zhu, S.-W. Kim, G. W. Ho, Nat. Commun. 2018, 9, 3438.

[258] P. Irajizad, M. Hasnain, N. Farokhnia, S. M. Sajadim, H. Ghasemi, Nat. Commun. 2016, 7, 13395.

[259] J. Chen, R. Dou, D. Cui, Q. Zhang, Y. Zhang, F. Xu, X. Zhou, J. Wang, Y. Song, L. Jiang, ACS Appl. Mater. Interfaces 2013, 5, 4026.

[260] J. Chen, K. Li, S. Wu, J. Liu, K. Liu, Q. Fan, ACS Omega 2017, 2, 2047.

[261] D. Rus, M. T. Tolley, Nature 2015, 521, 465.

[262] S. Kim, C. Laschi, B. Trimmer, Trends Biotechnol. 2013, 31, 287.

[263] M. Cianchetti, C. Laschi, A. Menciassi, P. Dario, Nat. Rev. Mater. 2018, 3, 143.

[264] H. Lu, M. Zhang, Y. Yang, Q. Huang, T. Fukuda, Z. Wang, Y. Shen, Nat. Commun. 2018, 9, 3944.

[265] Y. Tang, Y. Chi, J. Sun, T.-H. Huang, O. H. Maghsoudi, A. Spence, J. Zhao, H. Su, J. Yin, Sci. Adv. 2020, 6, eaaz6912.

[266] I. Must, E. Sinibaldi, B. Mazzolai, Nat. Commun. 2019, 10, 344.

[267] M. Rogoz, H. Zeng, C. Xuan, D. S. Wiersma, P. Wasylczyk, Adv. Opt. Mater. 2016, 4, 1689.

[268] N. Miljkovic, D. J. Preston, R. Enright, E. N. Wang, Nat. Commun. 2013, 4, 2517.

[269] L. Xue, A. Kovalev, A. Eichler-Volf, M. Steinhart, S. N. Gorb, Nat. Commun. 2015, 6, 6621.

[270] K. Huang, P. Rowe, C. Chi, V. Sreepal, T. Bohn, K.-G. Zhou, Y. Su, E. Prestat, P. Balakrishna Pillai, C. T. Cherian, A. Michaelides, R. R. Nair, Nat. Commun. 2020, 11, 1097.

[271] Y. Wang, S. Gao, W. Xu, Z. Wang, Adv. Func. Mater. 2020, 30, 1908252.

[272] X. Hou, Y. S. Zhang, G. Trujillo-de Santiago, M. M. Alvarez, J. Ribas, S. J. Jonas, P. S. Weiss, A. M. Andrews, J. Aizenberg, A. Khademhosseini, Nat. Rev. Mater. 2017, 2, 17016.

[273] Q. Li, Z. Guo, J. Mater. Chem. B. 2018, 6, 13549.

[274] H. Chen, T. Ran, Y. Gan, J. Zhou, Y. Zhang, L. Zhang, D. Zhang, L. Jiang, Nat. Mater. 2018, 17, 935.

[275] S.A. Kulinich, M. Honda, A.L. Zhu, A.G. Rozhinb, X.W. Du, The icephobic performance of alkyl-grafted aluminum surfaces, Soft Matter 2015, 11, 856-861.

[276] Z. J. Wang, W. Hong, Z. L. Wu, Q. Zheng, Angew. Chem., Int. Ed. Engl. 2017, 56, 15974.

[277] S. Y. Zheng, Y. Shen, F. Zhu, J. Yin, J. Qian, J. Fu, Z. L. Wu, Q. Zheng, Adv. Funct. Mater. 2018, 28, 1803366.

[278] B. B. Xu, Q. Liu, Z. Suo, R. C. Hayward, Adv. Funct. Mater. 2016, 26, 3218.

[279] S. Park, D. Kim, S. Y. Ko, J.-O. Park, S. Akella, B. Xu, Y. Zhang, S. Fraden, Lab Chip 2014, 14, 1551.

[280] Y. Li, D. Wang, J. Richardson, B. B. Xu, Macromol. Symposia 2017, 372, 127.

APPENDIX

Recent publications and related award certifications are present in this section.

Please see next pages for detail

SCI
where science meets business

This is to certify that on 7 September 2018

Sreepathy Sridhar

was awarded the

Joint Third Prize
Oral Presentation

for

Excellence in Chemical Research

at the 25th Annual SCI-CSCST Conference
of the SCI Chinese UK Group and
the Chinese Society of Chemical Science & Technology in the UK

Weiping Wu

Weiping Wu
Chair, SCI Chinese UK Group

Sharon Todd
Executive Director, SCI

Society of Chemical Industry
International Headquarters, 14/15 Belgrave Square, London, SW1X 8
T: +44 (0)20 7598 1500 F: +44 (0)20 7598 1545 www.soci.org

Surface & Coatings Technology 408 (2021) 126809

Contents lists available at ScienceDirect

Surface & Coatings Technology

journal homepage: www.elsevier.com/locate/surfcoat

A highly controlled fabrication of porous anodic aluminium oxide surface with versatile features by spatial thermo-anodization

Zhehui Zhang [a,1], Sreepathy Sridhar [b,1], Guoying Wei [a,*], Yundan Yu [a], Zhongquan Zhang [a], Li Jiang [a], Yumeng Yang [a], Muhammad Wakil Shahzad [b], Xue Chen [b], Ben Bin Xu [a,b,*]

[a] College of Materials & Chemistry, China Jiliang University, Hang Zhou 310018, PR China
[b] Department of Mechanical and Construction Engineering, Faculty of Engineering and Environment, Northumbria University, Newcastle upon Tyne NE1 8ST, UK

ARTICLE INFO

Keywords:
Anodic oxidation
Solar absorptivity
Emittance
Surface wetting
Anti-freezing

ABSTRACT

Thermo-anodization technology has been considered as an effective means to improve the thermal, physical and chemical properties for metal alloy. In this work, we achieve a porous black layer on the surface of aluminium alloy through an environmentally friendly anodic oxidation process, with a high thermal emittance (0.96) and a high solar absorptivity (0.921). In addition, the black thermo-anodized coating layer shows a unique anti-corrosion property under UV irradiation. A hybrid hydrophobic surface has been facilitated through treating the thermo-anodized porous layer with silane. Moreover, an anti-icing feature can be realised that can effectively delay the freezing of water droplet on the surface of AA2024 aluminium alloy. As such, the specific anodic process of coating provides a simple method for improving the solar absorptivity and infrared emittance of aluminium alloys, enabling broad applications in aerospace engineering.

1. Introduction

Controllable thermo-anodized coating (CTC) with a passive and effective protection to a spacecraft, has attracted considerable research interests in recent years [1–3]. Such coatings have been widely used in the electronic housing packages of spacecraft with black CTC on the alloys, to fulfil high solar absorptivity and high emittance. Recently, the demand of these coatings climbs in response to the growing applications in aerospace engineering [4–9], where the common technical focuses are to develop CTC surfaces with resistance against corrosion [10] and icing [11], as well as high solar absorptivity (a_s) [12] and thermal emittance (ε) [13]. Some mechanisms have been proposed to achieve controlled oxidation on alloys [14] and Plasma Electrolytic Oxidation (PEO) [15]. Yao et al prepared a black high-solar-absorptivity and high-emittance coating on titanium alloy with a a_s of 0.93 and ε of 0.88 [16]. Shang et al used micro-arc oxidation to prepare a multi-layered GO coated Magnesium alloy with an improved corrosion resistance [17]. While the coating technology on the surfaces of titanium and magnesium alloys advances [18–20], their anti-corrosion performance declines at the presence of solar light [21–24]. Anodic aluminium alloys manufactured via traditional anodization methods exhibits mild anti-corrosion behaviour with reduced solar absorptivity and thermal emittance [25–27]. Hence, a conventional process to achieve high performance CTC coated Aluminium alloy has not been exploited elsewhere.

In this paper, we propose a conventional CTC strategy on the surface of aluminium alloys. The combination of anodic current density and temperature accelerate the anodization process without the need for involvement of changes to electrolyte concentration and provide controllability over the porous structure formation on the anodized aluminium oxide surface [28]. The as-prepared coating layer presents an excellent property with both absorptivity and emittance values above 0.9. The surface microstructure of coating layer can be adjusted by changing the anodizing temperature and current density. The fabricated black CTC possess a unique anti-corrosion property under UV irradiation. By constructing a hybrid layer with a silanization process, an improved anti-icing property can be facilitated by delaying the frozen time for the water droplet on the surface of AA2024 aluminium alloy.

* Corresponding authors at: College of Materials & Chemistry, China Jiliang University, Hang Zhou 310018, PR China; Department of Mechanical and Construction Engineering, Faculty of Engineering and Environment, Northumbria University, Newcastle upon Tyne NE1 8ST, UK.
E-mail addresses: guoyingwei@cjlu.edu.cn (G. Wei), ben.xu@northumbria.ac.uk (B.B. Xu).
[1] Authors with equal contribution.

https://doi.org/10.1016/j.surfcoat.2020.126809
Received 6 September 2020; Received in revised form 18 December 2020; Accepted 21 December 2020
Available online 6 January 2021

ADVANCED MATERIALS INTERFACES
www.advmatinterfaces.de

Controlled Cooperative Wetting Enabled Heterogeneous Structured 3D Morphing Transducers

*Sreepathy Sridhar, Cong Wang, Jonathan G. Terry, Xue Chen, Ansu Sun, Zhenghong Li, Haibao Lv, Ben Bin Xu, and Yifan Li**

A unique microfluidics approach for functional hydrogel patterning with multilayered heterogeneous structures is presented. Prepolymer solution droplets with differentiated sodium acrylate concentrations are dispensed/printed in a wetting-controlled "two-parallel plate" (TPP, like a Hele-Shaw Cell) system. The gelation within the system enables hydrogel bilayer structures with reconfigurable 3D deformations driven by in-plane and through-thickness heterogeneity under stimuli-responsive mask-less swelling/deswelling. The cooperation between swelling mismatch of functional groups results in a higher complexity of 3D reconfiguration in responding to discrete levels of stimulation inputs. This facile patterning technology with an in-built ionic hierarchy can be scaled up/down with advanced transducing functionalities in various fields.

1. Introduction

Inspired by nature,[1–3] morphing soft materials responding to external stimulation (e.g., electrical, mechanical, and chemical) has proven to exhibit applicability in various fields,[4–9] but not restricted to flexible electronics,[10,11] 4D printing,[12,13] biomedical transducers,[14] and soft robotics.[15,16] One of the desirable developments is to make the morphing process programmable[17–22] and reversible[23,24] through structured soft functional materials, which enable effective shape configuration design according to the applications. As one of the popular candidates, hydrogels have drawn more significant attentions due to their open network structures, and ability to generate large changes[25,26] (therefore high deformation) in volume responding to various external stimulation. For example, by creating through-thickness,[20] in-plane gradient,[27] or combining the two[28] in structuring dissimilar hydrogel functional layers and blocks, controllable deformation such as bending and folding can be achieved.

The through-thickness gradient approach typically employs a hydrogel bilayer structure where the swelling behavior remains dissimilar across the thickness.[8] The differential swelling leads to internal stress mismatch and influence out-of-plane 3D morphing configurations, resulting a single configuration at certain external conditions (e.g., temperature, ion concentration).[16] When external conditions are altered, a wider range of deformation magnitude and/or a reversed shape (e.g., bending towards opposite direction, "C" becomes "Ↄ") can be achieved, and more complicated configurations can be accomplished via advanced 2D shape patterning.[8,21,29] On the other hand, the in-plane gradient approach typically employs 2D heterogeneity via a single layer of patterned functional hydrogel on the same plane, resulting in a bistable status where the buckling could happen in either directions.[16] Combining the ideas from both through-thickness and in-plane gradient modes, through a controlled "preswelling" process that determines swelling direction, programmable complex deformations were demonstrated by the "site-specific" patterned hydrogel blocks.[17,27] The resultant shape-morphing structure generated due to in-plane elastic mismatch between nonswelling substrate and controlled swellable gel blocks was more or less fixed.[17,27] Moreover, such an approach always requires pairs of silhouetted/holed "preswelling masks" to assist and orchestrate the swelling command, in order to reconfigure the deformation patterns.[16,17] Also, once deformed, it will be difficult/impossible to apply the silhouetted/holed mask again to reconfigure the shape. For the required bilayer system, thickness uniformity is important due to its role in initiating the inherent stress distribution. For homogeneous hydrogel single-layer structures, patterned or not, this can be achieved by spin coating, or molding the prepolymer hydrogel (pre-gel) in a "two-parallel plate" (TPP, like a Hele-Shaw cell) configuration, followed by gelation processes.[8,30] Inspired by natural biostructures, a single layer of encoded heterogeneous hydrogel building blocks has been exploited to form hierarchical complex hydrogel architectures, using droplet microfluidics (DMF) surface wetting control to guide the gel formation.[31]

S. Sridhar, Dr. C. Wang, Dr. X. Chen, A. Sun, Prof. B. B. Xu, Dr. Y. Li
Mechanical and Construction Engineering
Faculty of Engineering and Environment
Northumbria University
Newcastle upon Tyne NE1 8ST, UK
E-mail: yifan.li@northumbria.ac.uk

Dr. J. G. Terry
School of Engineering
Institute for Integrated Micro and Nano Systems
University of Edinburgh
Edinburgh EH9 3JF, UK

Z. Li, Prof. H. Lv
Science and Technology on Advanced Composites in Special Environments Laboratory
Harbin Institute of Technology
Harbin 150080, P. R. China

The ORCID identification number(s) for the author(s) of this article can be found under https://doi.org/10.1002/admi.202001211.

DOI: 10.1002/admi.202001211

ADVANCED MATERIALS INTERFACES
www.advmatinterfaces.de

Biaxially Morphing Droplet Shape by an Active Surface

Ding Wang, Yingzhi Liu, Sreepathy Sridhar, Yifan Li, Glen McHale, Haibao Lu, Ziyi Yu, Steven Wang,* and Ben Bin Xu**

Drop morphology can be manipulated by designing localized solid/liquid interactions to create a favorable interfacial energy equilibrium. A topographical surface with hierarchical roughness can be harnessed to generate complex drop morphologies, enhance uniaxial and anisotropic spreading, in a designable fashion. Here, using an active surface is proposed with a responsive roughness (wrinkle patterns) under uniaxial compression/stretching, to morph droplet shape biaxially in a continuous and reversible manner. The keys to achieve biaxial drop shaping are the in-plane confinement from lattice hole patterns and the programmable formation of roughness, to pin and guide contact line movement in both in plane directions. The complex interplay between wetting and the patterns is elucidated by both experiments and numerical analysis. The results enrich the current understanding of shaping droplets by managing the contact line pinning/movement on an engineered elastic substrate, and providing insights for emerging applications in the areas such as droplet emicrofluidics, liquid robotics, ink-jet printing, 3D printing and healthcare.

Dr. D. Wang, Y. Liu, S. Sridhar, Dr. Y. Li, Prof. G. McHale, Prof. B. B. Xu
Smart Materials and Surfaces Laboratory
Faculty of Engineering and Environment
Northumbria University
Newcastle upon Tyne NE1 8ST, UK
E-mail: ben.xu@northumbria.ac.uk

Y. Liu, Prof. H. Lu
Science and Technology on Advanced Composites in Special Environments Laboratory
Harbin Institute of Technology
Harbin 150080, China

Prof. G. McHale
School of Engineering
University of Edinburgh
Edinburgh EH9 3JL, UK

Prof. Z. Yu
State Key Laboratory of Materials-Oriented Chemical Engineering
College of Chemical Engineering
Nanjing Tech University
Nanjing 211816, China
E-mail: ziyi.yu@njtech.edu.cn

Dr. S. Wang
Department of Mechanical Engineering
City University of Hong Kong
Hong Kong
E-mail: steven.wang@cityu.edu.hk

The ORCID identification number(s) for the author(s) of this article can be found under https://doi.org/10.1002/admi.202001199.

DOI: 10.1002/admi.202001199

Surfaces with controllable wetting properties are of great potential in downstream applications such as water harvesting,[1,2] self-cleaning,[3–5] surface coating,[6,7] adhesion[8–10] and microfluidic devices.[11–14] One strategy to facilitate controllable surface wetting is to develop surface topographies,[15–17] thereby enabling a desired liquid/solid interaction.[18–21] Recent advances have brought diverse approaches to create specific wetting performance by using chemical treatment,[22–24] dedicated pattern designs,[25–27] and functional materials.[28,29] Notably, Quéré and co-workers[16] manipulated the droplet shape on an elastic surface with soft pillars. Park and Kim used a shape memory polymer-based structure to shape droplets with adjustable surface morphology.[30] To date, the quest to achieve controllable surface wetting in a low cost, reliable and highly efficient fashion remains ongoing.

Recently, researchers developed strategies to control surface capillarity by creating surface wrinkles[31–33] and programmable surface roughness.[34–36] Designable wrinkle patterns with morphological transitions of periodicity, amplitude, and orientation under mechanical stimuli can enable a wetting anisotropy.[37–39] Some studies have investigated the wrinkling induced surface energy barriers and the associated contact line pinning. Stafford et al.[40] studied the wetting transitions upon a tunable single-period micro-wrinkled surfaces. Yang et al.[41] investigated the influences of wrinkle groove geometry on anisotropic wetting with a combining force balanced model. Feng et al.[42] reported anisotropic wetting on hierarchical wrinkled surfaces induced by curvature. Some of our authors explored the autonomous change of surface wetting by generating responsive wrinkle-cracking morphology on a gold/shape memory polymer bilayer.[43] However, the above studies focus on shaping droplets in one direction and the challenges on shaping a droplet bi-axially in a continuous, dynamic and reversible manner remain yet to be tackled.

In this work, we describe an approach to program a droplet from a circular shape to an ellipsoidal shape biaxially, upon a morphing surface consisting of a topographic lattice pattern and a stimuli-responsive roughness. Under uniaxial mechanical stimuli, localized wrinkle patterns can be initiated to create hierarchical structures on the surface selectively, yielding an enhanced pinning effect to pin and guide the movement of contact line. An analytical study is performed to understand the impact from surface geometries on droplet shaping. By varying

NANO · MICRO small
www.small-journal.com

Liquid Marbles in Liquid

Zhijian Zhao, Chen Ling, Dan Wang, Jie-Xin Wang, Joshua Saczek, Stevin Pramana, Sreepathy Sridhar, Jin Shang, Ben B. Xu,* Daniel C. W. Tsang, Jian-Feng Chen, and Steven Wang**

Traditional liquid marbles (LMs), liquid droplets encapsulated by hydrophobic particles at the liquid–gas interface, are restricted by their short lifetime and low heat transfer efficiency. Herein, a new paradigm for LMs immersed in various liquid mediums with massive enhanced heat transfer and spatial recognition is designed; without compromising the structural integrity, the lifetime of the liquid marbles in liquid (LMIL) is extended by ≈1000 times compared to classical LMs in air or naked droplets in organic reagents. The LMIL shows promising reverse structural re-configurability while under external stimuli and maintaining their functionality for a very long period of time (≈weeks). These superior behaviors are further exploited as a miniature reactor with prolonged lifetimes and excellent temperature control, combined with its feasible operation, new opportunities will open up in the advanced chemical and biomedical engineering fields. It is also shown that LMIL can be applied in methylene blue degradation and 3D in-vitro yeast cell cultures. These findings have important implications for real-world use of LMs, with a number of applications in cell culture technology, lab-in-a-drop, polymerization, encapsulation, formulation, and drug delivery.

Liquid marbles (LMs) are liquid droplets encapsulated by hydrophobic particles at the liquid–gas interface; this phenomena has recently drawn increasing interest due to their superior mobility,[1–4] elasticity,[5] and stability.[6,7] These beneficial characteristics have allowed LMs to be successfully applied as microreactors,[8–11] in microfluidic control,[12–15] gas sensing, and many other engineering areas.[16–19] Compared with the uncoated "naked" droplets, LMs can be manipulated as non-sticky fluidic cells with significantly reduced surface friction and increased drop operability.[20–22] Based on the nature of the internal fluid and variations of physical properties of coated particles, external stimuli such as electric field,[23–26] photon, visible light,[27] magnetic field,[28,29] and mechanical force[30–32] can be used to manipulate the LMs' properties. In addition, LMs with shells composed of multilayers of particles can be engineered for precise control of chemical dosing by allowing them to coalesce and disintegrate at specific interval.[7,33] The combination of simple manipulation, accurate control, and overarching benefits of microreactors give LMs promising advantages in both chemical analysis and biomedical applications.

The hydrophobic shell is the essential building block of LMs that generate many of their benefits, for example, it prevents the direct contact between the internal liquid and the wetting surface.[34–37] The porous shell also allows for the mass transfer of gas/vapor in and out of the LM, making it possible for use as gas sensors[38,39] and gas–liquid microreactors.[40] Although

Z. Zhao, Prof. D. Wang, Prof. J.-X. Wang, Prof. J.-F. Chen
State Key Laboratory of Organic Inorganic Composites
Beijing University of Chemical Technology
Beijing 100029, China
E-mail: wangdan@mail.buct.edu.cn

C. Ling, Dr. S. Wang
Department of Mechanical Engineering
City University of Hong Kong
Hong Kong 999077, China
E-mail: steven.wang@cityu.edu.hk

J. Saczek, Dr. S. Pramana
School of Engineering
Newcastle University
Newcastle upon Tyne NE1 7RU, UK

S. Sridhar, Prof. B. B. Xu
Department of Mechanical and Construction Engineering
Faculty of Engineering and Environment
Northumbria University
Newcastle upon Tyne NE1 8ST, UK
E-mail: ben.xu@northumbria.ac.uk

Dr. J. Shang
School of Energy and Environment
City University of Hong Kong
Hong Kong 999077, China

Prof. D. C. W. Tsang
Department of Civil and Environmental Engineering
The Hong Kong Polytechnic University
Hung Hom, Kowloon, Hong Kong 999077, China

The ORCID identification number(s) for the author(s) of this article can be found under https://doi.org/10.1002/smll.202002802.

DOI: 10.1002/smll.202002802

Particle
& Particle Systems Characterization
www.particle-journal.com

Controllable Synthesis of Upconversion Nanophosphors toward Scale-Up Productions

Yiran Jiao, Chen Ling, Jie-Xin Wang, Honeyfer Amanico, Joshua Saczek, Haoyu Wang, Sreepathy Sridhar, Ben Bin Xu, Steven Wang,* and Dan Wang**

Upconversion nanophosphors (UCNPs) are considered as an important synthesis arm within biomedical and energy sectors due to their unique optical characteristics, which can convert near-infrared light into higher energy emissions. However, key challenges, cost, compatibility of the materials, etc. have to be taken into serious consideration to transform this in-lab UCNPs technology into scale-up production for wider commercial needs. This review highlights the fundamental concepts of synthetic approaches for UCNPs and recaps recent advances in terms of large-scale production. A number of typical synthesis routes in both batch and continuous processes are reviewed, alongside their limitations and potential improvements when being considered for mass production. By discussing and exploiting the technical compacity for the potential synthetic trends, key challenges, and expectations of future synthesis methods for UCNPs are also outlined.

Y. Jiao, Prof. J.-X. Wang, Prof. D. Wang
State Key Laboratory of Organic Inorganic Composites
Beijing University of Chemical Technology
Beijing 100029, China
E-mail: wangdan@mail.buct.edu.cn

Y. Jiao, Prof. J.-X. Wang, Prof. D. Wang
Research Centre of the Ministry of Education for High Gravity Engineering and Technology
Beijing University of Chemical Technology
Beijing 100029, China

C. Ling, Dr. S. Wang
Department of Mechanical Engineering
City University of Hong Kong
Hong Kong 999077, China
E-mail: steven.wang@cityu.edu.hk

H. Amanico
Department of Chemical Engineering and Biotechnology
University of Cambridge
Cambridge CB2 3RA, UK

J. Saczek
School of Engineering
Newcastle University
Newcastle upon Tyne NE1 7RU, UK

Dr. H. Wang
Department of Chemical Engineering
Imperial College London
London SW7 2AZ, UK

S. Sridhar, Prof. B. B. Xu
Department of Mechanical and Construction Engineering
Faculty of Engineering and Environment
Northumbria University
Newcastle upon Tyne NE1 8ST, UK
E-mail: ben.xu@northumbria.ac.uk

The ORCID identification number(s) for the author(s) of this article can be found under https://doi.org/10.1002/ppsc.202000129.

DOI: 10.1002/ppsc.202000129

1. Introduction

Luminescence is a physical process to transform external stimuli into light emission, where these external stimuli can be light or other electromagnetic radiation. This phenomenon can be found in a variety of materials including organic dyes,[1] semiconductor quantum dots,[2] noble metal nanoclusters,[3] and lanthanide-doped phosphors.[4,5] In the last few years, the development of lanthanide-doped materials has attracted considerable interests due to their unique optical properties,[6] especially upconversion properties.[7]

The upconversion scheme, first proposed by Bloembergen[8] (1959) and demonstrated by Porter[9] (1961), represented an alternative to traditional Stokes photoluminescence, where it can convert near-infrared (NIR) light into ultraviolet (UV), visible, or NIR light,[10] enabling deeper penetration into biological tissues.[11] This feature together with its low toxicity, low auto-fluorescence, and high resistance to photobleaching[6,12–15] allows upconversion nanomaterials to be attractive carriers in downstream applications including in vitro and in vivo bioimaging,[16] drug delivery,[17] solar cells,[18] and photoreactions.[19]

Classical upconversion luminescence originates from upconversion nanoparticles (UCNPs), especially rare earth-doped UCNPs, which consists of a host matrix and dopant ions. A typical rare earth-doped UCNPs luminescent system is illustrated in **Figure 1**. Usually, dopant ions serve as luminescent activators and sensitizers.[20] By properly choosing the emission bands of doping ions, desired emission bands from UV to NIR can be achieved.[21,22] The host matrix could also act as a platform for upconversion emission[23] wherein the size, morphology, and phase of the host matrix can influence the performance of dopant ions and the corresponding upconversion luminescent intensity.[24,25] For example, it is found that in general when the $NaREF_4$ UCNPs size decreases, the emission intensity decreases as well. This is induced by the nonradiative relaxation of energy transfer and the quenching effect of surface ligands.[26]

Even though the relationship between optical performance and morphology of UCNPs have had been well understood,[23–26] relevant developments on commercializing such nanomaterials are hampered due to scaling-up production process, where bottlenecks normally exist in the reproducibility, repeatability as well as the yield from these methods. By recapping these reported synthesis methods, for example, thermal decomposition,[35–40] co-precipitation,[60–66] hydrothermal,[73–78] and ion exchange,[98–101]

Soft Matter

Accepted Manuscript

This article can be cited before page numbers have been issued, to do this please use: Z. Li, Y. Liu, M. Lei, A. Su, S. Sridhar, Y. Li, X. Liu, H. Lu, Y. Q. Fu and B. Xu, *Soft Matter*, 2020, DOI: 10.1039/C9SM02016K.

ROYAL SOCIETY OF CHEMISTRY

rsc.li/soft-matter-journal

View Article Online
DOI: 10.1039/C9SM02016K

ARTICLE

Stimuli-responsive gel impregnated surface with switchable lipophilic/oleophobic properties

Received 00th January 20xx,
Accepted 00th January 20xx

DOI: 10.1039/x0xx00000x

Zhenghong Li [a], Yingzhi Liu [a], Ming Lei [a], Ansu Sun [b], Sreepathy Sridhar [b], Yifan Li [b], Xuqing Liu [c], Haibao Lu *[a], Yong Qing Fu [b] and Ben Bin Xu *[b]

In this paper, we developed a novel morphing surface technique consisting of 3D printed miniature groove structure and injected stimuli-responsive hydrogel pattern, which is capable of switching between lipophilicity and oleophobicity under certain stimuli. Under swelling, the geometrical change of hydrogel will buckle the surface due to the structural confinement and create a continuous transition of surface topology. Thus, it will yield a change on surface wetting property from oleophilic to super-oleophobic with a contact angle of oil of 85° to 165°. We quantitatively investigate this structure-property relationship using finite element analysis and analytical modeling, and the simulation results and the modeling are in good agreement with the experimental ones. This morphing surface also holds its potentials to be developed into autonomous system for future sub-sea/off-shore engineering applications to separate oil and water.

1 Introduction

Developing novel and controllable wettability approaches using functional surfaces has attracted significant research interests, with underwater super-oleophobic surfaces being one of the hottest areas with promising applications in micro-fluidics, oil/water separation, marine antifouling coating, and self-cleaning technology.[1-7] For example, Jiang's group previously found an interesting phenomenon from fish, where its self-cleaning skin has a multi-length-scale hierarchical structure to enable an outstanding under water oleophobic property and on-demand surface wettability control, thus allowing fish to move freely in the oil-contaminated water.[8]

Aizenberg et.al developed a rough structure to lock the liquid to prepare a smooth liquid-infused porous surface (SLIPS), inspired by the structure of the pitcher plant.[9] This surface is good at reducing the viscous force of the liquid on the surface and can repel all liquids. Lu et al. prepared TiO_2 particles of two different sizes and ethanolic suspension with a certain proportion of fluorosilicone, using spray or dip coating methods to adhere them to the surface with double-sided tape. The surface was then immersed in hexadecane to obtain a tough, ultra-smooth and superhydrophobic material.[10] Rykaczewski et al. made micro-pattern arrays on silicon using the photolithography method, then the arrays were post-processed with octadecyltrichlorosilane hydrophobic layer, before infused the surface with ultra-light lubricating oil after adding perfluoro oil. This effectively prompts the droplet condensation of liquid with low surface tension.[11]

Bio-compatible and stimuli-responsive hydrogel materials can sense the environmental changes with adjustable responses controlled by their compositions and physical properties. Suo et al. demonstrated a hydrogel interferometer with adaptive colouration, providing a facilely tuneable way for broader functionalities.[12] Moreover, hydrogels are consisted of unique hydrophilic groups, whose internal three-dimensional (3D) crosslinked polymer network can absorb and retain large amounts of water molecules, which opens up opportunities for interface/surface structure designs to be applied in aqueous environment. For example, Liu's group used hydrogels to simulate fish scales' surfaces, which can be used in underwater super-oleophobic surface.[13,14] The conventional approach for oil/water separation is heavily relied on the hydrophilic nature of materials, *e.g.* using the hydrogel structures for oil/water separation.[15-17] However, the surfaces of such structures can be easily contaminated by oil residues, while the fabrication cost is normally high.

Recently, additive manufacturing, *e.g.* 3D printing, have re-invented the rapid prototyping technologies with a great efficiency.[18] Whilst there are great application potentials, some technical challenges remain, such as facilitation of complicated geometries and printing precisions. Currently, researchers have applied soft functional materials together with structural designs for enhanced actuating/sensing.[19,20] For example, Lewis et al fabricated strain sensors within highly conformal and extensible elastomeric matrices.[21] Kang et al printed integrated structures of a hydrogel and an elastomer in an arbitrary sequence, which enables new soft robotics concepts for medicine engineering.[22] Lei et al used 3D printing to achieve an auxetic metamaterial, which can continuously

[a] State Key Laboratory of Science and Technology on Advanced Composites in Special Environments, Harbin Institute of Technology, Harbin 150080, P.R. China.
[b] Smart Materials and Surfaces Laboratory, Faculty of Engineering and Environment, Northumbria University, Newcastle upon Tyne NE1 8ST, UK.
[c] School of Materials, University of Manchester, Oxford Road, Manchester, United Kingdom, M13 9PL.
† E-mail: luhb@hit.edu.cn and ben.xu@northumbria.ac.uk